Computational Color Science

To my parents, Giulio and Lucia, for showing a younger me the importance of studying.

And to Vicent Caselles, for proving this to me in a rigorous and mathematical way.

FOCUS SERIES

Series Editor Henri Maître

Computational Color Science

Variational Retinex-like Methods

Edoardo Provenzi

iSTE

WILEY

First published 2017 in Great Britain and the United States by ISTE Ltd and John Wiley & Sons, Inc.

ISTE Ltd
27-37 St George's Road
London SW19 4EU
UK

www.iste.co.uk

John Wiley & Sons, Inc.
111 River Street
Hoboken, NJ 07030
USA

www.wiley.com

Library of Congress Control Number: 2017931221

British Library Cataloguing-in-Publication Data
A CIP record for this book is available from the British Library
ISSN 2051-2481 (Print)
ISSN 2051-249X (Online)
ISBN 978-1-78630-159-8

Contents

Preface

Color Image Processing

Digital image processing has become one of the most important research fields in modern science. In fact, image processing algorithms are no longer confined to professional photographers or dedicated technicians (e.g. experts in medical imaging or in post-processing for fashion and cinema), but spread across the entire society thanks to the constantly increasing diffusion of portable digital devices, such as smartphones or tablets, with integrated cameras. Moreover, the complexity of mathematical techniques used nowadays in several image processing models is comparable to that of much more ancient scientific disciplines, e.g. theoretical physics.

Despite this, many image processing algorithms are still proposed for grayscale images and their extension to color images is not straightforward. Treating color information with the naive replication of well-established grayscale techniques on the three chromatic channels may not be feasible due to intrinsic mathematical problems or the possible introduction of artifacts and/or color shifts.

A dramatic example is given by histogram equalization, which will be introduced in Chapter 4. While this technique can be regularized and smoothed to considerably improve the contrast and detail visibility of a grayscale image, it may totally disrupt the chromatic content when directly replicated on the three color channels. In the literature, we can find multiple proposals to avoid, or at least limit, this problem. A common strategy consists of encoding the image information in a color space where achromatic and chromatic channels are separated, e.g. HVS, CIELab, L$\alpha\beta$ and so on, and only performing transformation on the luminance (achromatic) channel, while operating minor corrections on the chromatic content. Another proposal, which will be presented throughout this book, consists of devising transformations inspired by the human visual system (HVS) and applying them to the three color channels independently. The precursor of this kind of model is the famous Retinex model of Land and McCann [LAN 71], which will be described in detail in Chapter 3, along with its many interpretations.

In the subsequent chapters, it will be shown how a whole class of Retinex-based models inspired by the properties of the HVS can be embedded in a rigorous variational framework. The variational interpretation allows us to understand the behavior of these models with respect to important image features such as contrast and dispersion of tonal intensities. Moreover, we can mathematically compare different Retinex-based algorithms and clearly understand their similarities and differences, which is very difficult to do without relying on their variational formulation.

Due to the importance of human visual properties in the analysis of the color correction models presented in this book, a brief summary of the basic features of the HVS is presented in the first chapter.

Edoardo PROVENZI
February 2017

1

Rudiments of Human Visual System (HVS) Features

In this chapter, the basic facts about the processing of a visual signal by the retina and brain will be recalled. The purpose of this chapter is not only to provide an exhaustive treatise about the Human Visual System (HVS), but also to introduce some important concepts and formulae that will have a fundamental role in the development of the models described in Chapter 5. For complete details on these topics, see, for example, [FAI 05].

1.1. The retina

In Figure 1.1, a human eye and the cross-section of a retina are represented.

Several layers of neural cells constitute the retina, beginning with around 130 million photoreceptors (rods and cones) and ending with about 1 million ganglion cells. The specific processing that occurs in each type of cell is complex and not yet completely understood.

What we know for certain is that retinal cells may respond nonlinearly to stimuli and are connected via links called *synapses*, which are able to perform basic mathematical operations such as addition, subtraction, multiplication, division, amplification and gain control. Considered as a whole, these operations result in a clever and sophisticated modification of the visual input.

Among all retinal cells, the most important for our purposes are the photoreceptors (rods and cones), to which the next section is devoted.

Computational Color Science: Variational Retinex-like Methods, First Edition. Edoardo Provenzi.

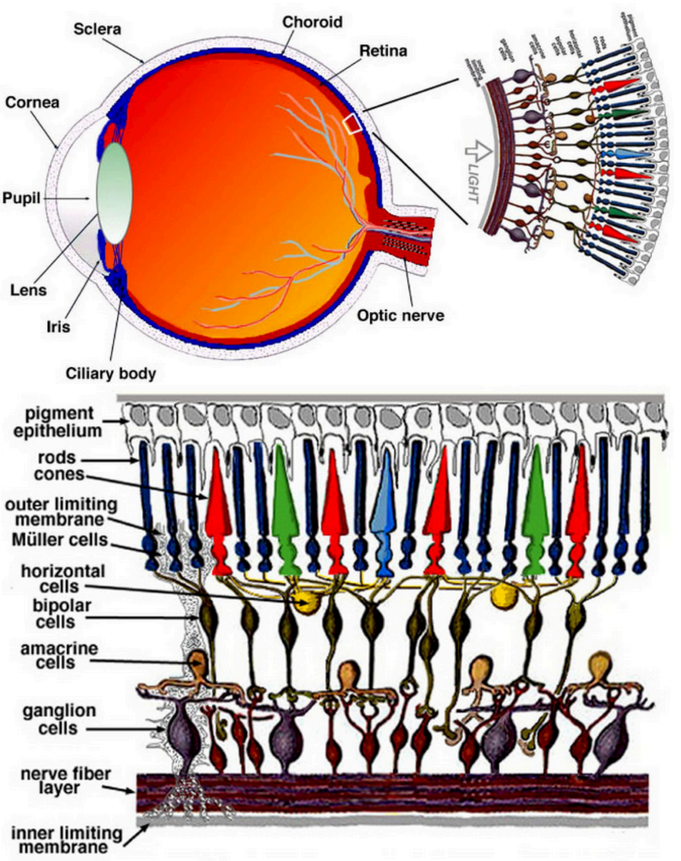

Figure 1.1. *Top: a human eye. Bottom: the cross-section of a human retina. Courtesy of [KOL 95]. For a color version of the figure, see www.iste.co.uk/provenzi/color.zip*

1.1.1. *Photoreceptors: rods and cones*

Rods and cones are labelled in this way because of their shape. Rods work in the so-called *scotopic region*, below 10^{-3} cd/m^2, while cones respond to luminance levels higher than 10 cd/m^2, a range called the *photopic region*. In the intermediate range, called the *mesopic region*, both rods and cones are activated, but their response is less efficient than when they work in isolation from each other. Henceforward, we will only consider photopic conditions and thus the properties of cones.

Color vision in the photopic region is possible, thanks to the existence of three types of cone receptors with peak spectral sensibilities distributed along the visual spectrum (see Figure 1.2). This is due to the existence of three slightly different molecular structures in each cone type, which are referred to as L, M and S cones. They refer to the *long*, *middle* and *short* wavelengths where cones have their maximal sensitivity at 560 nm, 530 nm and 420 nm, respectively.

The LMS cones can also be referred to as the RGB cones. Of course, RGB is the notation for monochromatic *red*, *green* and *blue*, but, as shown in Figure 1.2, this is an abuse of language, in particular because the L cones are gathered in the region of monochromatic green-yellow, not red.

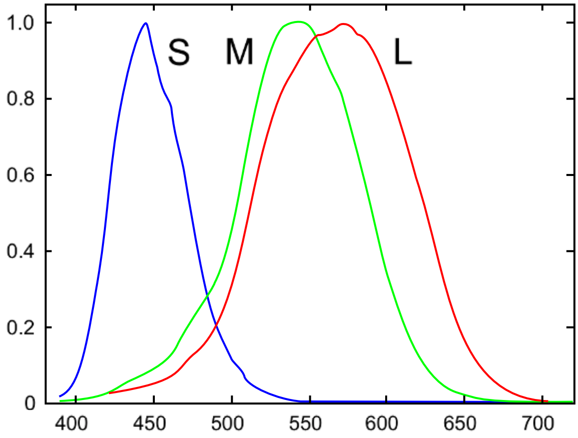

Figure 1.2. *The normalized spectral sensitivity functions of the LMS cones. Courtesy of [KOL 95]. For a color version of the figure, see www.iste.co.uk/provenzi/color.zip*

Note that the spectral sensibilities of the three cone types are broadly overlapping, in particular those of the L and M cones. This constitutes a substantial difference with respect to most physical imaging systems, in particular digital cameras (see, e.g., [JIA 13]), where sensor responses are only slightly overlapping.

Finally, it must be noted that the distribution of cones in the retina is not uniform: S cones are relatively sparse and completely absent in the *fovea*, the central part of the retina with the highest density of L and M cones.

1.2. Adaptation and photo-electrical response of receptors

Light adaptation is the name used to describe the fact that the HVS is able to adapt to different light intensities in order to enable detail perception over a range of 10 orders of magnitude.

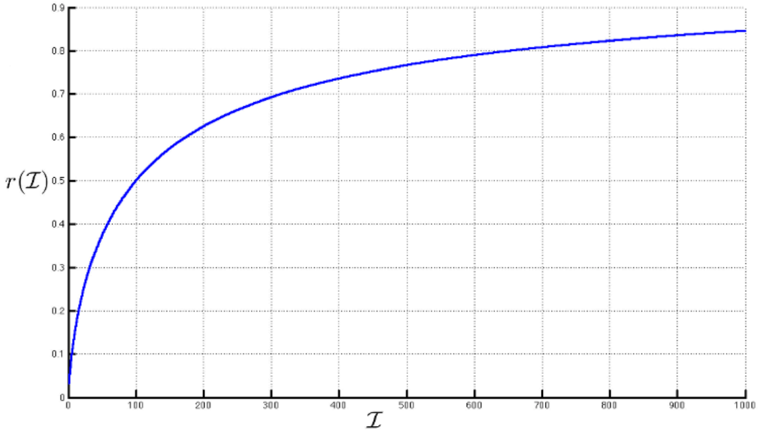

Figure 1.3. *Compressive effect of Michaelis-Menten's response in arbitrary units between 1 and 1000 and with* $\gamma = 0.74$*. The semi-saturation constant* $\mathcal{I}_S$ *has been arbitrarily set to 100 and* $r(\mathcal{I}_S) = 1/2$

Before reaching a photoreceptor, rod or cone, light intensity is reduced by the cornea, crystalline lens, the humors and the macula. Moreover, when a light photon is absorbed by a photoreceptor, a transduction occurs: the electromagnetic energy carried by the photon is passed to the photoreceptor, which changes the electric potential of its membrane. The empirical law that describes the photoreceptor transduction is known as *Michaelis-Menten's equation* [SHA 84] (or *Naka-Rushton's equation* when $\gamma = 1$):

$$r(I) = \frac{\Delta V}{\Delta V_{\max}} = \frac{\mathcal{I}^{\gamma}}{\mathcal{I}^{\gamma} + \mathcal{I}_S^{\gamma}}, \tag*{[1.1]}$$

where $\Delta V_{\max}$ is the highest difference of potential that the membrane can handle, γ is a constant (measured as 0.74 for the rhesus monkey), $\mathcal{I}$ is light intensity and $\mathcal{I}_S$ is the value at which the photoreceptor response is half maximal, called the *semi-saturation level*. Note that, as previously mentioned, each type of cone is most sensitive over a particular waveband, thus the value of the semi-saturation constant $\mathcal{I}_S$ can change for the three types of cones.

The photo-electrical response of photoreceptors, along with other phenomena occurring mainly in the retina, is considered one of the main explanations for the property of *adaptation to the average luminance level* of the HVS. In fact, after the photoreceptors transduction, the dynamic range is centered in $r(\mathcal{I}_S) = 1/2$, as can be seen in Figure 1.3, which shows the nonlinear compressive behavior of Michaelis-Menten's response. The adaptation property of the HVS is crucial: without it, the operational range of our vision would be much narrower and sight as we know it would be impossible.

1.3. Spatial locality of vision

Transduction curves shown in Figure 1.3 represent the very first stage of visual processing. The electrical signals generated by the photoreceptors are processed by the retinal neurons, synapses and ganglion cells, until they are then finally transmitted to the brain via the optic nerve. In the brain, the visual signal is processed in several zones, each of which is devoted to processing different characteristics, e.g. shape, orientation, spatial frequency, size, color, motion [ZEK 93].

Our present understanding of post-photoreceptors physiological operating principles is far from being precise: not only the brain, but also retinal functions still present some unknown features. Without entering the very complicated analysis of post-photoreceptor physiology, what is important to underline here is that the signals transmitted from the photoreceptors to higher levels of the visual path are not simple point-wise representations, but they consist of sophisticated combinations of receptors responses to photons coming from different parts of the visual scene. In fact, even when we fix a single point, our eyes are constantly moving and capturing light information from all over the visual scene. These movements are called *saccadics*, and they are the fastest of our body.

A conventional nomenclature has been introduced to rigorously define the local neighborhood of a point in a visual field (see, e.g., [HUN 14] and [FAI 05]):

– Stimulus: the visual element corresponding to foveal vision, about 2° of angular extension;

– Proximal field: the closest environment of the stimulus, it extends isotropically for about 2° from its edge;

– Background: extends isotropically for about 10° from the edge of the proximal field;

– Surround: a field that lies outside the background;

– Adapting field: the total environment of the stimulus considered the proximal field, the background and the surround, until the limit of vision in all directions.

The components of the adaptive field are shown in Figure 1.4.

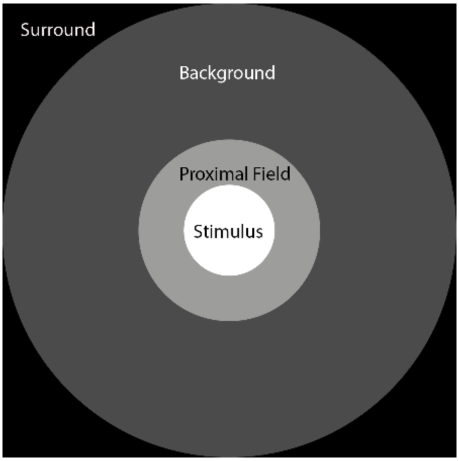

Figure 1.4. *Components of the adaptive field*

1.4. Local contrast enhancement

The eye's optical system and the response of photoreceptors strongly reduce the range of light intensity that can be processed. To *compensate* this reduction, the HVS has developed a system to enhance contrast perception already in the retina, in particular with the typical lateral inhibition phenomenon exhibited by ganglion cells [CRE 87, CRE 90, HUR 90, ZAI 99, MCC 11].

Studies about ganglion cells revealed that the electric potential of their membrane spontaneously oscillates at a base rate while at rest, an event called *firing of action potential*. *Excitation* of retinal ganglion cells results in an increased firing rate while *inhibition* corresponds to a depressed rate of firing. For this reason, the magnitude of the signal is represented in terms of the number of spikes of voltage per second fired by the cell rather than by the difference of voltage across the cell membrane.

To represent the physiological properties of ganglion cells, it is useful to consider the concept of *receptive field*, which is a *graphical representation of the area in the visual field to which a given cell responds*. The positive or negative response is indicated in the receptive field, as shown in Figure 1.5, which represents a prototypical receptive field for ganglion cells.

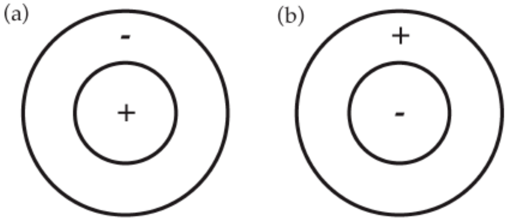

Figure 1.5. *Center-surround receptive fields: (a) on-center; (b) off-center*

Receptive fields illustrate *center-surround antagonism*: the receptive field in Figure 1.5 (a), called *on-center*, describes a positive central response, surrounded by a negative surround response, while Figure 1.5 (b), called *off-center*, shows a ganglion cell response of opposite polarity.

The excitation-inhibition processing can explain some *local contrast enhancement* effects as Mach bands, see Figure 1.6: If we focus on the vertical band on the right the adjacent gray level appears lighter, if we focus on the vertical band on the left the adjacent gray level appears darker, in spite of the fact that the luminance value in each vertical gray band is constant.

Consider Figure 1.7: in situation 1, excitation and inhibition fire signals equally, so a uniform patch is perceived; in situation 2, part of the inhibition component of the receptive field is activated by a region of highest luminance and so it prevails, generating a sensation of darker gray; on the contrary, in situation 3, part of the inhibition component of the receptive field is activated by a region of lowest luminance and so it is dominated by the excitation component, which produces a sensation of lighter gray.

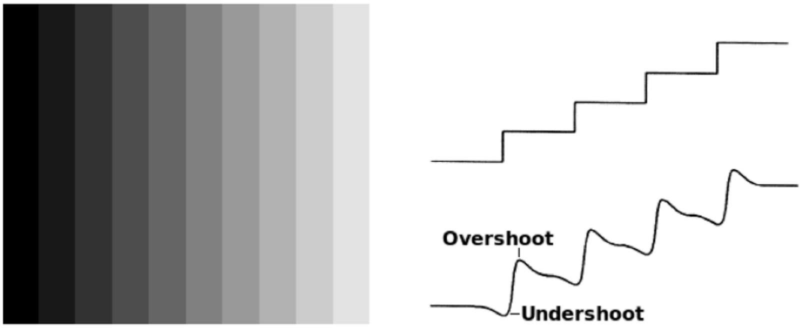

Figure 1.6. Left*: Mach bands effect.* Right*: real (above) and apparent (below) luminance pattern*

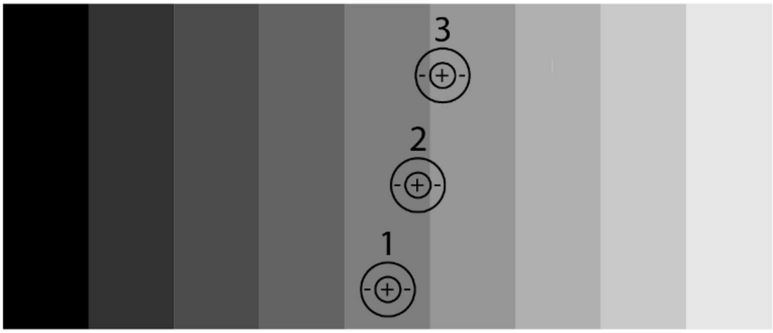

Figure 1.7. *Excitation-inhibition explanation of the Mach band effect*

Another well-known local contrast enhancement effect is simultaneous contrast, first discussed by Chevreul in 1839 in his essay "*La loi du contraste simultané des couleurs*", as shown in Figure 1.8.

Figure 1.8. *Simultaneous contrast: even though the two inner squares have the same luminosity, our perception is different, due to the difference in the left and right background*

The influence of context on the perception of a point decreases with distance, as discussed, for example, in [WAL 48, RUD 04], where the authors developed a clever psychophysical experiment to measure induction of achromatic stimuli. We will discuss this method in Chapter 3.

1.5. Physical vs. perceived light intensity contrast: Weber-Fechner's law

In the previous section, we have seen that the HVS rearranges spatial information in order to amplify the response to edges present in a visual scene. This phenomenon concerns *spatial contrast*. In this section, we recall the HVS response to *light intensity contrast*, without considering the spatial distribution across the scene.

Psychophysics is the science that aims to model the magnitude of human perception in response to external stimuli in a mathematically rigorous way. The German physicist E. Weber, with results obtained in the second half of the 19th Century, was one of the first scientists in history to develop psychophysical experiments to test perception of light intensity contrast.

To avoid unwanted biases, Weber worked in a very constrained setting: a dark-adapted human observer was put in a dim room in front of a white screen on which a narrow beam of light was shone in the center of the visual field. The light intensity $\mathcal{I}$ of the beam was increased very slowly and the observer was asked to tell whether he/she could perceive an intensity change. The least perceptible intensity change $\Delta\mathcal{I}$ is called JND for *Just Noticeable Difference*.

Weber found out that the JND increased proportionally with the light intensity[1], i.e. $\Delta\mathcal{I}/\mathcal{I} = K$ or $\Delta\mathcal{I} = K\mathcal{I}$. K is called *Weber's constant* and the relationship between $\Delta\mathcal{I}$ and $\mathcal{I}$ is called Weber's law.

Weber's law says that, as we increase the background light $\mathcal{I}$, the difference $\Delta\mathcal{I}$ must increase proportionally in order to be able to appreciate $\mathcal{I} + \Delta\mathcal{I}$ as being different from $\mathcal{I}$. This partially explains why dark areas of a visual scene are more sensitive to noise, and thus why it is more important to perform denoising in dark areas of digital images rather than in bright ones. This last consideration is a practical application of a psychophysical phenomenon.

The founder of psychophysics, the German experimental psychologist G. Fechner, gave the following interpretation of Weber's law: he introduced the adimensional quantity $s(I)$ called light *sensation* and stated that the difference of sensation $\Delta s(I)$ is proportional to a slightly modified Weber's ratio, i.e.

$$\Delta s(\mathcal{I}) = k\frac{\Delta\mathcal{I}}{n+\mathcal{I}}, \qquad [1.2]$$

where $k > 0$ is a constant and $n > 0$ is a quantity, often interpreted as *internal noise* in the visual mechanism. Fechner assumed that this finite difference equation could be valid for arbitrarily small differences, which of course is not possible because of the very definition of JND. However, following Fechner's hypothesis, the finite-difference equation [1.2] becomes a differential equation [WYS 82]:

$$ds(\mathcal{I}) = k\frac{d\mathcal{I}}{n+\mathcal{I}}. \qquad [1.3]$$

By integrating both sides from $\mathcal{I}_0$, the lowest threshold of perceivable light intensity, defined by $s(\mathcal{I}_0) = 0$ and $s(\mathcal{I}_0 + \varepsilon) > 0$ for all $\varepsilon > 0$, to a generic value of $\mathcal{I}$, we obtain

$$\int_{\mathcal{I}_0}^{\mathcal{I}} ds(\mathcal{I}) = k\int_{\mathcal{I}_0}^{\mathcal{I}} \frac{d\mathcal{I}}{n+\mathcal{I}} \iff s(\mathcal{I}) - s(\mathcal{I}_0)$$
$$= k[\log(n+\mathcal{I}) - \log(n+\mathcal{I}_0)], \qquad [1.4]$$

---

[1] Weber's law is approximately valid not only for the visual sense, but also for all the other senses, with different values of Weber's constant.

which can be rewritten as follows:

$$s(\mathcal{I}) = k\log\left(\frac{n+\mathcal{I}}{n+\mathcal{I}_0}\right) = s_0 + k\log(n+\mathcal{I}), \qquad [1.5]$$

where $s_0 = -k\log(n+\mathcal{I}_0)$. This last formula is called *Weber-Fechner's law* and it states that *the sensation of light differences*, in the very constrained context of Weber's experiment, *grows as the logarithm of the light intensity*.

We must stress the *limitations of Weber-Fechner's law*:

1) First, it is only valid for very simple visual scenes, such as those considered by Weber in his experiments. As discussed in the previous section, the presence of a non-trivial spatial context introduces significant modifications in visual perception;

2) Second, even for very simple visual scenes, Fechner's assumption about the possibility to maintain the validity of Weber's law passing from finite to infinitesimal light intensity differences is correct only for a limited range of light intensity between the minimum and the maximum perceivable light. As we approach these extreme situations, this assumption fails dramatically due to strong nonlinearities in the visual mechanism and Weber-Fechner's law does not hold anymore.

The last phenomenological feature of human vision that is worth recalling is color constancy; however, its role in image processing is so important that it will be separately discussed in the following chapter.

2

Computational Color Constancy Algorithms

Color constancy is the ability of human vision to perceive colors very robustly with respect to changes in illumination. The precise reasons behind color constancy are not yet known. Phenomenologically speaking, it is known that both cognitive and physiological effects of color memory and chromatic adaptation, respectively, play a major role in color constancy. For more information about this topic, see, for example, [EBN 07] and [FAI 05].

Instead of investigating the causes of human color constancy, in this chapter, we will review the computational models of image processing that try to digitally reproduce color constancy. This discussion will also be important for the development of perceptually variational models of color enhancement in Chapter 5. Before providing the details about the variety of computational color constancy models proposed in the literature, it is worthwhile answering a common question about models of this kind, namely “why do we need a color constancy algorithm when our visual system already does that job?”. The answer is that *humans possess the color constancy ability when they are embedded in a visual scene and adapted to its illuminant conditions*. Thus, we cannot automatically remove the chromatic layer superimposed on a digital image by a non-neutral illuminant simply by looking at it on a digital screen. This is the reason why computational color constancy algorithms are studied in image processing.

Computational Color Science: Variational Retinex-like Methods, First Edition. Edoardo Provenzi.

2.1. The dichromatic and Lambertian image formation models

In order to understand the details of computational color constancy models, it is necessary to start by describing the dichromatic and Lambertian models of image formation [GEV 12]. Suppose that we have a visual scene illuminated by *only one spatially homogeneous light source* with spectral power distribution $E : \Lambda \to [0, +\infty)$, with Λ being the set of visible wavelengths λ of the electromagnetic spectrum. Let us also suppose that we have an RGB camera with spectral sensitivity functions in the low, medium and high visible wavelengths, denoted by R, G and B, respectively.

We denote the spectral sensitivity functions as $R_c : \Lambda \to [0, +\infty)$, $c \in \{R, G, B\}$. To avoid a cumbersome notation, each time the chromatic index c appears, it is implicitly supposed to vary in the set $\{R, G, B\}$. The analysis performed in [JIA 13], p. 4322, showed that $\mathrm{supp}(R_c)$, the supports of the functions R_c, are very similar for practically all commercial cameras and do not overlap as much as those of spectral sensitivity functions of retinal cones.

If we point the camera towards the light source, we obtain the light vector $\vec{L} = (L_R, L_G, L_B) \in (0, +\infty)^3$, with

$$L_c = \int_\Lambda E(\lambda) R_c(\lambda)\, d\lambda. \qquad [2.1]$$

Following [GIJ 11], we say that $\vec{L}$ is *neutral*, or *white*, if there exists a real positive constant K, such that $\vec{L} = K(\frac{1}{\sqrt{3}}, \frac{1}{\sqrt{3}}, \frac{1}{\sqrt{3}})$, i.e. if it is proportional to a unit vector whose color channels are balanced and none of them prevail over the others.

Let us now turn our camera from the illuminant to the objects of the visual scene and denote by $S(\xi, \lambda) \in [0, 1]$ the surface reflectance of the scene objects in the spatial position $\xi = (\xi_1, \xi_2, \xi_3) \in \mathbb{R}^3$ and at the wavelength $\lambda \in \Lambda$. If $S(\xi, \lambda) = 1$, the point ξ is said to be *perfectly reflective* at the wavelength λ.

In the dichromatic reflection model [SHA 85], the scene elements are supposed to have both a *specular* and a *diffused reflectance*. A specular reflection is only visible if the normal vector of a shiny object is oriented precisely halfway between the direction of incoming light and the direction of the camera sensor. The diffused reflectance is due to the scattering between the light and the surface particles of an object, which produces an isotropic reflection of light. We denote by $m_s(\xi)$ and $m_d(\xi)$ the scale factors that weight the relative amount of specular and diffused reflectance, respectively, contributing to the overall light reflected at the location ξ.

Suppose now that we take a picture of the scene (and not of the illuminant) with the same RGB camera. The rays of light emitted or reflected by scene objects project univocally[1] to the pixels of the image formed by the camera. Using this one-to-one correspondence, we can identify the portion of the visual scene represented by the camera with the two-dimensional support Ω of the image, a particular point ξ of an object with the corresponding pixel $x = (x_1, x_2) \in \Omega$ and denote, without ambiguity, the reflectance $S(\xi, \lambda)$ as $S(x, \lambda)$.

With this notation in mind, we can write the intensity of any pixel $x \in \Omega$ of the digital image as

$$I_c^{\text{Dichromatic}}(x) = m_d(x) \int_\Lambda S(x, \lambda) E(\lambda) R_c(\lambda)\, d\lambda + m_s(x) L_c, \qquad [2.2]$$

note that in the specular term, the reflectance is assumed to be 1. The intensity values $I_c(x)$ will always be considered normalized in the unit interval $[0, 1]$.

In the *Lambertian reflection models*, the specular reflection term is ignored, so that $m_d(x) \equiv 1$ and $m_s(x) \equiv 0$, and the resulting image formation model reduces to

$$I_c^{\text{Lambert}}(x) = \int_\Lambda S(x, \lambda) E(\lambda) R_c(\lambda)\, d\lambda. \qquad [2.3]$$

In the literature, we often find equation [2.3] simplified as follows:

$$I_c(x) = S_c(x) L_c. \qquad [2.4]$$

There are two possible ways to pass from equation [2.3] to the separable form [2.4]. The first possibility is to suppose that the camera spectral

---

[1] Here we assume that the resolution of the picture is high enough to consider negligible the averaging of light information performed in the pixel area.

sensitivity functions are Dirac deltas with spikes in R, G, B; this hypothesis is not plausible in conventional digital photography [JIA 13].

The second possibility consists of supposing that *the supports* $\mathrm{supp}(R_c)$ of the camera sensitivity functions R_c form a *mutually disjoint partition of* Λ, i.e.

$$\Lambda = \bigcup_{c\in\{R,G,B\}} \mathrm{supp}(R_c), \quad \mathrm{supp}(S_c) \cap \mathrm{supp}(S_{c'}) = \emptyset, \text{ if } c \neq c', \qquad [2.5]$$

and that *the reflectance functions* $S(x, \lambda)$ *are constant with respect to* λ *in each subset* $\mathrm{supp}(R_c)$ *of* Λ, i.e.

$$S(x, \lambda) = S_c(x) \qquad \forall \lambda \in \mathrm{supp}(R_c). \qquad [2.6]$$

In fact, in that case, equation [2.3] can be rewritten as $I_c(x) = S_c(x) \int_\Lambda E(\lambda)R_c(\lambda)\, d\lambda$, i.e. $I_c(x) = S_c(x)L_c$, thanks to [2.1].

This hypothesis is much more realistic: in fact, even if the sensitivity functions of digital cameras overlap, they all have a wide area in which they can be considered as disjoint (see, e.g., Figure 1 in [JIA 13]). However, it must be kept in mind that [2.4] is an approximation.

We also note that this hypothesis does not make sense for a vision model because the L and M retinal cone sensitivity functions are highly overlapping. Therefore, if we used the hypothesis of constant reflectance in support of the spectral sensitivities of cones, then $S_L(x)$ would always be equal to $S_M(x)$.

Reflectance and illuminants play two very different roles in image formation. To understand this, let us consider Figure 2.1. If the blue color exhibited by the tissue depicted in the picture is given by the relative difference between the reflectance values $S_R(x), S_G(x), S_B(x)$ of the tissue, then we say that the *dominant color* of the image is blue. However, the picture could represent a white tissue and the blue color could be generated by the relative difference between the illuminant values (L_R, L_G, L_B); in this case, we say that the image has a blue *color cast*.

Let us note that, for both equations [2.3] and [2.4], the problem of estimating the illuminant or the reflectance from the single image information provided by $I_c(x)$ is *under-constrained*, because we only have one piece of information, $I_c(x)$, for two unknowns: reflectance and illuminant value. There exist several approaches to break this ambiguity; a detailed summary is provided in [GIJ 11]. In the following section, we will analyze the so-called white-patch, gray-world and gray-edge methods in detail to estimate illuminant value and reflectance. This information will be important for the discussion of the color correction models presented in Chapter 3.

Figure 2.1. *A typical example of ambiguity in the interpretation of the color exhibited by a picture: is it the image of a blue tissue taken under a neutral illuminant, or is it, for example, the picture of a white tissue taken under a blue illuminant? For a color version of the figure, see www.iste.co.uk/provenzi/color.zip*

2.2. Classical hypotheses for illuminant and reflectance estimation

If we consider the Lambertian image formation model and its simplified version, equations [2.3] and [2.4] respectively, we infer that color changes in pictures of a *fixed* visual scene taken with a *fixed* setting of an RGB camera can only be produced by a change in illumination. Thus, if it were possible to estimate the illumination, we could filter it out and retain just the intrinsic object reflectance. In particular, if the hypotheses underlying the simplified Lambertian image formation model described by equation [2.4] are satisfied, then the estimated reflectance can be obtained by dividing the image values $I_c(x)$ by the estimated illuminant L_c:

$$S_c(x) = \frac{I_c(x)}{L_c}. \qquad [2.7]$$

Before describing the white-patch, gray-world and gray-edge methods to estimate the illuminant and reflectance, it is worthwhile underlying their positive and negative sides. The major advantage of these methods is that they have fast performance, are easy to program and, at least for the pure white-patch and gray-world assumptions, do not require a training procedure. Their main disadvantages are the fact that they only make physical sense when the scene is illuminated by a single spatially homogeneous light source E and that they rely on the validity of an assumption on reflectance distribution that is frequently violated in real-world scenes. This is the reason why these algorithms often need an ad-hoc pre-processing step.

Finally, it is important to stress that intrinsic object reflectance cannot be associated with color: while reflectance is a physical quantity, it's the interaction between the reflectance of objects that creates color sensation, not the interaction between illumination and reflectance. In fact illumination is discounted thanks to the color constancy property of human vision.

2.2.1. *White-patch assumption and related models*

The white-patch (WP) assumption [LAN 71, LAN 77] states that *there exists at least one patch of an object in the physical scene with perfect reflectance (for all wavelengths)*. This means that if the scene is illuminated by the neutral light defined in section 2.1, then the perfectly reflective patch will be measured as having the same intensity in each chromatic channel. It follows that any deviation from this situation will be caused by a certain color temperature of the illuminant being different from that of white light [WYS 82].

The white-patch assumption stated above is often violated in natural scenes. For this reason, a *relaxed* version can be formulated which requires the existence of at least a patch with perfect reflectance in each separated chromatic channel. The relaxation lies in the fact that now the perfect reflective patch may differ in every chromatic channel, which is a far more common situation in practice.

Let us see how we can use the white-patch assumption to estimate L_c. Remember that $S(x, \lambda) \in [0, 1]$ for all $x \in \Omega$ and all $\lambda \in \Lambda$, so the white-patch assumption implies that there exists a pixel $\bar{x} \in \Omega$, such that $S(\bar{x}, \lambda) = 1$ for all $\lambda \in \Lambda$. It follows that:

$$\begin{aligned} I_c(\bar{x}) &= \int_\Lambda S(\bar{x}, \lambda) E(\lambda) R_c(\lambda)\, d\lambda \\ &= \int_\Lambda E(\lambda) R_c(\lambda)\, d\lambda = L_c, \quad \forall c \in \{R, G, B\}. \end{aligned} \tag{2.8}$$

Since L_c is supposed to be uniform across the image, and since 1 is the highest reflectance value, it follows that $I_c(\bar{x}) = \max\limits_{x\in\Omega}\{I_c(x)\}$. So, if the white-patch assumption is satisfied, the illuminant can be estimated as follows:

$$L_c^{\mathrm{WP}} = \max_{x\in\Omega}\{I_c(x)\}, \qquad [2.9]$$

this explains why this method of illuminant estimation is often, and more properly, called "max-RGB".

As a result, if the WP assumption is satisfied, then there exists a unique $\bar{x} \in \Omega$, such that $M_c = I_c(\bar{x}) = \max\limits_{x\in\Omega}\{I_c(x)\}$ for all $c \in \{R, G, B\}$, so if M_c is the same for all $c \in \{R, G, B\}$, then the illuminant is neutral, otherwise the scene is illuminated by a non-neutral light.

If the relaxed WP assumption is verified, then we can only guarantee the existence of three (possibly different) pixels, $\bar{x}_R$, $\bar{x}_G$, $\bar{x}_B$, such that

$$M_c = \max_{x\in\Omega}\{I_c(x)\} = I_c(\bar{x}_c), \qquad [2.10]$$

but the conclusion is the same as mentioned above, i.e. if M_c is different as c varies in $\{R, G, B\}$, then the illuminant is non-neutral and *vice versa*.

If the WP assumption or its relaxed version is verified, then the estimated reflectance is

$$S_c^{WP}(x) = \frac{I_c(x)}{\max_{x\in\Omega}\{I_c(x)\}}. \qquad [2.11]$$

The easiest computational model that used this strategy to enhance images is the so-called von Kries algorithm [VON 02], which consists of the following diagonal transformation:

$$\begin{pmatrix} \tilde{I}_R(x) \\ \tilde{I}_G(x) \\ \tilde{I}_B(x) \end{pmatrix} = \begin{pmatrix} \frac{1}{\max_{x\in\Omega}\{I_R(x)\}} & 0 & 0 \\ 0 & \frac{1}{\max_{x\in\Omega}\{I_G(x)\}} & 0 \\ 0 & 0 & \frac{1}{\max_{x\in\Omega}\{I_B(x)\}} \end{pmatrix} \begin{pmatrix} I_R(x) \\ I_G(x) \\ I_B(x) \end{pmatrix}, \qquad [2.12]$$

where $\tilde{I}_c$ is the c-th component of the enhanced output image.

To physically test the validity of the WP hypothesis (respectively, its relaxed version), we must illuminate a scene with a uniform light of known spectral composition and then verify whether the brightest pixel in the whole image (respectively, in each separated chromatic channel) has the same values as the illuminant or at least very similar ones. Without knowing the reflectance of the materials in the scene or the spectral distribution and geometry of illumination, the only way to determine whether or not a visual scene fulfills the WP assumption or its relaxed version is to estimate the illumination components (L_R, L_G, L_B) with techniques that do not rely on physically based hypotheses about the scene displayed in the picture (for an overview of such techniques, see, e.g., [GIJ 11]).

Max-RGB algorithms are very sensitive to noise and outliers, which can alter the whole computation. To overcome this problem, the image is often preprocessed. For instance, in [BAR 02, FUN 10], the authors showed that smoothing the image much improves the performances by limiting the effect of outliers.

2.2.2. *Gray-world assumption and related models*

The gray-world assumption [BUC 80] states that "*the (spatial) average reflectance in a visual scene is achromatic (gray)*". As noted for the white-patch assumption, if the gray-world assumption holds true and the measured average intensity is not achromatic, then the illuminant has a non-neutral color.

The mathematical translation of the gray-world assumption is as follows:

$$\frac{1}{|\Omega|}\int_{\Omega} S(x,\lambda)\,dx = k, \qquad \forall\lambda \in \Lambda, \tag{2.13}$$

where $|\Omega|$ is the area of Ω (or the number of pixels of the image support in the discrete framework). The formula presented above indicates that if the gray-world hypothesis is true, when we compute the spatial average of the reflectance, the dependence on λ decreases and there remains a constant k (typically close to 1/2).

This does not mean that S is independent of λ; in fact, $S(x,\lambda)$ is allowed to vary with λ. Rather, it means that for every fixed $\lambda \in \Lambda$, the values of $S(x,\lambda)$

are evenly distributed across the scene around a middle value k, so that the deviations from k cancel out with the spatial integration.

Let us see how we can estimate the illumination components L_c with the gray-world assumption. If we compute the *average image intensity*, we then have:

$$\begin{aligned}\overline{I_c} &\equiv \frac{1}{|\Omega|}\int_\Omega I_c(x)\,dx = \frac{1}{|\Omega|}\int_\Omega\left(\int_\Lambda S(x,\lambda)E(\lambda)R_c(\lambda)\,d\lambda\right)dx\\ &= \int_\Lambda\left(\frac{1}{|\Omega|}\int_\Omega S(x,\lambda)\,dx\right)E(\lambda)R_c(\lambda)\,d\lambda = kL_c, \end{aligned}\qquad [2.14]$$

where we have used the definition of L_c and the gray-world hypothesis in the last step of the computation.

Consequently, the gray-world (GW) illuminant and reflectance estimations are:

$$L_c^{\mathrm{GW}} = \frac{\overline{I_c}}{k},\quad S_c^{GW}(x) = k\frac{I_c(x)}{\overline{I_c}}.\qquad [2.15]$$

Since $k = \overline{I_c}/L_c$, without knowing the spectral composition of the illuminant, we cannot assure that k remains constant in the three chromatic channels because of the symmetrical distribution of the reflectance values around k, or because of L_c. So, to physically test the GW assumption, we have to illuminate the scene with a uniform neutral light and calculate the average image intensity in the three chromatic channels: if this remains constant, then the GW hypothesis holds true. As a result, if a scene complies with the GW assumption and $\overline{I_c}$ varies with c, then the scene in the picture is taken under a non-neutral illuminant.

Also in this case, as in the WP scenario, without knowing the spectral distribution and geometry of illumination, the only way to determine whether a visual scene fulfills the GW assumption or not is to estimate the illumination components (L_R, L_G, L_B) with techniques that do not rely on hypotheses about the physical nature of the scene displayed in the picture.

If the condition [2.6] holds, then we can consider the simplified Lambert image formation model $I_c(x) = S_c(x)L_c$. So, the relaxed GW assumption

$$\frac{1}{|\Omega|}\int_{\Omega} S_c(x)\,dx = k \qquad [2.16]$$

implies again the equation $\bar{I}_c = kL_c$. Thus, the GW assumption and its relaxation lead to the same illuminant estimation equation.

We observe that this method is not as sensitive to noise as the max-RGB because it involves an average operation, in which the effect of outliers is automatically smoothed. However, gray-world methods are sensitive to the presence of large areas with a uniform color different from gray; in fact, for these kinds of scenes, the gray-world assumption is evidently violated and the illuminant estimation that they provide can be far from correct.

Also in this case, we can pre-process the image to partially overcome the violation of the gray-world assumption; a typical strategy is to segment the image, compute the average color of all segments and then suitably combine this information to compute the global average color as proposed by [BAR 02].

2.2.3. *Shades of gray and multi-scale max-RGB assumptions to mix white-patch and gray-world hypotheses*

The considerations of the previous two sections imply that the white-patch and gray-world methods have a higher probability to work properly if the picture has a high contrast. In fact, in this case, we maximize the probability of having bright objects in the scene (thus approaching the white-patch assumption) and minimize the probability of finding large homogeneous areas (thus approaching the gray-world assumption, since bright and dark object surfaces tend to compensate each other in the average operation).

However, as previously noted, for white-patch algorithms to perform correctly, the digital image should be as noiseless as possible; thus, they are not indicated for images taken under dim light conditions. Noise generated by poor illumination, instead, does not significantly affect the performances of gray-world algorithms, but they do not work properly for close-ups of uniform regions, where the contrast is poor. In these unfavorable cases, the methods tend to return an incorrect illuminant estimation, resulting in an estimated reflectance that is too saturated to white or to gray, respectively.

To minimize the drawbacks and capitalize on the assets of the white-patch and gray-world methods, Finlayson and Trezzi [FIN 04] and Gijsenij and Gevers [GIJ 07] studied two frameworks, in which the white-patch and gray-world methods can be combined.

Let us describe the proposal of Finlayson and Trezzi that is based on a simple, yet informative, observation. Consider the L^p-norm of the image function $I_c : \Omega \to [0, 1]$, which is well defined for all $p \geq 1$ because I_c is bounded and Ω is compact, i.e.

$$||I_c||_p = \left(\int_\Omega I_c(x)^p \, dx \right)^{1/p}, \qquad [2.17]$$

then, $||I_c||_\infty = \max_{x \in \Omega}\{I_c(x)\}$ and $||I_c||_1 = |\Omega|\overline{I_c}$. If we compare these expressions with equations [2.9] and [2.15], we find that:

$$L_c^{\mathrm{WP}} = ||I_c||_\infty \text{ and } L_c^{\mathrm{GW}} = \frac{||I_c||_1}{k|\Omega|}, \qquad \forall c \in \{R, G, B\}. \qquad [2.18]$$

Hence, it is reasonable to think that if we use intermediate values of p between $p = 1$ (gray-world) and $p = \infty$ (white-patch) to estimate L_c, then we obtain intermediate results between the gray-world and white-patch methods. For this reason, Finlayson and Trezzi called this method “shades of gray”. They defined the L^p-norm illuminant estimation for $1 \leq p \leq \infty$ as follows: $L_{c,p} = k_p||I_c||_p$, where k_p plays the role of k in equation [2.15], but with respect to the L^p-norm.

In this case, the reflectance is postulated after the aforementioned mathematical observation as follows:

$$S_{c,p}(x) = \frac{I_c(x)}{k_p||I_c||_p}. \qquad [2.19]$$

Finlayson and Trezzi showed that, on the database [BAR 02], the best performances are obtained with $p = 6$; however, the optimal value of p can change from one database to another.

Let us now describe the proposal of Gijsenij and Gevers [GIJ 07]. They refined the pre-processing idea of [BAR 02] by considering the original image at different scales. The multi-scale approach is built through the convolution of the original image using a Gaussian kernel with the standard deviation σ: $I_c^\sigma \equiv I_c * G^\sigma$.

We have two limit behaviors: the finest scale, $\sigma = 0$, in which the convolution has no effect at all, i.e. $I_c^{\sigma=0} = I_c$, and the coarsest scale, $\sigma \to +\infty$, in which the convolution reduces to a homogeneous averaging operation, i.e. $I_c^{\sigma\to\infty} \to \int_\Omega I_c(x)\,dx$.

Gijsenij and Gevers postulate illuminant and reflectance estimation as follows:

$$L_{c,\sigma} = k_c \max_{x\in\Omega}\{I_c^\sigma(x)\} \quad \text{and} \quad S_{c,\sigma}(x) = \frac{I_c(x)}{k_c \max_{x\in\Omega}\{I_c^\sigma(x)\}}, \qquad [2.20]$$

$\forall c \in \{R, G, B\}$, $\forall x \in \Omega$, where k_c plays the role of k in equation [2.15], but with respect to I_c^σ. It can be seen that this technique combines the max-RGB method with equation [2.20], and the gray-world technique by using I_c^σ instead of I_c.

The results of this method are similar to those of the shades of gray model and out-perform those of the pure white-patch and gray-world methods. The major disadvantage is that the scale parameter σ, analogously to p in the shades of gray algorithm, depends on the database of images under examination.

2.2.4. *Gray-edge assumption and related models*

Referencing the gray-edge assumption in [WEI 07], it is stated that "*the average of the reflectance differences in a scene is achromatic (gray)*". As stated by the authors, this hypothesis originates from an *empirical observation*: the plot of the color derivative distribution of an image approximates an ellipsoid whose longest axis coincides with that of the light source color [WEI 06]. So, if this axis is rotated with respect to that of neutral light, it means that the illuminant has a non-neutral color.

To compute reflectance differences, the authors consider the spatial derivative $\partial_x S$ of the reflectance function $S(x, \lambda)$ and translate the gray-edge hypothesis as follows:

$$\frac{1}{|\Omega|}\int_\Omega |\partial_x S(x,\lambda)|\, dx = k, \qquad \forall \lambda \in \Lambda, \tag{2.21}$$

where $|\ |$ is the Frobenius norm and k is a suitable constant that depends on the space in which color differences are represented [WEI 07]. In other words, the total variation of the reflectance function in every chromatic channel must be constant.

The illuminant estimation with this new proposal can be obtained by the following computations:

$$\begin{aligned}\overline{|\partial_x I_c|} &\equiv \frac{1}{|\Omega|}\int_\Omega |\partial_x I_c(x)|\, dx = \frac{1}{|\Omega|}\int_\Omega \left(\int_\Lambda |\partial_x S(x,\lambda)| E(\lambda) R_c(\lambda)\, d\lambda\right) dx \\ &= \int_\Lambda \left(\frac{1}{|\Omega|}\int_\Omega |\partial_x S(x,\lambda)|\, dx\right) E(\lambda) R_c(\lambda)\, d\lambda = k L_c,\end{aligned} \tag{2.22}$$

where we have used the definition of L_c and the gray-edge hypothesis in the last step of the computation.

Consequently, the illuminant and reflectance estimation with the gray-edge (GE) assumption is given by:

$$L_c^{\mathrm{GE}} = \frac{\overline{|\partial_x I_c|}}{K}, \quad S_c^{\mathrm{GE}}(x) = k\frac{I_c(x)}{\overline{|\partial_x I_c|}}. \tag{2.23}$$

The considerations of section 2.2.2 can be translated here, with the only difference being that the role of $\overline{I}_c$ here will be played by $\overline{|\partial_x I_c|}$.

The framework presented above can be generalized by considering the n-th derivative, $n \geq 1$, i.e. by formulating the following hypothesis [WEI 07]:

$$\frac{1}{|\Omega|}\int_\Omega \left|\partial_x^n S(x,\lambda)\right|\, dx = k_n, \tag{2.24}$$

where, again, k_n plays the same role as k in equation [2.15]. Using the same arguments as above, the illuminant estimation in this case is given by:

$$L_c^{\mathrm{GE},n} = \frac{\overline{|\partial_x^n I_c|}}{k_n}. \qquad [2.25]$$

If hypothesis [2.6] is satisfied, the reflectance estimation is given by:

$$S_c^{\mathrm{GE},n}(x) = k_n \frac{I_c(x)}{\overline{|\partial_x^n I_c|}}. \qquad [2.26]$$

In [WEI 07], it is shown that the value of n that corresponds to the best performances depends on the database chosen. In the next section, we will show how all the previous methods can be fused into a single one.

2.2.5. *Multi-scale n-th order shades of gray-edge assumption: a general hypothesis*

All the assumptions described in the previous sections can be fused into a single one, as shown in [WEI 07]. Joining the names of all the previous ones, it seems reasonable to call this assumption the "multi-scale n-th order shades of gray-edge assumption":

$$\left(\frac{1}{|\Omega|}\int_\Omega \left|\partial_x^n \rho^\sigma(x,\lambda)\right|^p \, dx\right)^{1/p} = k_{n,\sigma,p}, \qquad [2.27]$$

where $\partial_x^n \rho^\sigma = \rho * \partial_x^n G^\sigma$, with G^σ being a Gaussian with the standard deviation σ. $k_{n,\sigma,p}$ is a constant for a fixed value of the parameters n (the order of the spatial derivative), σ and p.

Following the same arguments as in the previous sections, we find that the illuminant estimation provided by the method that uses this generalized assumption is given by:

$$L_c^{p,n,\sigma} = \frac{\|\partial_x^n I_c^\sigma\|_p}{k_{n,\sigma,p}}, \qquad [2.28]$$

where $\partial_x^n I_c^\sigma = I_c * \partial_x^n G^\sigma$.

If hypothesis [2.6] is satisfied, the estimated reflectance in this case is given by:

$$S_c^{p,n,\sigma}(x) = k_{n,\sigma,p} \frac{I_c(x)}{\|\partial_x^n I_c^\sigma\|_p}. \qquad [2.29]$$

For the sake of clarity, we recall the meaning of the three parameters p, n, σ:

– $1 \leq p \leq \infty$ determines which L^p-norm is used in the computation: if we choose $p \to \infty$, we emphasize the influence of large values of $I_c(x)$ (white-patch-like behavior); if we choose $p = 1$, all the values of $I_c(x)$ influence the computation in the same way (gray-world-like behavior);

– $0 \leq n < \infty$ is the derivative order: $n = 0$ corresponds to a shades of gray algorithm and $n > 1$ to a gray-edge one;

– $0 \leq \sigma \leq \infty$ is the scale at which the image is considered, the bigger it is, the coarser the scale.

We refer to [GIJ 11] and [WEI 07] for a thorough discussion of the performances of this algorithm as its parameters vary.

3

Retinex-Like Algorithms for Color Image Processing

Edwin H. Land coined the term “Retinex” in his 1964 paper [LAN 64], even if the most popular paper about Retinex is the one that he published with John J. McCann in 1971 [LAN 71]. Retinex stands for “Retina plus Cortex”, which refers to the fact that the mechanisms underlying human color vision depend both on the retinal photoreceptor catches and on the cortex interpretation of these signals. The original Retinex is a computational model developed with the aim of finding a perceptual correlate of reflectance, called “lightness” by Land, to be tested with psychophysical measurements [MCC 70].

Through a series of ground-breaking experiments, mostly performed with the famous “Mondrian tableaux”, as the one shown in Figure 3.1, Land and McCann proved that human perception of a surface’s color is much more influenced by the spatial distribution of the surrounding surfaces than by the spectral distribution of the light used to illuminate the Mondrian tableau. As underlined by McCann in many papers and conference speeches, spatial locality of color perception is the central concept in the whole Retinex theory. Thus, at least in its original form, the aim of Retinex is not to discard illumination and recover the intrinsic reflectance of surfaces, as several authors claim in their paper even nowadays, but to quantify how the points of the spatial surround cooperate to modify the color perception of a given spot in a visual scene.

In spite of their innovative and important experimental achievements, neither Land nor McCann “carved their model into stone” through a rigorous

Computational Color Science: Variational Retinex-like Methods, First Edition. Edoardo Provenzi.

mathematical formulation. To the author’s knowledge, the first explicit Retinex formula that Land wrote appeared in the paper [LAN 83], which was partially formalized in [BRA 86], too late to prevent many other authors from diverging with respect to the first version. In the following section, we provide a formalization of the original Retinex formula. This will help us fix the ideas about many concepts and notations that will be used later on.

Figure 3.1. *Digital reproduction of a typical Mondrian tableau used by Land and McCann for their color matching experiments. For a color version of the figure, see www.iste.co.uk/provenzi/color.zip*

3.1. Mathematical description of the original ratio-threshold-reset Retinex algorithm

As mentioned previously, the original Retinex model of Land and McCann [LAN 71] is based on the assumption that the HVS operates with three retinal-cortical systems, each processing the low, middle and high wavelengths of the visible electromagnetic spectrum independently. Every independent process forms a separate image that determines a quantity that they called *lightness* and denoted as L. Inspired by several matching experiments (see, e.g., [MCC 70, LAN 71]), Land and McCann found a computational way to reproduce lightness for their Mondrian tableaux by introducing spatial comparisons among intensities, calculated over *paths*. The comparison is performed through a multiplicative chain of ratios, subjected to these nonlinear mechanisms[1]:

– *Threshold mechanism*: if the ratio does not differ from 1 by more than a fixed threshold value, then it is set to be unitary;

– *Reset mechanism*: if the cumulated product of ratios overcomes the value 1 at a certain point of the path, then it is forced to be 1, so that the computation restarts from it. In this way, this point becomes a local white reference, so the reset mechanism is responsible for the white-patch behavior of Retinex.

Let us now present the mathematical formalization of Land and McCann's ratio-threshold-reset Retinex computation provided in [PRO 05]. Given a discrete digital image function with a normalized range, $I : \Omega \subset \mathbb{Z}^2 \to [0,1]$, let us consider a collection of N oriented paths $\vec{\gamma} = \{\gamma_1, \dots, \gamma_N\}$ composed of ordered chains of pixels starting in y_k and ending in x, $k = 1, \dots, N$. Let n_k be the number of pixels traveled by the path γ_k and let $t_k = 1, \dots, n_k$ be its parameter, i.e. $\gamma_k : \{1, \dots, n_k\} \to \Omega \subset \mathbb{R}^2$, $\gamma_k(1) = y_k$ and $\gamma_k(n_k) = x$. For the sake of simplicity, let us write two subsequent pixels of the path as $\gamma_k(t_k) = y_{t_k}$ and $\gamma_k(t_k + 1) = y_{t_k+1}$, for $t_k = 1, \dots, n_k - 1$. In every fixed chromatic channel $c \in \{R, G, B\}$, let us consider their intensities $I(y_{t_k})$, $I(y_{t_k+1})$ and then compute the ratio $R_{t_k} = \frac{I(y_{t_k+1})}{I(y_{t_k})}$ with the initial condition $R_0 = 1$.

With this notation in mind, the value of lightness provided by the ratio-threshold-reset Retinex algorithm for a generic pixel $x \in \Omega$, in every fixed chromatic channel c (that we avoid specifying for the sake of a clearer notation), is given by:

$$L_{\varepsilon,\vec{\gamma}}(x) = \frac{1}{N} \sum_{k=1}^{N} \prod_{t_k=1}^{n_k-1} \delta_k(R_{t_k}) \qquad [3.1]$$

---

[1] A further mechanism, called *scaling*, can be introduced [LAN 77]. For the sake of a clearer description of Retinex, we will avoid considering this mechanism in this chapter and will introduce it in Chapter 5.

where $\delta_k : \mathbb{R}^+ \longrightarrow \mathbb{R}^+$, $k = 1, \ldots, N$, are functions defined in this way: $\delta_k(R_0) = 1$ and, for $t_k = 1, \ldots, n_k - 1$,

$$\delta_k(R_{t_k}) = \begin{cases} R_{t_k} & \text{if } 0 < R_{t_k} \leq 1 - \varepsilon \\ 1 & \text{if } 1 - \varepsilon < R_{t_k} < 1 + \varepsilon \\ R_{t_k} & \text{if } 1 + \varepsilon \leq R_{t_k} \leq \frac{1+\varepsilon}{\prod_{m_k=0}^{t_k-1} \delta_k(R_{m_k})} \\ \frac{1}{\prod_{m_k=0}^{t_k-1} \delta_k(R_{m_k})} & \text{if } R_{t_k} > \frac{1+\varepsilon}{\prod_{m_k=0}^{t_k-1} \delta_k(R_{m_k})} \end{cases} \qquad [3.2]$$

with $\varepsilon > 0$ being a fixed threshold.

The first option is satisfied when the intensity of the pixel y_{t_k+1} is appreciably smaller than the intensity of the pixel y_{t_k}, and then δ_k reproduces the value of the ratio R_{t_k}. The second option occurs when only a very small change in intensity is measured between two subsequent pixels. In this case, $\delta_k(R_{t_k})$ is defined to be 1, so that the product of ratios remains exactly the same as in the previous step. This is the mathematical implementation of the threshold mechanism.

The third option is referred to the case when the ratio R_{t_k} is greater than $1 + \varepsilon$, but the product $\delta_k(R_1)\delta_k(R_2) \cdots \delta_k(R_{t_k-1})R_{t_k}$ is not greater than $1 + \varepsilon$. In this case, δ_k reproduces the value of R_{t_k} as in the first option. Finally, the fourth option holds when $\delta_k(R_1)\delta_k(R_2) \cdots \delta_k(R_{t_k-1})R_{t_k} > 1 + \varepsilon$. In this case, δ_k resets the chain of product to 1 because a "local white pixel" has been reached. This option implements the reset mechanism (and so the white-patch behavior) of the algorithm.

It is useful to write the contribution of the single path γ_k to $L_{\varepsilon,\vec{\gamma}}(x)$ as:

$$L_{\varepsilon,\gamma_k}(x) = \prod_{t_k=1}^{n_k-1} \delta_k(R_{t_k}), \qquad [3.3]$$

so that formula [3.1] simply reduces to the average of these contributions, i.e. $L_{\varepsilon,\vec{\gamma}}(x) = \frac{1}{N} \sum\limits_{k=1}^{N} L_{\varepsilon,\gamma_k}(x)$.

Since the logarithmic function transforms products into sums and divisions into subtractions, the computational cost of the algorithm defined by formula 3.1 can be reduced via the decomposition of the identity function on $\mathbb{R}^+$ as $\exp \circ \log$ applied to the product of ratios, i.e.

$$L_{\varepsilon,\vec{\gamma}}(x) = \frac{1}{N}\sum_{k=1}^{N} \exp\left(\sum_{t_k=1}^{n_k-1} \log(\delta_k(R_{t_k}))\right). \qquad [3.4]$$

We can simplify the formula by defining $\tilde{I}(y_{t_k}) = \log(I(y_{t_k}))$, $\tilde{R}_{t_k} = \log R_{t_k} = \tilde{I}(y_{t_k+1}) - \tilde{I}(y_{t_k})$, $\tilde{R}_0 = 0$. We define the functions δ_k to be: $\tilde{\delta}_k(\tilde{R}_0) = 0$ and, for $t_k = 1, \ldots, n_k - 1$,

$$\tilde{\delta}_k(\tilde{R}_{t_k}) = \begin{cases} \tilde{R}_{t_k} & \text{if } -\infty < \tilde{R}_{t_k} \leq -\tilde{\varepsilon} \\ 0 & \text{if } -\tilde{\varepsilon} < \tilde{R}_{t_k} < \tilde{\varepsilon} \\ \tilde{R}_{t_k} & \text{if } \tilde{\varepsilon} \leq \tilde{R}_{t_k} \leq \tilde{\varepsilon} - \sum_{m_k=0}^{t_k-1} \tilde{\delta}_k(\tilde{R}_{m_k}) \\ -\sum_{m_k=0}^{t_k-1} \tilde{\delta}_k(\tilde{R}_{m_k}) & \text{if } \tilde{R}_{t_k} > \tilde{\varepsilon} - \sum_{m_k=0}^{t_k-1} \tilde{\delta}_k(\tilde{R}_{m_k}) \end{cases} \qquad [3.5]$$

with $\tilde{\varepsilon} = \log(1+\varepsilon)$. If we use these notations, the formula for the lightness can be written as:

$$L_{\varepsilon,\vec{\gamma}}(x) = \frac{1}{N}\sum_{k=1}^{N} \exp\left(\sum_{t_k=1}^{n_k-1} \tilde{\delta}_k(\tilde{R}_{t_k})\right), \qquad [3.6]$$

which contains only one exponential, sums and differences. For small values of ε, it coincides with the lightness of the non-logarithmic formulation.

3.2. Analysis of the ratio-reset Retinex formula: the limit $\varepsilon \to 0$

The analytical formula that describes the ratio-threshold-reset Retinex algorithm introduced above permitted making predictions about the model. As explained in [PRO 05], this can be done if the threshold mechanism is disregarded or, equivalently, by considering the case $\varepsilon \to 0$.

As $\varepsilon \to 0$, the functions δ_k become much simpler:

$$\delta_k(R_{t_k}) = \begin{cases} R_{t_k} & \text{if } 0 < R_{t_k} \prod_{m_k=0}^{t_k-1} \delta_k(R_{m_k}) \leq 1 \\ \dfrac{1}{\prod_{m_k=0}^{t_k-1} \delta_k(R_{m_k})} & \text{if } R_{t_k} \prod_{m_k=0}^{t_k-1} \delta_k(R_{m_k}) > 1 \end{cases} \qquad [3.7]$$

hence, when $\varepsilon \to 0$, δ_k behaves either as the identity function or as the reset function.

For the sake of a simpler and more comprehensible notation, we shall eliminate the suffix k for a moment, and focus attention on a given path γ starting in $\gamma(1) = y$ and ending in $\gamma(n) = x$. Let H be the value of the parameter of γ, such that $\gamma(H) = y_H$ is the pixel with highest intensity in the whole path.

If we write the contribution of γ explicitly as

$$\delta\left(\frac{I(y_2)}{I(y)}\right)\cdots\delta\left(\frac{I(y_H)}{I(y_{H-1})}\right)\delta\left(\frac{I(y_{H+1})}{I(y_H)}\right)\cdots\delta\left(\frac{I(x)}{I(y_{n-1})}\right) \qquad [3.8]$$

we can prove that the pixel y_H enables the reset mechanism. In fact, if no reset occurs before y_H, then we have:

$$\frac{I(y_2)}{I(y)}\frac{I(y_3)}{I(y_2)}\cdots\delta\left(\frac{I(y_H)}{I(y_{H-1})}\right)\delta\left(\frac{I(y_{H+1})}{I(y_H)}\right)\cdots\delta\left(\frac{I(x)}{I(y_{n-1})}\right) \qquad [3.9]$$

the first ratios cancel out, so that:

$$\frac{I(y_{H-1})}{I(y)}\delta\left(\frac{I(y_H)}{I(y_{H-1})}\right)\delta\left(\frac{I(y_{H+1})}{I(y_H)}\right)\cdots\delta\left(\frac{I(x)}{I(y_{n-1})}\right). \qquad [3.10]$$

Thanks to the hypothesis on y_H, $\frac{I(y_H)}{I(y_{H-1})} > 1$; thus, the product of this ratio with the previous ones reduces to:

$$\frac{I(y_{H-1})}{I(y)}\frac{I(y_H)}{I(y_{H-1})} = \frac{I(y_H)}{I(y)} \qquad [3.11]$$

which is again greater than 1. The reset mechanism is enabled and the chain of products reduces to:

$$\delta\left(\frac{I(y_{H+1})}{I(y_H)}\right)\cdots\delta\left(\frac{I(x)}{I(y_{n-1})}\right). \qquad [3.12]$$

If the reset mechanism is activated by some other pixel before y_H in the path γ, then the conclusion remains true: to verify this, it is sufficient to replace

y with the last pixel that has produced the reset before y_H and then use the same arguments as before.

As a consequence, when $\varepsilon \to 0$, all the pixels composing the path γ before the pixel with highest intensity are totally useless for the lightness computation.

After the pixel y_H, the reset mechanism is inhibited and the δ function simply reduces to the identity. In fact, if all of the ratios remain less than 1 until the end of the path, then the statement is trivially true. Instead, if there exists a pixel y_K, $K > H$, such that $\frac{I(y_{K+1})}{I(y_K)} > 1$, the reset mechanism cannot be enabled because the product of ratios $R_1 \cdots R_K$ reduces to:

$$\frac{I(y_{H+1})}{I(y_H)} \frac{I(y_{H+2})}{I(y_{H+1})} \cdots \frac{I(y_K)}{I(y_{K-1})} \frac{I(y_{K+1})}{I(y_K)} = \frac{I(y_{K+1})}{I(y_H)} < 1. \qquad [3.13]$$

If there are other pixels with the same characteristic as y_K, the conclusion is unchanged. If there is more than one pixel with the same intensity as y_H, then all the considerations mentioned above have to be referred to the last pixel with highest intensity traveled by γ. To resume, when $\varepsilon \to 0$, the contribution of the path reduces simply to $\frac{I(x)}{I(y_H)}$.

Since the arguments presented above work for every path, we can write:

$$L_{0,\gamma_k}(x) = \frac{I(x)}{I(y_{H_k})}, \qquad [3.14]$$

where y_{H_k} is the pixel with highest intensity traveled by γ_k, for every $k = 1, \ldots, N$. Thus, formula [3.1] can be written as follows:

$$L_{0,\vec{\gamma}}(x) = \frac{I(x)}{N} \sum_{k=1}^{N} \frac{1}{I(y_{H_k})}, \qquad [3.15]$$

or

$$L_{0,\vec{\gamma}}(x) = \frac{1}{N} \sum_{k=1}^{N} \exp\left(\tilde{I}(x) - \tilde{I}(y_{H_k})\right), \qquad [3.16]$$

in the logarithmic formulation.

Equation [3.15] shows explicitly that, when $\varepsilon \to 0$, the Retinex lightness is obtained simply by multiplying by $I(x)$ the average of the inverse values of the highest intensities of the pixels traveled by the paths γ_k. Henceforward, we will refer to formula [3.15] as describing the "ratio-reset Retinex algorithm".

Note that the similarity with the von Kries algorithm described in the previous section is evident; however, the presence of paths makes the ratio-reset Retinex a local algorithm, where locality is intrinsically represented by the geometry of paths used. We will turn back to the path dependency of the ratio-reset Retinex in section 3.3 when we will describe the spray-based implementation. Here, we just observe that when $n_k \to |\Omega|$ or $N \to \infty$, the ratio-reset Retinex loses its local properties and reduces to the global diagonal von Kries model [PRO 05]. In contrast, if we use small values of n_k or N, the resulting lightness images are affected by a lot of noise (see again [PRO 05]).

We note that since intensity values are normalized, $0 < I(y_{H_k}) \leq 1$ for every $k = 1, \ldots, N$ and then $\sum_{k=1}^{N} \frac{1}{I(y_{H_k})} \geq N$. It follows that $L(x) \geq I(x)$ for every pixel i, which proves that an image filtered with the ratio-reset Retinex is always brighter or equal to the original one. This shows an important limitation of this algorithm: an over-exposed picture can only be worsened by the application of the ratio-reset Retinex used as a color corrector.

Further interesting information that can be obtained via formula [3.15] is the qualitative behavior of ratio-reset Retinex when it is iteratively applied to an image. Mathematically, the operation of applying m-times Retinex corresponds to the composition of the lightness function with itself m times. The simplest case of $m = 2$ can be written as follows:

$$\begin{aligned} L^2_{0,\vec{\gamma}}(x) = \frac{L_{0,\vec{\gamma}}(x)}{N} \sum_{k=1}^{N} \frac{1}{L_{0,\vec{\gamma}}(y_{H'_k})} \quad &\Leftrightarrow \quad \frac{L^2_{0,\vec{\gamma}}(x)}{L_{0,\vec{\gamma}}(x)} \\ &= \frac{1}{N} \sum_{k=1}^{N} \frac{1}{L_{0,\vec{\gamma}}(y_{H'_k})}, \end{aligned} \qquad [3.17]$$

where $y_{H'_k}$ is the pixel with the highest value of lightness in a given chromatic channel along the path γ_k after the first application of Retinex. We stress that $y_{H'_k}$ is, in general, different from y_{H_k}, which is the pixel with the highest intensity along γ_k before the first filtering operation.

More generally, if we write with $L^m_{0,\vec{\gamma}}$ the composition of $L_{0,\vec{\gamma}}$ with itself m times, it can be immediately seen that:

$$\frac{L^m_{0,\vec{\gamma}}(x)}{L^{m-1}_{0,\vec{\gamma}}(x)} = \frac{1}{N}\sum_{k=1}^{N} \frac{1}{L^{m-1}_{0,\vec{\gamma}}(y_{H_k^{m-1}})} \qquad [3.18]$$

where $y_{H_k^{m-1}}$ is the pixel with the highest value of lightness along the path γ_k after $m-1$ applications of Retinex to the original image.

Equation [3.18] shows that in every iteration of Retinex, the lightness of any pixel x is greater or equal to that of the previous iteration. In fact, $0 < L^{m-1}_{0,\vec{\gamma}}(y_{H_k^{m-1}}) \le 1$, $k = 1, \dots, N$, hence the right-hand side of [3.18] is ≥ 1 and so $L^m(x) \ge L^{m-1}(x)$ for every pixel $x \in \Omega$. In particular, the lightness of x is forced to grow until the right-hand side of equation [3.18] reaches the value 1, but this happens if and only if $L^{m-1}_{0,\vec{\gamma}}(y_{H_k^{m-1}}) = 1$, i.e. when the lightness of (at least) one pixel in all the paths $\gamma_1, \dots, \gamma_N$ reaches the value 1. This is the convergence condition: every further iteration of the ratio-reset Retinex will leave the image unchanged. At a visual level, when the convergence condition is reached, the image is corrupted by "speckling", i.e. the presence of a large number of white spots across the image domain, as can be seen in Figure 3.2.

3.2.1. *Retinex: "a melody that everyone plays differently"*

In image processing, it is hard to find a model whose name has been interpreted in so many different ways as "Retinex". In this subsection, we present a synthetic description of the evolution of the Retinex interpretation. In Chapter 5, we will link these different Retinex implementations to their corresponding variational versions.

Path-wise Retinex shares a local WP nature and mostly differs from each other by the path geometry used to explore spatial locality: Land and McCann used piecewise linear paths in [LAN 71]. In [COO 04], [MAR 00] and [SIM 14], those paths were substituted for double spirals, Brownian paths and traces of a specialized swarm of termites, respectively.

Figure 3.2. *Top to bottom: original image and result of multiple iterations of the ratio-reset Retinex algorithm until the convergence is reached. Note the speckling effect*

Center/surround Retinex are local GW algorithms originating from [LAN 86], where Land noticed that he could reproduce Mach bands formed by a spinning white square on a black background by using a different Retinex formulation. Precisely, for every image point, the intensity of the center x is replaced by the ratio between $I(x)$ and the average value of the surround, sampled with a density that decays as the inverse of the square distance from the center. Writing with L^{CS} this "center/surround lightness", we have:

$$L^{\mathrm{CS}}(x) = \frac{I(y)}{< \{I(y),\, y \in \text{Surround}\} >}, \qquad [3.19]$$

where $< \cdot >$ represents the average operator. Comparing [3.19] with [3.15], it can be seen that there is a fundamental difference between this formulation and the original one: there the ratio is performed over the pixel with highest intensity, while in this formulation it is implemented over the mean value of the surround. We can go further: comparing [3.19], with [2.15], it can be seen that this formulation of Retinex is practically a GW method to remove the illuminant component of the image.

In 1997, Johbson, Rahman and Woodell [JOB 97b] re-elaborated Land's idea presented in [LAN 86]: they worked with logarithmic data, approximating the average of the surround by convolving the image function I with a normalized kernel function F, usually a Gaussian. If we use again, for simplicity, the symbol L^{CS}, we can write this model as follows:

$$L^{\mathrm{CS}}(x) = \log(I(x)) - \log((F * I)(x)), \qquad \forall x \in \Omega. \qquad [3.20]$$

Multi-level Retinex algorithms were pioneered by Frankle and McCann in [FRA 83] and further refined in [FUN 04]. In these works a multi-level version of the original local WP Retinex is presented, the authors abandon paths and consider a computation that takes into account all pixels. The input image is progressively sub-sampled averaging a number of pixel that grows as increasing powers of 2. On each sub-sample level, a ratio-reset computation (without threshold) is operated a certain number of times from the coarser sub-sample level to the finest one. Because of the sub-sampling, as we go further from the target pixel, we do not consider actual pixel values, but average values of macroareas of increasing size. A rigorous mathematical formulation of these multi-level algorithms is still lacking.

Based on this idea, Marini, Rizzi and De Carli [MAR 00] constructed a local WP multi-level version of Brownian path Retinex that reduced the amount of noise in the output images. A different multi-level proposal has been pointed out by Johbson, Rahman and Woodell in [JOB 97a]: they introduced a certain number S of scales where performing the convolutions in [3.20] with normalized Gaussian functions F_s, $s = 1, \ldots, S$. Each scale is associated with a suitable weight w_s, which gives more importance to finer scales than to coarser ones.

Finally, there are WP Retinex versions based on solving a Poisson equation. They rely on a study by Horn [HOR 74], in which he remarkably pointed out, for the first time, the need for a spatially isotropic two-dimensional version of Retinex. Horn considered, as Land, only Mondrian tableaux illuminated by a smoothly varying light. However, differently from Land, he explicitly tackled the ill-posed problem of inverting the equation $I_c(x) = S_c(x)L_c(x)$, $c \in \{R, G, B\}$, with respect to $S_c(x)$ (the reflectance of the point $x \equiv (x_1, x_2)$) knowing only the image intensity $I_c(x)$. If we now pass to logarithmic values, i.e. $\log I_c(x) = \log S_c(x) + \log L_c(x)$ or, equivalently, $\log S_c(x) = \log I_c(x) - \log L_c(x)$, and we apply a differential operator D to both sides, then $D(\log L_c(x))$ will be small but finite everywhere, while $D(\log S_c(x))$ will be different from zero only if x is close to sharp edges.

If we apply a threshold operator δ_T defined as follows:

$$\delta_T(s) = \begin{cases} s & \text{if } |s| > T \\ 0 & \text{elsewhere,} \end{cases}$$

for all $s \in \mathbb{R}$ and if the threshold $T > 0$ satisfies the constraints defines by the following inequality:

$$\max_{x\in\Omega} \{D(\log L_c(x))\} < T < \min \{D(\log S_c(x)),$$
$$x \in \Omega \ : \ D(\log S_c(x)) \neq 0\} \qquad [3.21]$$

then we obtain $D(\log S_c(x)) = \delta_T(D(\log I_c(x)))$. Horn insisted on the choice of the Laplacian for D instead of the gradient, arguing that first order derivatives are one-dimensional, while the second order derivatives involved in the Laplacian are isotropic and thus more suited for the topology of an image. By substituting D for the Laplacian operator Δ, the last formula becomes a Poisson equation:

$$\Delta(\log S_c(x)) = \delta_T(\Delta(\log I_c(x))) \qquad [3.22]$$

whose solution allows recovering the logarithmic reflectance $\log S_c(x)$. It is clear that Horn's method is based on quite restrictive hypotheses: smoothness of illumination (violated by scenes with deep shadows, for instance) and a Mondrian-like world (violated each time edges are not sharp). Blake [BLA 85] refined Horn's results using more suitable boundary constraints when solving Horn's Poisson equation, and Hurlbert pointed out in [HUR 86] a connection between Land's and Horn's versions of Retinex by analyzing Green's technique for the solution of Horn's Poisson equation.

The alternative Retinex interpretations quoted above have been mathematically formalized with the help of variational principles and the theory of partial differential equations. In Chapter 5, these formalizations will be discussed in detail.

3.3. From paths to pixel sprays: RSR

The information obtained, thanks to the mathematical formulation of Retinex, has important consequences for the structure of $\mathcal{P}_x(\Omega)$, the set of paths embedded in the image domain Ω and ending in the point x. After formula [3.15], on this set, it is natural to define the following equivalence relation: given $\gamma, \eta \in \mathcal{P}_x(\Omega)$,

$$\gamma \sim \eta \quad \Leftrightarrow \quad \max_{y \in \gamma^*}\{I(y)\} = \max_{y \in \eta^*}\{I(y)\} \qquad [3.23]$$

where γ^* and η^* are the codomains of the paths, i.e. the collections of pixels traveled by γ and η, respectively.

Paths belonging to different equivalence classes give different contributions to the lightness computation, while every path in a given equivalence class gives rise to the same value of $L_{0,\gamma_k}(x)$. It follows immediately that $\mathcal{P}_x(\Omega)$ contains redundant paths and that the correct set of paths to consider is given by the quotient set $\mathcal{P}_x(\Omega)/\sim$, whose elements are the equivalence classes of paths with respect to the equivalence relation defined in [3.23].

In each equivalence class, we can choose a single representative path to compute $L_{0,\gamma_k}(x)$, in particular, the more efficient one is the two-points path whose codomain is simply given by $\{y_{H_k}, x\}$. Thus, the ordering operations needed to generate the paths are totally unnecessary for the final lightness computation. Moreover, from a mathematical point of view, paths are topological manifolds of dimension 1 embedded in the image, which is a topological manifold of dimension 2, so paths do not really scan local neighborhoods of a pixel, but rather *particular directions* in these neighborhoods. This directional extraction of information can lead to halos or artifacts in the filtered image (see, e.g., [FRA 83]).

The classical implementations of Retinex try to remedy this problem using a large number of paths, but this increases the filtering time and does not really overcome the problem. In conclusion, there are three reasons for which paths are not perfectly suitable for the analysis of locality of color perception within the Retinex model: they are redundant, their ordering is completely unnecessary and they have an inadequate topological dimension.

These considerations led the authors of [PRO 07] to consider two-dimensional objects such as *areas* instead of one-dimensional paths to analyze image locality for an efficient color correction. Roughly speaking, their idea is to implement spatial locality by selecting a fraction of pixels from these areas with a density sample that changes according to a given function of their distance with respect to the target pixel x. Each function generates a different kind of pixel selection around x, leading to different types of "sprays", each of which shows different local filtering properties. The new implementation of the ratio-reset Retinex that follows this idea is called RSR for "Random Sprays Retinex".

In RSR the role of a path γ_k traveling n_k pixels and *ending* in the target x is played by $S_k(x)$, a spray with n_k pixels *centered* in x. Actually, once the number of points per spray is chosen, there is no need to vary it with k, hence, from now on, we will write n instead of n_k to denote the number of pixels per spray. The ratio-reset operation along a path is substituted for the search of the pixel with highest intensity in the whole spray. The functional expression of formula [3.14] to compute the lightness remains exactly the same in both algorithms, so the ratio-reset Retinex and RSR share the same intrinsic properties.

$S_k(x)$ is built as follows: starting with a *uniform random distribution* of n values in the real unit interval $[0, 1]$, we extend it to the intervals $[0, 2\pi)$ and $[0, R]$, where R is a given positive real number that will represent the radius of the spray. We denote the corresponding uniform random distributions by $\textsc{rand}_n[0, 2\pi]$ and $\textsc{rand}_n[0, R]$, respectively. Then, if (x_1, x_2) are the coordinates of x, we can define the polar coordinates of a generic pixel $y \equiv (y_1, y_2)$ belonging to $S_k(x)$ in this way:

$$\begin{cases} y_1 = x_1 + \rho\, \cos(\theta) \\ y_2 = x_2 + \rho\, \sin(\theta) \end{cases} \qquad [3.24]$$

where $\rho \in \textsc{rand}_n[0, R]$ and $\theta \in \textsc{rand}_n[0, 2\pi)$. These are the coordinates of pixels that have an isotropic *angular* distribution in a circle of radius R centered in the pixel x.

However, note that the *radial* density is not isotropic; in fact, the spray results are denser near the target pixel x than far away. To compute $\delta(r)$, the mean areolar density variation in function of r, consider any circle C_r of arbitrary radius r, $0 < r \leq R$, centered in x. The area of C_r is $A = \pi r^2$, so $r = \sqrt{\frac{A}{\pi}}$; moreover, since we are dealing with uniform random distributions, the mean number of points inside C_r is $n\frac{r}{R} = \frac{n}{R}\sqrt{\frac{A}{\pi}}$. Computing the derivative of this expression with respect to A, we get the rate of change of the average areolar density:

$$\frac{d\left(\frac{n}{R}\sqrt{\frac{A}{\pi}}\right)}{dA} = \frac{n}{2R\sqrt{\pi A}} \qquad [3.25]$$

but $A = \pi r^2$, so:

$$\delta(r) = \left(\frac{n}{2\pi R}\right)\frac{1}{r}. \qquad [3.26]$$

Thus, the mean areolar density of spray pixels decreases as the inverse radius. Figure 3.3 shows an example of such a spray with 400 points and radius $R = 1$. The radial areolar density decay can be modified by applying a function to ρ. More information about this use of RSR to study the dependence of Retinex on spatial locality can be found in [PRO 07].

In [GIA 14], the RSR sampling technique has been studied from a probabilistic point of view, resulting in the algorithm QBRIX.

3.3.1. *LRSR and SMRSR*

In this section, we will discuss two techniques proposed in [BAN 13, BAN 15] that have been applied to RSR with the aim of reducing the noise in the output image and also decreasing the computational time.

Let us start by describing the strategy described in [BAN 13] and called "Light Random Sprays Retinex" (LRSR) devised to avoid noise formation when a small value of n and/or N is used. Consider an arbitrary input image I

and apply RSR to it, obtaining the image R. The ratio $C = \frac{I}{R}$ is called the intensity change image. In LRSR, the noise is reduced through a convolution with a kernel function k. This can be done after the computation of C, obtaining $C'_k = (C * k)(x)$, $\forall x \in \Omega$, or before it, i.e. applying the blurring to I and R, obtaining $C''_k(x) = \frac{(I*k)(x)}{(R*k)(x)}$, $\forall x \in \Omega$. By combining the two approaches, i.e. filtering before and after calculation with two (possibly identical) kernels k_1 and k_2, respectively, we can define the new intensity change matrix: $C^*_{k_1,k_2}(x) = (C''_{k_1}(x) * k_2)(x)$.

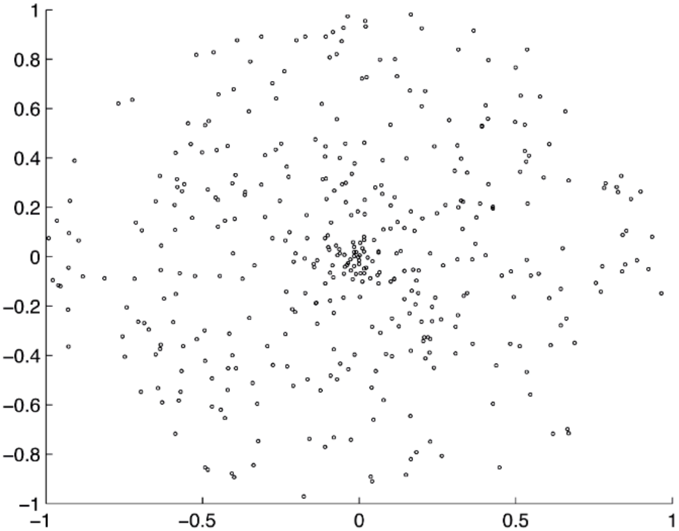

Figure 3.3. *Example of a random spray with 400 points and unitary radius*

The output image O of LRSR is calculated via the formula:

$$O(x) = \frac{I(x)}{C^*_{k_1,\,k_2}(x)} \quad \forall x \in \Omega, \qquad [3.27]$$

the size of the kernels k_1 and k_2 used in [BAN 13] is 25×25.

In [BAN 15], the same authors attacked the problem of computational complexity reduction with a technique called "Smart Light Random Memory Sprays Retinex" (SLRMSR). The basic concept behind SLRMSR is that of "spray memory", which consists of creating a single spray that will be gradually modified while we browse the image. First of all, we extend the image by mirror symmetry to correctly treat pixels that lie near the edge of the image domain. We then consider the first pixel $x \equiv (1, 1) \in \Omega$ of the input image and we build a spray $S(x)$ with n pixels centered in x. We then pass to the subsequent pixel in the same row, i.e. $x' \equiv (2, 1)$, and we *modify just one pixel* of $S(x)$, by randomly selecting a pixel that lies in the neighborhood of x'. By iterating this procedure, we will gradually and smoothly modify the content of each spray. At a computational level, if we store the pixels of the spray in a hyper-matrix, for each new pixel we will just modify the last element of this matrix. Thereby, the spray will be totally renewed every n pixels.

Note that, thanks to this idea, the computational complexity passes from $O(nN|\Omega|)$ to $O(n|\Omega|)$ because now one spray is used. When this technique is applied directly without the filtering strategy quoted above, it produces results affected by horizontal lines, as shown in Figure 3.4 (middle). The main reason is to be found in the great deal of information redundancy in natural images, i.e. the fact that nearby pixels are very likely to have similar values, unless they lie in the proximity of a sharp edge, thus, if we change only one pixel spray at the time and we browse the image horizontally, this kind of problem is to be expected.

3.4. A psychophysical method to measure (achromatic) induction

One of the aims of the RSR model was the investigation of the effects of spatial locality on the computed lightness. It thus seems pertinent to discuss here the Rudd-Zemach model of achromatic induction, which, as the authors say, shares some similarities with Retinex.

The first quantitative measure of achromatic induction was performed by [WAL 48]. In his classical experiment (Figure 3.5), Wallach considered two disks, D_T and D_M for *Target* and *Match*, surrounded by two rings R_T and R_M, embedded in a uniform background B. Let us denote L_{D_M}, L_{R_M}, L_{D_T}, L_{R_T} and L_B as the luminance values of D_M, R_M, D_T, R_T and B, respectively. He showed this configuration to a set of observers adapted to the light conditions of a dimly illuminated room, keeping L_{D_T} and L_{R_M} fixed, using L_{R_T} as an independent variable that he could fix in every experiment and L_{D_M} as a dependent variable that the observers could adjust in order to achieve a perceptual match between the two disks T and M. The stimuli presented to the observers did not have chromatic components.

Figure 3.4. Top*: original image.* Middle*: output of spray memory RSR without applying the filters of LRSR.* Bottom*: output of SLMRSR. Top (original) image courtesy of N. Banić. For a color version of the figure, see www.iste.co.uk/provenzi/color.zip*

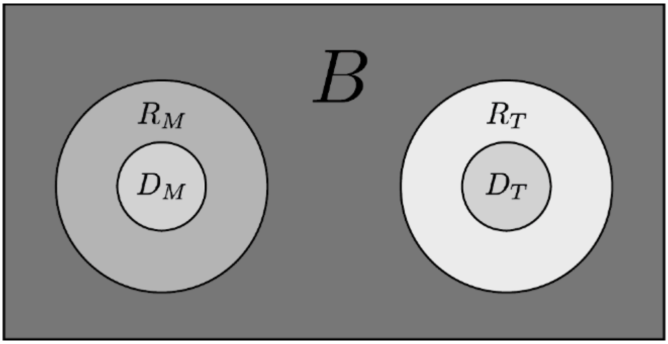

Figure 3.5. *Wallach's classical experiment. Over a uniform background B, there are two inner disks, D_T and D_M (T and D for* Target *and* Match*, respectively), surrounded by two external rings R_T and R_M*

If the luminance of the surrounding rings failed to influence the perception of the achromatic color of the disks, then the match between the two disks would simply be the *photometric* one, i.e. $L_{D_M} = L_{D_T}$; instead, Wallach found that a fairly good match among the achromatic color of the two disks was obtained when the ratios between the disk and the ring luminances were identical on the two sides of the display, i.e.

$$\frac{L_{D_M}}{L_{R_M}} = \frac{L_{D_T}}{L_{R_T}}, \qquad [3.28]$$

a formula called *Wallach's Ratio rule*. By taking the logarithms at both sides and solving for L_{D_M} we find:

$$\log L_{D_M} = \log L_{D_T} + \log L_{R_M} - \log L_{R_T}, \qquad [3.29]$$

thus, according to Wallach's Ratio rule, the plot of the perceptual match in the plane of coordinates $(x, y) = (\log L_{R_T}, \log L_{D_M})$ should be a straight line with slope -1, against the slope 0 that a photometric match would measure. More recent measures using the classical Wallach's experiment have shown that this slope is actually between -1 and 0, as can be seen in Figure 3.6 (adapted from Rudd & Zemach [RUD 04]).

To account for these new psychophysical data, Rudd and Zemach [RUD 04] have proposed a more sophisticated model than Wallach's. They repeated Wallach's experiment adding a non-black background B. As in

Wallach's experiment, L_{D_T} and L_{R_M} are fixed and the observer's task is to adjust L_{D_M} to achieve an achromatic color match to the test disk as a function of L_{R_T}. L_{R_T} is varied from trial to trial by sampling from a set of six luminance values spaced equally in RGB units from 2.54 to 6.31 cd/m^2 (note that Rudd and Zemach used the base 10 for their logarithmic values, so that the logarithmic range goes from 0.405 to 0.800 cd/m^2).

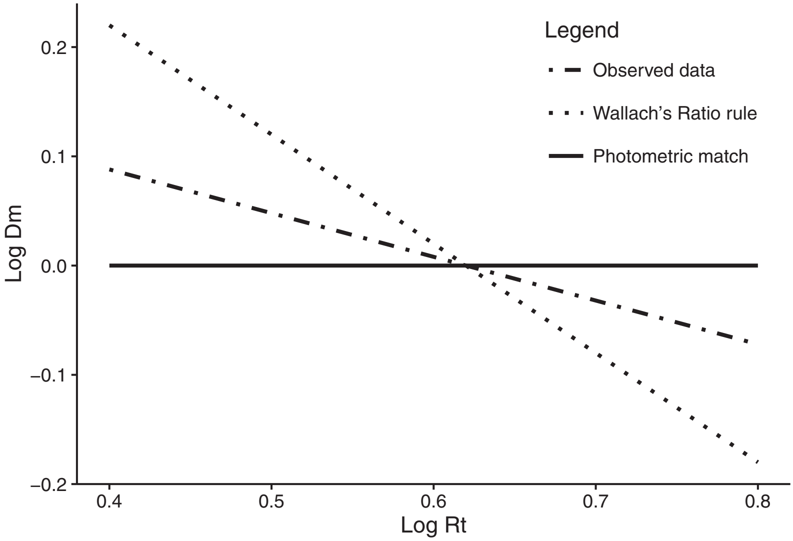

Figure 3.6. *Quantitative measures of Wallach's achromatic color induction experiment for four observers performed in [RUD 04]. The best-fit regression line slopes and associated 95% confidence limits observed by [RUD 04] for the four subjects of the experiment are the following: –0.639 ± 0.033, –0.791 ± 0.034, –0.723 ± 0.047 and –0.657 ± 0.042*

Rudd and Zemach also pointed out some similarities between their model of achromatic induction and Retinex; however, they did not consider the threshold and reset mechanisms. Their model can be described as follows: let L_i and L_j be the luminance of two points i and j in an image, the ratio $\frac{L_i}{L_j}$ can be decomposed as a sequential multiplication of the local luminance ratios at borders encountered along a path connecting j and i, for instance:

$$\frac{L_i}{L_j} = \prod_{k=i}^{j-1} \frac{L_k}{L_{k+1}}, \qquad [3.30]$$

by taking the logarithm at both sides we get

$$\log \frac{L_i}{L_j} = \sum_{k=i}^{j-1} \log \frac{L_k}{L_{k+1}}. \qquad [3.31]$$

Rudd and Zemach introduced *induction strength weights* w_k in order to take into account the fact that patches that lie in a nearby surround have a stronger influence on the induced perception than those that are far away, i.e. spatial locality of vision. Note that in the configuration shown in Figure 3.5, we have $i = D_M$, $i+1 = j-1 = R_M$, $j = B$ on the left part of the visual field and $i = D_T$, $i + 1 = j - 1 = R_T$, $j = B$ on the right part. The *logarithmic brightness of* i, which we denote as $\log\,\Phi(i)$, and which can be inferred by Rudd and Zemach's model, is the following:

$$\log\,\Phi(i) \equiv \sum_{k=i}^{j-1} w_{k-i+1} \log \frac{L_k}{L_{k+1}} + \mu, \qquad [3.32]$$

where $\mu \in \mathbb{R}$ is an arbitrary constant that will be eliminated by the matching procedure and that we introduced to underline the fact that brightness perception is relative to a context and not absolute.

It can be seen that if the luminances L_k and L_{k+1} are equal, then their ratio does not give any contribution to $\Phi(i)$. A meaningful contribution to $\Phi(i)$ is given only by the luminances of points lying at the border of an edge. So, $\Phi(i)$ represents the summed influence of all the edges present within the spatial surround of the target point, suitably weighted. The weight index is $k - i + 1$, which means that small values of the index refer to patches close to i and vice versa. With this convention, and invoking the fact that induction strength decreases with the distance, as proven by [WAL 63], we have that $w_1 > w_2 > \ldots$, i.e. $\frac{w_2}{w_1} < 1$ and so on.

Rudd and Zemach called their model of achromatic induction "Weighted Log Luminance Ratio" (WLLR). The WLLR predicts that the brightness match between L_{D_M} and L_{D_T} is attained when $\Phi(D_M) = \Phi(D_T)$, i.e.

$$w_1 \log \frac{L_{D_M}^{\text{Match}}}{L_{R_M}} + w_2 \log \frac{L_{R_M}}{L_B} + \mu = w_1 \log \frac{L_{D_T}}{L_{R_T}} + w_2 \log \frac{L_{R_T}}{L_B} + \mu, \qquad [3.33]$$

solving this equation w.r.t., $\log L_{D_M}$ we have:

$$\log\, L_{D_M}^{\text{Match}} = \log L_{D_T} + \left(1 - \frac{w_2}{w_1}\right) \log L_{R_M} - \left(1 - \frac{w_2}{w_1}\right) \log L_{R_T}, \qquad [3.34]$$

$L_{D_M}^{\text{Match}}$ is the luminance value of D_M selected by the observer to match L_{D_T}. If we set $u = \log L_{D_M}^{\text{Match}}$, $\alpha = \log L_{D_T} + \left(1 - \frac{w_2}{w_1}\right) \log L_{R_M}$, $\beta = -\left(1 - \frac{w_2}{w_1}\right)$ and $v = \log L_{R_T}$, then the WLLR model predicts the following *linear behavior in the logarithmic domain*:

$$u = \alpha + \beta v, \qquad [3.35]$$

with a slope $\beta = -\left(1 - \frac{w_2}{w_1}\right) \in (-1, 0)$, which is coherent with Rudd and Zemach's empirical observations. In fact, the estimations of the ratio $\frac{w_2}{w_1}$ from their interpolated data for the four observers are: 0.361, 0.209, 0.277 and 0.343.

A key assumption of *edge integration models*, like the WLLR, is that the total achromatic color induction produced by a complex surround is *the sum of the individual induction effects* produced by the luminance borders comprising that surround. Rudd and Zemach performed experiments to directly test this assumption by predicting and then measuring the magnitude of the total induction effect produced by combining three circular edges located at different distances from the test disk. This was done after first measuring the magnitudes of the induction effects produced by the individual edges. The results were in accordance with the predictions of the model.

In section 5.4, we will reinterpret the WLLR model in terms of variational principles.

3.5. Automatic Color Equalization: ACE

Automatic Color Enhancement (ACE) [RIZ 03] is an algorithm for color image enhancement inspired by the HVS features. ACE, like Retinex, transforms the intensity of an image in a local, differential and nonlinear way. To show how ACE works, it is worthwhile to present its formulae and then discuss their meaning. Keeping the notations used for Retinex, let us fix a target pixel x and let y denote the generic pixel in the rest of the image. Given a fixed real constant $\alpha > 1$, we construct the following odd function: $\mathrm{s}_\alpha : [-1, 1] \to [-1, 1]$,

$$\mathrm{s}_\alpha(t) = \begin{cases} -1 \text{ if } -1 \leq t \leq -\frac{1}{\alpha} \\ \alpha t \text{ if } -\frac{1}{\alpha} < t < \frac{1}{\alpha} \\ +1 \text{ if } \frac{1}{\alpha} \leq t \leq 1 \end{cases} \qquad [3.36]$$

α and s_α are called, respectively, slope and slope function. We are interested in the analysis of s_α when t assumes the values $t = I(x) - I(y)$, i.e. we will deal with $\mathrm{s}_\alpha(I(x) - I(y))$, with $I(x)$ constant (since x is fixed) and $I(y)$ variable (since y runs over the whole image). The reason for the use of differences in ACE is that they are the easiest operations to jointly implement the differential nature of spatial comparisons and the GW principle recalled in Chapter 2. This can be easily understood considering the toy image with only two pixels x and y. If we define $D_{xy} = I(x) - I(y)$, then $D_{yx} = -D_{xy}$, so their average is 0. The null value can then be mapped to the middle gray with the simple translation using the term $\frac{1}{2}$. The same results can be obtained considering an image of any size and using an odd function of $I(x) - I(y)$, because the average value of an odd function is 0.

We also consider a normalized *weight function* $w : \Omega \times \Omega \to (0, 1)$, $\sum_{y \in \Omega} w(x, y) = 1$ for all $x \in \Omega$, where $w(x, y)$ is a monotonically decreasing function of the Euclidean distance $||x - y||$ representing the induction weight. w can be, for instance, the inverse of $||x - y||$ or a Gaussian kernel with standard deviation left as parameter and so on.

The lightness computation of x is performed by ACE in two steps, the first is called chromatic spatial adjustment and consists of the determination of the following pixel-wise value:

$$R(x) = \sum_{y \in \Omega} w(x, y) \mathrm{s}_\alpha(I(x) - I(y)). \qquad [3.37]$$

Then, with $M = \max_{y \in \Omega}\{R(y)\}$, a dynamic tone reproduction scaling is performed via the equation:

$$L^{\mathrm{ACE}}(x) = \frac{1}{2} + \frac{R(x)}{2M}. \qquad [3.38]$$

Note that, since the odd function s_α is weighted, the sum in [3.37] is not null. The nonlinearity in ACE is determined by the slope function, in fact, in the region $-\frac{1}{\alpha} < I(x) - I(y) < \frac{1}{\alpha}$, i.e. for relatively small intensity differences, s_α increases the contrast, mapping $I(x) - I(y)$ into $\alpha(I(x) - I(y))$ with $\alpha > 1$, while it clips relatively big intensity differences. Finally, the mapping in [3.38] implies a global WP behavior, since there surely exists, at least, one pixel x such that $R(x) = M$ so that its lightness becomes 1. Note that, differently from the ratio-reset Retinex algorithms, ACE can increase and decrease the intensity of a pixel.

3.6. RACE: a model with mixed features between RSR and ACE

Both RSR and ACE decrease the color cast of an image, if it exists. However, while the results of RSR tend to have a nice saturation, those of ACE tend to be somewhat washed out. On the contrary, ACE's nonlinear slope function allows for a noticeable contrast intensification, in particular with large values of the slope parameter α, which cannot be reached with RSR. Moreover, both models fail to work properly in large uniform areas: if these regions are wide enough, RSR detects the region pixels as local maxima, thus it normalizes those pixels on themselves and it produce a great amount of visible noise; on the other side, ACE's chromatic spatial adjustment represented by equation [3.37] will be close to 0 and the pixels will turn gray regardless their original color.

Starting from these considerations, in [PRO 08] the authors developed a fusion of RSR and ACE into an algorithm called "RACE" with the aim of combining the positive features of both algorithms, and they also proposed a technique to avoid the problems mentioned above in case of large uniform areas.

In order to build a combined algorithm between RSR and ACE, we must implement spatially local operations within a common mathematical framework. In [PRO 08], the local sprays of RSR have been favored over the weighted computation performed across the entire image as in ACE due to the fact that they required substantially less computation time.

Once the use of localized spray is established, the main difference between ACE and RSR is the presence of the dynamic tone reproduction scaling in ACE. We recall that this operation introduces a global white-patch behavior in ACE, but, in view of the combination with RSR, this step becomes redundant, since a local white-patch behavior is already provided by RSR.

There is a simple way to remove the dynamic range mapping while keeping the local weighted average behavior typical of ACE: incorporating the term $\frac{1}{2}$ in s_α, i.e. considering this new slope function:

$$\tilde{\mathrm{s}}_\alpha(I(x)-I(y)) \equiv \begin{cases} 0 & \text{if } -1 \le I(x)-I(y) \le -\frac{1}{2\alpha} \\ \frac{1}{2}+\alpha(I(x)-I(y)) & \text{if } -\frac{1}{2\alpha} < I(x)-I(y) < \frac{1}{2\alpha} \\ 1 & \text{if } \frac{1}{2\alpha} \le I(x)-I(y) \le 1. \end{cases} \qquad [3.39]$$

Indicating the lightness corresponding to this spray formulation of the local GW component of ACE with L^{sprayACE}, we have:

$$L^{\text{sprayACE}}(x) = \frac{1}{N}\sum_{k=1}^{N}\frac{1}{\tilde{n}_k}\sum_{y\in S_k(x)\setminus\{x\}}\tilde{\mathrm{s}}_\alpha(I(x)-I(y)) \qquad [3.40]$$

$\tilde{n}_k = \text{card}\{(S_k(x)\setminus\{x\})\cap\Omega\}$ being the number of spray pixels (center x excluded) that lie inside the spatial domain of the image.

Now that the spray formulation of ACE and the new slope function $\tilde{\mathrm{s}}_\alpha$ are defined, RSR and ACE can be combined by performing their local average. This is the most natural operation for the purpose of developing an algorithm with an intermediate behavior between the previous ones.

If we consider a single spray $S_k(x)$, the average contribution of RSR and ACE is given by the formula:

$$L_k^{\text{RACE}}(x) = \frac{1}{2}\left(\frac{I(x)}{I(H_k)}+\frac{1}{\tilde{n}_k}\sum_{j\in S_k(x)\setminus\{i\}}\tilde{\mathrm{s}}_\alpha(I(x)-I(y))\right), \qquad [3.41]$$

as usual, the final lightness is obtained by averaging the N spray contributions:

$$L^{\text{RACE}}(x) = \frac{1}{N}\sum_{k=1}^{N}\frac{1}{2}\left(\frac{I(x)}{I(H_k)} + \frac{1}{\tilde{n}_k}\sum_{y\in S_k(x)\setminus\{x\}} \tilde{s}_\alpha(I(x)-I(y))\right). \qquad [3.42]$$

It is interesting to discuss how formula [3.42] behaves with respect to three ideal conditions. The *ideal white* situation is that in which $I(x) = I(H_k)$ and $\tilde{s}_\alpha(I(x)-I(y)) = 1$ for every $y \in S_k(x) \setminus \{x\}$; the *ideal middle gray* situation happens when $I(x) = \frac{I(H_k)}{2}$ and $\frac{1}{\tilde{n}_k}\sum_{S_k(x)\setminus\{i\}} \tilde{s}_\alpha(I(x)-I(y)) = \frac{1}{2}$; finally, the *ideal black* condition is defined by $I(x) = 0$ and $\tilde{s}_\alpha(I(x)-I(y)) = 0$ for every $y \in S_k(x) \setminus \{x\}$. The correct recovering of white, middle gray and black in the ideal conditions defined above is a basic theoretic test for correct tonal reproduction of RACE. All the ideal situations are easily seen to be correctly verified.

We stress that RACE does not use *ad hoc* pre- or post-processing. The only pre- or post-LUT treatments are due to the conversion respectively from/to gamma encoded sRGB values. Thus, prior to any computation, if the input image was encoded in sRGB, a gamma transformation must be applied to linearize data. In a similar way, prior to visualization, a gamma correction for sRGB encoding should be applied.

3.6.1. *Regularization of RACE formula: attachment to original image*

As mentioned above, the action of RSR and ACE on large homogeneous areas of an image fails to give good results. The combination of the two algorithms in RACE does not remedy the problem. In this subsection, we show how it is possible to modify the RACE formula with a regularization term in order to avoid this unwanted behavior.

Let us fix the attention on the lightness contribution $L_k^{\text{RACE}}(x)$ associated with a spray $S_k(x)$, as defined in [3.41]. The first step in the regularization technique corresponds to modifying $L_k^{\text{RACE}}(x)$ taking a convex linear combination with the original intensity value $I(x)$ of the target pixel:

$$\tilde{L}_k^{\text{RACE}}(x) = \beta_k(x)L_k^{\text{RACE}}(x) + (1-\beta_k(x))I(x). \qquad [3.43]$$

The coefficient $\beta_k(x) \in [0,1]$ is a local parameter that can vary with x. The term $\beta_k(x)L_k^{\text{RACE}}(x)$ in [3.43] is called the "RACE component", while $(1 - \beta_k(x))I(x)$ is called the "original component". For every $x \in \Omega$, we have:

$$\tilde{L}_k^{\text{RACE}}(x) \longrightarrow \begin{cases} I(x) & \text{if } \beta_k(x) \to 0 \\ L_k^{\text{RACE}}(x) & \text{if } \beta_k(x) \to 1 \end{cases} \qquad [3.44]$$

hence, in order to preserve uniform areas from being corrupted by the incorrect behavior of the algorithm, we would like $\beta_k(x)$ to take values close to 0 if $S_k(x)$ samples a uniform image area. Conversely, we would like $\beta_k(x)$ to take values close to 1 if $S_k(x)$ explores very detailed image regions. This task can easily be accomplished by considering, for instance, $\beta_k(x)$ as a monotonically increasing function of the standard deviation $\sigma_k(x)$ associated with $S_k(x)$, i.e.

$$\sigma_k(x) = \sqrt{\sum_{y \in S_k(x)} (I(y) - m_k(x))^2 \, p_{k,x}(I(y))}, \qquad [3.45]$$

where $p_{k,x}(I(y)) = \frac{1}{\tilde{n}_k}\text{card}\{z \in S_k(x),\ I(z) = I(y)\}$ is the occurrence probability of value $I(y)$ inside the spray $S_k(x)$ and

$$m_k(x) = \sum_{y \in S_k(x)} I(y) p_{k,i}(I(y)) \qquad [3.46]$$

is the mean intensity value inside $S_k(x)$. Recalling that sprays are localized around the center x, $\sigma_k(x)$ can be interpreted as a *local measure of average contrast* around x [GON 02].

The local nature of $\sigma_k(x)$ is vital for the declared purposes: spatial locality allows a modulation of RACE component in [3.43] such that it provides a higher contribution in detailed areas than in uniform zones. This is coherent with the characteristics of the HVS, since its efficacy is increased by the presence of local details in a scene [LAN 83, JOB 97a]. Moreover, smooth transitions between uniform and detailed areas correspond to smooth transitions between original and RACE components, avoiding the generation of halos, as confirmed by the tests performed in [PRO 08]. A similar, but simpler, proposal for a local adaptive unsharp masking has been presented in [POL 00].

3.7. An alternative fusion between RSR and ACE: STRESS

A more recent proposal to fuse WP and GW features in a single algorithm is that presented in [KOL 11] and is called STRESS (Spatio-Temporal Retinex-like Envelope with Stochastic Sampling). Like Retinex, STRESS computes, for each pixel, the local white reference, but also the black reference in each chromatic channel. This is done through calculating the maximum and minimum envelope functions, denoted as $E_{\max(x)}$ and $E_{\min(x)}$, respectively.

The computational steps needed to obtain the envelope functions are the following: fix a pixel $x \in \Omega$ and N random sprays [PRO 07] $S_k(x)$, $k = 1, \ldots, N$, centered in x, then compute $M_k = \max_{x \in S_k(x)} I(x)$, $m_k = \min_{x \in S_k(x)} I(x)$ and the following objects:

$$r_k(x) = M_k(x) - m_k(x), \quad v_k(x) = \begin{cases} \frac{1}{2} & \text{if } M_k(x) = m_k(x) \\ \frac{I(x) - m_k(x)}{M_k(x) - m_k(x)} & \text{otherwise,} \end{cases}$$

thus, essentially, the value of $v_k(x)$ is either the middle gray if x lies in a homogeneous area or it is the linearly stretched value of $I(x)$ with respect to the interval $[m_k(x), M_k(x)]$. By denoting $\bar{r}(x)$ and $\bar{v}(x)$ the average values of $r_k(x)$ and $v_k(x)$ over the N sprays, i.e.

$$\bar{r}(x) = \frac{1}{N} \sum_{k=1}^{N} r_k(x), \ \bar{v}(x) = \frac{1}{N} \sum_{k=1}^{N} v_k(x),$$

the authors can finally define the two envelope functions $E_{\min(x)}$ as follows:

$$\begin{aligned} E_{\min}(x) = I(x) - \bar{v}(x)\bar{r}(x), \quad E_{\max}(x) &= I(x) + (1 - \bar{v}(x)\bar{r}(x)) \\ &= E_{\min} + \bar{r}(x). \end{aligned} \qquad [3.47]$$

The final output of STRESS is the stretched value of $I(x)$ on the interval $[E_{\min}, E_{\max}]$, namely:

$$\text{STRESS}(I(x)) = \frac{I(x) - E_{\min}}{E_{\max} - E_{\min}}. \qquad [3.48]$$

STRESS, like RACE, is capable of handling both under and over exposed images, but it is affected by the same noise problems as RSR. In Chapter 5, we will see a variational extension of the technique used to compute the envelope functions based on the total variation. This will allow avoiding the noise problems related to the random spray technique.

4

Variational Formulation of Histogram Equalization

Generally speaking, variational principles amount to defining a suitable functional, i.e. a scalar-valued function defined on a certain functional space, so that its minima (ideally, its *unique* minimum) provide the optimal solution of the problem under analysis. An introduction to variational principles can be found in the Appendix.

In 1997, Caselles and Sapiro used variational principles to give a novel interpretation of histogram equalization of a digital image. This work is not only a profound achievement in itself, but also the main theoretical result on which the next chapter's variational framework of perceptual enhancement of color images is based. For this reason, this entire chapter will be dedicated to the description and interpretation of Caselles–Sapiro's model of histogram equalization.

4.1. The Caselles–Sapiro model

It is worthwhile to start with the notation that will be used from now on. The functional space that we will consider here is that of RGB continuous image functions. To introduce these functions, we will first denote $\Omega \subset \mathbb{R}^2$ as the *spatial domain* of a digital image, $|\Omega|$ as its area, and $x \equiv (x_1, x_2)$ and $y \equiv (y_1, y_2)$ as the coordinates of two arbitrary pixels in Ω. Unless otherwise

Computational Color Science: Variational Retinex-like Methods, First Edition. Edoardo Provenzi.

specified, we will always consider a *normalized dynamic range* in $[0, 1]$, so that an *RGB image function* will be denoted as:

$$\begin{aligned} \vec{I} : \Omega &\longrightarrow [0,1] \times [0,1] \times [0,1] \\ x &\mapsto (I_R(x), I_G(x), I_B(x)) \end{aligned}$$

where each scalar component $I_c(x)$ defines the intensity level of the pixel $x \in \Omega$ in the red, green and blue channels, respectively.

As in the previous chapters, we will perform every computation on the scalar components of the image, thus *treating each chromatic component separately*. Therefore, we will avoid the subscript c and write simply $I(x)$ to denote the intensity of the pixel x in a given chromatic channel.

From the point of view of functional analysis, we will implicitly consider the space of image functions as a subspace of $L^2(\Omega)$, the space of square-integrable (finite-energy) functions from Ω to $[0, 1]$.

Let us also recall very briefly what histogram equalization is. Let $\lambda \in [0, 1]$ be a generic intensity level, then the *histogram* of I computed in λ is given by:

$$h(\lambda) = \frac{1}{|\Omega|} \text{Area}\{x \in \Omega \,|\, I(x) = \lambda\} \qquad \lambda \in [0,1], \tag{4.1}$$

i.e. the *occurrence probability* of the level λ in the image.

The *cumulative histogram* of I computed in λ, $H(\lambda)$, is given by:

$$H(\lambda) = \frac{1}{|\Omega|} \text{Area}\{x \in \Omega \,|\, I(x) \le \lambda\} \qquad \lambda \in [0,1], \tag{4.2}$$

i.e. the *probability of finding a pixel with an intensity less than* λ.

Of course, the relationship between h and H is given by:

$$H(\lambda) = \int_0^{\lambda} h(t)\,dt, \quad H'(\lambda) = h(\lambda), \tag{4.3}$$

i.e. *H is the integral function of h* in the interval $[0, 1]$ and the first derivative of H in each level gives the histogram of that level.

It will be useful for later purposes to note that the relationship $H(\lambda) = \int_0^\lambda h(t)\,dt$ can be rewritten as follows:

$$H(\lambda) = \int_0^\lambda h(t)\,dt = \frac{1}{|\Omega|}\int_0^1 \mathrm{sign}^+(\lambda - I(t))\,dt \qquad [4.4]$$

where

$$\mathrm{sign}^+(s) = \begin{cases} 1 & \text{if } s \geq 0 \\ 0 & \text{if } s < 0 \end{cases}$$

and its *spatial version*

$$H(I(x)) = \frac{1}{|\Omega|}\int_\Omega \mathrm{sign}^+(I(x) - I(y))\,dy. \qquad [4.5]$$

An image is said to be *equalized* if *each level has the same occurrence probability*, i.e. if $h(\lambda) \equiv 1$ (recall that the histogram is normalized) $\forall\lambda$, which, of course, can be translated to the following condition on the cumulative histogram: $H(\lambda) = \lambda$, $\forall\lambda$.

It is easy to prove (see, e.g., [GON 02]) that the transformation from $[0, 1]$ to itself given by $\lambda \longmapsto H(\lambda)$ is the easiest application that implements histogram equalization.

However, this is not the only histogram equalization transformation available in the literature. In particular, a variational interpretation has been provided by Caselles and Sapiro in [SAP 97]. For the purposes of this book, the Caselles–Sapiro's results can be resumed in the following theorem.

THEOREM 4.1.– Given the functional

$$E_{\text{hist eq}}(I) \equiv 2\int_\Omega \left(I(x) - \frac{1}{2}\right)^2 dx - \frac{1}{|\Omega|}\iint_{\Omega^2} |I(x) - I(y)|\,dxdy \qquad [4.6]$$

if $I^* = \mathrm{argmin}_I\, E_{\text{hist eq}}(I)$, then I^* has equalized histogram, i.e. $H(I^*(x)) = I^*(x)$ for all $x \in \Omega$.

Moreover, if I_0 is the original image, then the initial value problem for the gradient descent

$$\begin{cases} \partial_t I = -\delta E_{\text{hist eq}}(I) \\ I(0) = I_0 \end{cases}$$

has only one solution, where t is the evolution parameter of the iterative gradient descent scheme and the symbol δ represents the first variation of the functional.

$E_{\text{hist eq}}(I)$ will be called the *Caselles–Sapiro functional* from now on. The entire proof of the theorem can be found in [SAP 97]. While the details of the proof about the convergence to the minimum and the uniqueness are too long and technical to be reproduced here, it is worthwhile showing that an image function that satisfies the Euler-Lagrange equations associated with $E_{\text{hist eq}}(I)$ is equalized, because the tricks used in the proof show explicitly the link with histogram equalization, which is far from being intuitive at a first glance by looking at $E_{\text{hist eq}}(I)$.

First, let us start by recalling a classical lemma of variational calculus.

LEMMA 4.1.– Given the two functionals

$$E_1(I) = \int_\Omega \psi(I(x))\, dx, \quad E_2(I) = \iint_{\Omega^2} \phi(I(x), I(y))\, dxdy, \tag{4.7}$$

where ψ is a differentiable function defined on the codomain of I and ϕ is a differentiable function defined on the 2-th Cartesian power of the codomain of I, then their first variations are, respectively:

$$\delta E_1(I, J) = \int_\Omega \left.\frac{\partial \psi}{\partial I}\right|_{I(x)} J(x)\, dx \equiv \int_\Omega \psi'(I(x))\, J(x)\, dx \tag{4.8}$$

and

$$\delta E_2(I, J) = \iint_{\Omega^2} \left(\left.\frac{\partial \phi}{\partial I}\right|_{I(x)} J(x) + \left.\frac{\partial \phi}{\partial I}\right|_{I(y)} J(y) \right) dxdy, \tag{4.9}$$

with J being a perturbation of I.

Then, by linearity, we can compute the first variation of the two terms appearing in $E_{\text{hist eq}}(I)$ and then add the results. Therefore, we can write:

$$D_{\frac{1}{2}}(I) = 2\int_\Omega \left(I(x) - \frac{1}{2}\right)^2 dx; \qquad [4.10]$$

$$C(I) = \frac{1}{|\Omega|}\iint_{\Omega^2} |I(x) - I(y)|\, dxdy. \qquad [4.11]$$

By virtue of formula [4.8], we have:

$$\delta D_{\frac{1}{2}}(I, J) = \int_\Omega 4\left(I(x) - \frac{1}{2}\right) J(x)\, dx, \qquad [4.12]$$

and thanks to formula [4.9], we have:

$$\begin{aligned}\delta C(I, J) &= \frac{1}{|\Omega|}\iint_{\Omega^2} [\mathrm{sign}(I(x) - I(y))J(x) \\ &\quad -\mathrm{sign}(I(x) - I(y))J(y)]\ dxdy \\ &= \frac{1}{|\Omega|}\left\{\iint_{\Omega^2} \mathrm{sign}(I(x) - I(y))J(x)\, dxdy \right. \\ &\quad \left. - \iint_{\Omega^2} \mathrm{sign}(I(x) - I(y))J(y)\, dxdy\right\}. \end{aligned} \qquad [4.13]$$

Now, interchanging the role of the "mute" variables x and y in the second integral of the last step, we have:

$$\begin{aligned}&\frac{1}{|\Omega|}\iint_{\Omega^2} \mathrm{sign}(I(x) - I(y))J(y)\, dxdy \\ &\quad = \frac{1}{|\Omega|}\iint_{\Omega^2} \mathrm{sign}(I(y) - I(x))J(x)\, dydx \end{aligned} \qquad [4.14]$$

but using the oddness of the sign function, we have:

$$\begin{aligned}&\frac{1}{|\Omega|}\iint_{\Omega^2} \mathrm{sign}(I(x) - I(y))J(y)\, dxdy \\ &\quad = -\frac{1}{|\Omega|}\iint_{\Omega^2} \mathrm{sign}(I(x) - I(y))J(x)\, dydx. \end{aligned} \qquad [4.15]$$

Hence, we can write:

$$\begin{aligned}\delta C(I,J) &= \frac{1}{|\Omega|}\left\{\iint_{\Omega^2} \operatorname{sign}(I(x)-I(y))J(x)\,dydx\right.\\ &\quad\left.+\iint_{\Omega^2} \operatorname{sign}(I(x)-I(y))J(x)\,dydx\right\}\\ &= \frac{2}{|\Omega|}\iint_{\Omega^2} \operatorname{sign}(I(x)-I(y))J(x)\,dydx \end{aligned} \qquad [4.16]$$

which can be conveniently rearranged as follows:

$$\delta C(I,J) = \int_\Omega \left(\frac{2}{|\Omega|}\int_\Omega \operatorname{sign}(I(x)-I(y))\,dy\right) J(x)\,dx. \qquad [4.17]$$

Since $\delta E_{\text{hist eq}}(I,J) = \delta D_{\frac{1}{2}}(I,J) - \delta C(I,J)$, by using formulas [4.12] and [4.17], we have:

$$\begin{aligned}\delta E_{\text{hist eq}}(I,J) &= \int_\Omega 4\left(I(x)-\frac{1}{2}\right)J(x)\,dx\\ &\quad - \int_\Omega \left(\frac{2}{|\Omega|}\int_\Omega \operatorname{sign}(I(x)-I(y))\,dy\right) J(x)\,dx \end{aligned} \qquad [4.18]$$

i.e.

$$\begin{aligned}\delta E_{\text{hist eq}}(I,J) &= \int_\Omega \left[4\left(I(x)-\frac{1}{2}\right)\right.\\ &\quad\left. - \frac{2}{|\Omega|}\int_\Omega \operatorname{sign}(I(x)-I(y))\,dy\right] J(x)\,dx. \end{aligned} \qquad [4.19]$$

The stationary condition $\delta E_{\text{hist eq}}(I,J) = 0$, $\forall J$ implies that the expression in the square bracket must be zero, i.e.

$$\begin{aligned}\delta E_{\text{hist eq}}(I,J) = 0 \quad \Longleftrightarrow \quad & 4\left(I(x)-\frac{1}{2}\right)\\ & - \frac{2}{|\Omega|}\int_\Omega \operatorname{sign}(I(x)-I(y))\,dy = 0, \end{aligned} \qquad [4.20]$$

so that the Euler-Lagrange equation relative to the energy functional $E_{\text{hist eq}}$ is the following implicit equation

$$2\left(I(x) - \frac{1}{2}\right) - \frac{1}{|\Omega|}\int_\Omega \operatorname{sign}(I(x) - I(y))\,dy = 0, \qquad [4.21]$$

which can be suitably rewritten as

$$\frac{1}{|\Omega|}\int_\Omega \operatorname{sign}(I(x) - I(y))\,dy = 2I(x) - 1. \qquad [4.22]$$

Now, using the identity $\operatorname{sign}(t) \equiv 2\operatorname{sign}^+(t) - 1 \ \forall t \in \mathbb{R}$, we can express the left-hand side of the Euler-Lagrange equation as:

$$\begin{aligned}
&\frac{1}{|\Omega|}\int_\Omega (2\operatorname{sign}^+(I(x) - I(y)) - 1)\,dy \\
&\quad = \frac{2}{|\Omega|}\int_\Omega \operatorname{sign}^+(I(x) - I(y))\,dy - \frac{\int_\Omega dy}{|\Omega|} \\
&\quad = 2H(I(x)) - 1, \qquad [4.23]
\end{aligned}$$

where we have used the fact that $\frac{1}{|\Omega|}\int_\Omega \operatorname{sign}^+(I(x) - I(y))\,dy$ is the spatial version of the cumulative histogram $H(I(x))$, as noted in equation [4.5].

Thus, the Euler-Lagrange equation [4.22] is equivalent to $2H(I(x)) - 1 = 2I(x) - 1$, i.e. to $H(I(x)) = I(x)$, but then

$$\delta E_{\text{hist eq}}(I, J) = 0 \quad \Longleftrightarrow \quad H(I(x)) = I(x), \ \forall x \in \Omega, \qquad [4.24]$$

which means that the image function I that satisfies the Euler-Lagrange equations of the functional $E_{\text{hist eq}}(I)$ has an equalized histogram, as it had to be proven.

4.2. Interpretation of Caselles–Sapiro’s functional for histogram equalization

Interpretation of the energy functional $E_{\text{hist eq}}(I)$ in terms of image features is crucial for the following chapter. As stated previously, we can write $E_{\text{hist eq}}(I) = D_{\frac{1}{2}}(I) - C(I)$. Thus, the minimization of $E_{\text{hist eq}}(I) = D_{\frac{1}{2}}(I) - C(I)$ is achieved through the *minimization of* $D(I)$ and the *maximization of* $C(I)$.

The meaning of the two functional terms is as follows:

– $D_{\frac{1}{2}}(I)$ is called *global quadratic dispersion* around the middle gray level $\frac{1}{2}$, which is minimized when $I(x) \equiv \frac{1}{2}$ for all $x \in \Omega$; that is, the minimization of this term tends to turn I into an uniform gray image;

– $C(I)$ is called *global contrast* whose maximization corresponds to the maximization of the global contrast of the image I, expressed by the set of absolute differences $|I(x) - I(y)|$.

Thus, the argmin of the Caselles–Sapiro functional is the image corresponding to the optimal balance between *two opposite effects*: on the one side, the minimization of $D_{\frac{1}{2}}(I)$ tends to *set all the levels to the average gray level* $\frac{1}{2}$ but, on the other side, the minimization of $-C(I)$ tends to *spread the intensity levels apart, as far as possible from each other*. So, the intrinsic meaning of Theorem 4.1 is that *the equilibrium among two conflicting actions, dispersion control around the middle gray and global contrast enhancement, induces histogram equalization.*

One practical consequence of this result is that by applying, for example, the gradient descent technique to minimize $E_{\text{hist eq}}(I)$, we can stop the minimization process before reaching the complete equalization, thus realizing a *partial equalization* that can nonetheless be useful to avoid the typical over-enhancement of low-key images (for more details, see [GON 02]).

However, for the purposes of color image processing, the most important consequences of Theorem 4.1 are theoretical: in fact, as we will see in the next chapter, we can modify the functional $E_{\text{hist eq}}(I)$ in such a way that the basic balance principle of histogram equalization is preserved, but we can change the analytical form of the terms $D_{\frac{1}{2}}(I)$ and $C(I)$ by taking inspiration from human visual perceptual features. The argmin image I^* of the modified functional is a color-corrected version of the original image driven by the perceptual properties of the human visual system (HVS).

4.3. Application of histogram equalization techniques to color images

The application of histogram equalization to color images is far from trivial. If we apply it on the three chromatic channels independently, then the resulting image is likely to show unnatural colors. However, if we apply it to the achromatic channel and keep chromaticity intact, the resulting image can show a weak enhancement. Figure 4.1 clearly shows the aforementioned features.

In the next chapter, we will see that if the histogram equalization functional is suitably modified by introducing some important features of the HVS, then we can perform a separate channel enhancement that gives sound results, even if a certain color shift (that can be treated with *ad hoc* techniques) appears.

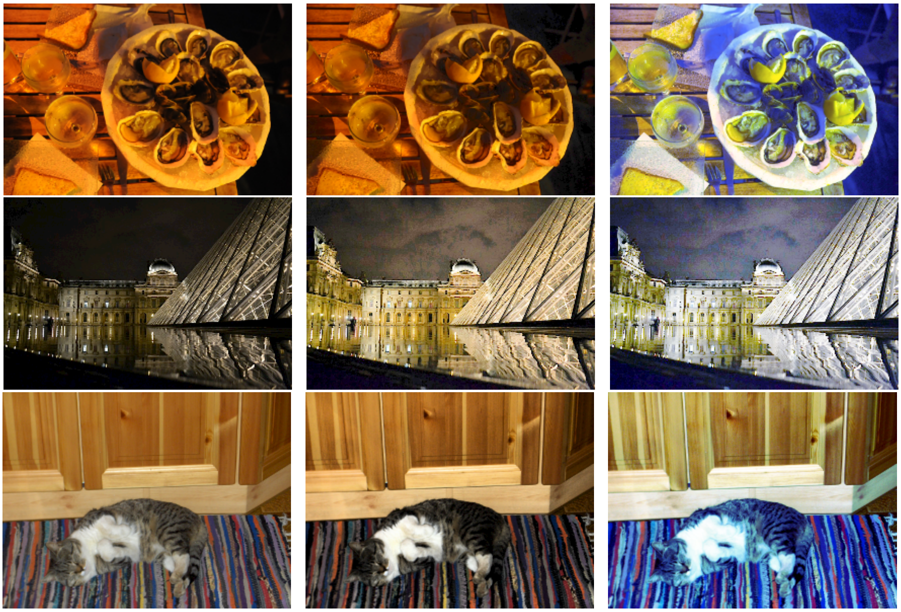

Figure 4.1. *Left column: original color images. Middle column: histogram equalization of the luminance. Note that the color cast of the picture of the first row is not filtered out by the histogram equalization on the luminance channel. Right column: histogram equalization of the three independent chromatic channels. Note the dramatic color shifts. For a color version of the figure, see www.iste.co.uk/provenzi/color.zip*

5

Perceptually-inspired Variational Models for Color Enhancement in the RGB Space

Now that the basic properties of the human visual system (HVS) and the variational interpretation of histogram equalization have been introduced, it is possible to describe the variational framework for perceptually inspired color image enhancement, proposed in [PAL 09], and its consequences.

Before turning to the mathematical details, it is worth explaining the main similarities and differences between histogram equalization and HVS properties that led the authors of [PAL 09] to the formulation of this model.

Let us start with similarities. First, after the light intensity reduction performed by the eye elements, the visual signal is transduced by photoreceptors to an electrical signal centered around the semi-saturation level. This can be thought as the HVS process equivalent to the adjustment around the average gray level $\frac{1}{2}$ in histogram equalization.

Second, the local contrast enhancement performed by the HVS opposes the shrinking of a light dynamic range, analogously to what happens in histogram equalization.

Regarding differences, the most important one is that the HVS handles contrast locally, i.e. in a spatially dependent way. Furthermore, color constancy and Weber-Fechner's law are not taken into account in histogram equalization.

Computational Color Science: Variational Retinex-like Methods, First Edition. Edoardo Provenzi.

Therefore, the aim of [PAL 09], and its related papers [BER 07, BER 09, PRO 14], was to modify the Caselles–Sapiro functional in order to make the new energy consistent with the HVS properties recalled previously. It will be seen that even working in the RGB space, the output images of the modified functional are qualitatively much better than those of histogram equalization.

Of course, in the literature, we can find several other proposals to modify histogram equalization which have comparable or even more efficient color correction properties than those presented here. The aim of the work [PAL 09], and its related papers, were primarily theoretical, i.e. the authors wanted to test to what extent we can solely rely on a model of the HVS, and not on *ad hoc* mathematical and/or algorithmic requirements, to avoid, or at least, strongly diminish the problems related to RGB histogram equalization (and, in general, separate waveband processing, as in multi-spectral imaging).

As it will be seen later, the framework that they have built is general enough to be adopted also for other applications.

5.1. Beyond the Caselles–Sapiro model: modification of the histogram equalization functional to approach visual properties

The main problem in the modification of the Caselles–Sapiro functional is the determination of a contrast enhancement term that complies with the HVS features. Once it is determined, the selection of the adjustment term can be carried out through dimensional coherence, as it will be explained in more detail in this section.

5.1.1. *A contrast term coherent with HVS properties*

Let us consider the problem of building a suitable contrast measure $\bar{c}(a, b)$ between two gray levels $a, b > 0$ (to avoid some singular cases, we shall assume that intensity image values are always positive). We require the contrast function $\bar{c} : (0, +\infty) \times (0, +\infty) \to \mathbb{R}$ to be continuous, symmetric in (a, b), i.e. $\bar{c}(a, b) = \bar{c}(b, a)$, increasing when $\min(a, b)$ decreases or $\max(a, b)$ increases.

Basic examples of contrast measures are given by $\bar{c} = |a - b| \equiv \max(a, b) - \min(a, b)$ or $\bar{c}(a, b) = \max(a, b)/\min(a, b)$.

Since our purpose is to enhance contrast by *minimizing* an energy, we define an *inverse contrast function* $c(a,b)$, still continuous and symmetric in (a,b), but decreasing when $\min(a,b)$ decreases or $\max(a,b)$ increases. Note that if $\bar{c}(a,b)$ is a contrast measure, then $c(a,b) = -\bar{c}(a,b)$ or $c(a,b) = 1/\bar{c}(a,b)$ is an inverse contrast measure, so that basic examples of inverse contrast measures are given by $c(a,b) = \min(a,b) - \max(a,b)$ or $c(a,b) = \frac{\min(a,b)}{\max(a,b)}$.

Let us now introduce a weighting function to localize the contrast computation. Let $w : \Omega \times \Omega \to \mathbb{R}^+$ be a positive symmetric kernel, such that $w(x,y) = w(y,x) > 0$, for all $x, y \in \Omega$, which measures the mutual influence between the pixels x, y. The symmetry requirement is motivated by the fact that the mutual chromatic induction is independent of the order of the two pixel considered. Usually, we assume that $w(x,y)$ is a function of the Euclidean distance $\|x - y\|$ between the two points. We shall assume that *the kernel is normalized*, i.e.

$$\int_{\Omega} w(x,y) = 1 \qquad \forall x \in \Omega. \tag{5.1}$$

Given an inverse contrast function $c(a,b)$ and a positive symmetric kernel $w(x,y)$, we define a contrast energy term by:

$$C_w(I) = \iint_{\Omega^2} w(x,y)\, c(I(x), I(y))\, dxdy. \tag{5.2}$$

Thanks to the symmetry assumption, we may write $c(a,b) = \tilde{c}(\min(a,b), \max(a,b))$ for some function $\tilde{c}$ (indeed, well defined by this identity). Note that $\tilde{c}$ is non-decreasing in the first argument and non-increasing in the second one. The symmetry hypothesis is not restrictive; in fact, if the inverse contrast measure $c(a,b)$ is not symmetric, we can write it as the sum $c(a,b) = c_s(a,b) + c_{as}(a,b)$, where $c_s(a,b)$ and $c_{as}(a,b)$ are symmetric and anti-symmetric, respectively. Since the sum $\iint_{\Omega^2} w(x,y)\, c_{as}(I(x), I(y))\, dxdy = 0$, then the only remaining term is $\iint_{\Omega^2} w(x,y)\, c_s(I(x), I(y))\, dxdy$; hence, we may assume that $c(a,b)$ is symmetric in (a,b).

In order to find out which properties the contrast term should satisfy, let us note that, thanks to color constancy, an overall change in illumination, measured by the generic quantity $\lambda > 0$, does not affect the visual sensation.

This requires the contrast function c to be homogeneous, recalling that c is homogeneous of degree $n \in \mathbb{Z}$ if

$$c(\lambda a, \lambda b) = \lambda^n \, c(a, b) \quad \forall \lambda, a, b \in (0, +\infty), \qquad [5.3]$$

where a and b are synthetic representations of $I(x)$ and $I(y)$.

Of course, if $n = 0$, c automatically disregards the presence of λ, but we can say more: since λ can take any positive value, if we set $\lambda = 1/b$, we may write equation [5.3] as:

$$c(a, b) = b^n \, c\left(\frac{a}{b}, 1\right) \quad \forall a, b \in (0, +\infty), \qquad [5.4]$$

so when $n = 0$, $b^n = 1$ and c results as a function of the ratio a/b that intrinsically disregards the overall changes in light intensity. If $n > 0$, then λ has a global influence and could be removed by performing a suitable normalization (for instance, dividing by the n-th power of the highest intensity level).

We summarize these observations by saying that we assume that the inverse contrast function $c(a, b)$ is homogeneous.

Thanks to the arguments presented so far, we have that inverse contrast functions that are homogeneous of degree $n = 0$ are those that can be written as a monotone non-decreasing function of $\min(I(x), I(y))/\max(I(x), I(y))$.

Finally, let us consider Weber-Fechner's law: if the intensity of the uniform background in Weber's experiment is I_0 and the supra-threshold stimulus is I_1, then we can rewrite the Weber ratio $\frac{I_1 - I_0}{I_0}$ as $I_1/I_0 - 1$, i.e. the sensation of intensity contrast is a function of I_1/I_0.

This reason motivates us to say that $c(a, b)$ is a *generalized Weber-Fechner contrast function* if c is an *inverse contrast* function that can be written as a non-decreasing function of $\min(a, b)/\max(a, b)$.

Even if Weber-Fechner's law is not valid for all intensity levels, it remains correct for a large dynamic range; thus, it seems natural to require c to be a generalized Weber-Fechner contrast function.

Explicit examples of energy functionals complying with our set of assumptions on the contrast function are given by:

$$C_w^{\mathrm{id}}(I) := \frac{1}{4} \iint_{\Omega^2} w(x,y) \, \frac{\min(I(x), I(y))}{\max(I(x), I(y))} \, dxdy \qquad [5.5]$$

$$C_w^{\log}(I) := \frac{1}{4} \iint_{\Omega^2} w(x,y) \, \log\left(\frac{\min(I(x), I(y))}{\max(I(x), I(y))}\right) dxdy \qquad [5.6]$$

$$C_w^{-\mathcal{M}}(I) := -\frac{1}{4} \iint_{\Omega^2} w(x,y) \, \mathcal{M}\left(\frac{\min(I(x), I(y))}{\max(I(x), I(y))}\right) dxdy \qquad [5.7]$$

where

$$\mathcal{M}\left(\frac{\min(I(x), I(y))}{\max(I(x), I(y))}\right) := \frac{1 - \frac{\min(I(x),I(y))}{\max(I(x),I(y))}}{1 + \frac{\min(I(x),I(y))}{\max(I(x),I(y))}} \equiv \frac{|I(x) - I(y)|}{I(x) + I(y)}, \qquad [5.8]$$

is the well-known Michelson's definition of contrast [MIC 27].

The upper symbol in the above definitions of C_w simply specifies the monotone function applied on the basic contrast variable $t := \frac{\min(I(x),I(y))}{\max(I(x),I(y))}$, i.e. identity $\mathrm{id}(t) = t$, logarithm $\log t$ and minus the Michelson's contrast function $-\mathcal{M}(t) = -\frac{1-t}{1+t}$, respectively.

Note that the function $t = \min(I(x), I(y))/\max(I(x), I(y))$ is minimized when the minimum takes the smallest possible value and the maximum takes the largest possible one, which corresponds to a contrast stretching. Thus, minimizing an increasing function of the variable t will produce a contrast enhancement. To refer to any one of them, we use the notation $C_w^{\varphi}(I)$, where $\varphi = \mathrm{id}, \log, -\mathcal{M}$.

5.1.2. *Entropic adjustment term*

Let us now consider the term that should control the dispersion. As suggested previously, we intend it as an adjustment term to the initial given image I_0 (not to depart too much from the original image) and to the average illumination value, represented by the quantity μ. Thus, we define two dispersion functions: $d_1(I(x), I_0(x))$, which measures the separation between

$I(x)$ and $I_0(x)$, and $d_2(I(x), \mu)$, which measures the separation from the value μ.

Both d_1 and d_2 are continuous functions $d_{1,2} : \mathbb{R}^2 \to \mathbb{R}^+$, such that $d_{1,2}(a, a) = 0$ for any $a \in \mathbb{R}$ and $d_{1,2}(a, b) > 0$ if $a \neq b$.

We write $d_{I_0,\mu}(I(x)) = d_1(I(x), I_0(x)) + d_2(I(x), \mu)$, and the dispersion energy term as:

$$D(I) = \int_\Omega d_{I_0,\mu}(I(x))\, dx. \qquad [5.9]$$

In principle, to measure the dispersion of I with respect to I_0 or $1/2$, any distance function can be used. The simplest example would be a quadratic distance:

$$D^q_{\alpha,\beta}(I) := \frac{\alpha}{2} \int_\Omega \left(I(x) - \frac{1}{2} \right)^2 dx + \frac{\beta}{2} \int_\Omega (I(x) - I_0(x))^2\, dx, \quad \alpha,\beta > 0. \qquad [5.10]$$

However, given that contrast terms are expressed as homogeneous functions of degree 0, the variational derivatives are homogeneous functions of degree -1. We search for functions that are able to maintain dimensional coherence with the contrast term.

A good candidate for this is the *entropic dispersion* term [AMB 05], i.e.

$$\begin{aligned} D_{\alpha,\beta}(I) := \alpha & \int_\Omega \left(\mu \log \frac{\mu}{I(x)} - (\mu - I(x)) \right) dx \\ & + \beta \int_\Omega \left(I_0(x) \log \frac{I_0(x)}{I(x)} - (I_0(x) - I(x)) \right) dx, \end{aligned} \qquad [5.11]$$

where $\alpha,\beta > 0$, which is based on the relative entropy distance [AMB 05] between I and μ (the first term) and between I_0 and I (the second term).

Note that if $a > 0$ and $f(s) = a \log \frac{a}{s} - (a - s)$, $s \in (0, 1]$, then $\frac{df}{ds}(s) = 1 - \frac{a}{s}$ and $\frac{d^2 f}{ds^2}(s) = \frac{a}{s^2} > 0$, $\forall s$. So, $f(s)$ has a global minimum in $s = a$. In particular, this holds when $a = I_0(x)$ or $a = \mu$. Given the statistical interpretation of entropy, we can say that *minimizing $D_{\alpha,\beta}(I)$ amounts to minimizing the disorder of intensity levels around μ and around the original* *data* $I_0(x)$. Thus, $D_{\alpha,\beta}(I)$ accomplishes the required tasks of an adjustment term.

The minimization of $E^{\varphi}_{w,\alpha,\beta,\mu}(I) = C^{\varphi}_{w}(I) + D_{\alpha,\beta,\mu}$ corresponds to a trade-off between two opponent mechanisms: on the one hand, we have entropic control of dispersion around μ and around the original data, and on the other hand, we have local contrast enhancement invariant with respect to global illumination changes. These energies are called perceptually inspired or perceptual functionals.

In the following section, we show the explicit minimization of perceptual functionals.

5.2. Minimization of perceptual functionals

The existence of a minimum in the discrete framework can be guaranteed for a quite general class of energy functionals. Let us define, for $\rho > 0$, $\mathcal{F}_\rho := \{I : \Omega \to [0,1],\ I(x) \geq \rho\ \forall x \in \Omega\}$. We minimize the energy E in the class $\mathcal{F}_\rho$ to avoid singularities in the entropic dispersion term or when we use $\varphi = \log$.

In [PAL 09], the following result has been proved.

THEOREM 5.1.– Let $c : (0,1] \times (0,1] \to \mathbb{R}$ be a continuous function. Let $E^{\varphi}_{w,\alpha,\beta,\mu}(I) := D_{\alpha,\beta,\mu}(I) + C^{\varphi}_{w}(I)$, where $C^{\varphi}_{w}(I)$ is given in [5.2]. There is a minimum of $E^{\varphi}_{w,\alpha,\beta,\mu}(I)$ in the class of functions $\mathcal{F}_\rho$. An analogous result holds if we use the quadratic dispersion term $D^{q}_{\alpha,\beta,\mu}(I)$.

Note that if the energy E is differentiable, its argmin I^* satisfies $\delta E^{\varphi}_{w,\alpha,\beta,\mu}(I^*) = 0$. Before computing the Euler-Lagrange equations, we note that the contrast terms $C^{\varphi}_{w}(I)$, $\varphi = \mathrm{id}, \log, -\mathcal{M}$ are not convex and the basic function $t := \frac{\min(a,b)}{\max(a,b)}$ is not differentiable.

In fact, we may write $\min(a,b) = \frac{1}{2}(a + b - |a - b|)$ and $\max(a,b) = \frac{1}{2}(a + b + |a - b|)$, for any $a, b \in \mathbb{R}$. The non-differentiability comes from the absolute value $A(z) = |z|$, $z \in \mathbb{R}$.

To use a gradient descent approach for the minimization, we must regularize the basic variable t. We note that $A'(z) = 1$ if $z > 0$, $A'(z) = -1$ if

$z < 0$ and A is not differentiable at $z = 0$. However, all the values $s \in [-1, 1]$ are *subtangents* of $A(z)$ at $z = 0$, i.e. $A(z) - A(0) \geq s(z - 0)$ for any $z \in \mathbb{R}$.

Thus, we may write $A'(z) = \operatorname{sign}(z)$, where:

$$\operatorname{sign}(z) = \begin{cases} 1 & \text{if } z > 0 \\ [-1, 1] & \text{if } z = 0 \\ -1 & \text{if } z < 0 \end{cases} . \qquad [5.12]$$

We define $\operatorname{sign}_0(z)$ as in [5.12], but with the particular choice 0 when $z = 0$.

It is useful to introduce the following definition. Given $\varepsilon > 0$, we say that $A_\varepsilon(z)$ is a "*nice regularization*" of $A(z)$ if $A_\varepsilon(z) \geq 0$ is convex, differentiable with continuous derivative, $A_\varepsilon(0) = 0$, $A_\varepsilon(-z) = A_\varepsilon(z)$, and

i) $A_\varepsilon(z) \leq |z|$ for any $z \in \mathbb{R}$ and $A_\varepsilon(z) = |z| + Q_{1,\varepsilon}(z)$, where $Q_{1,\varepsilon}(z) \to 0$ as $\varepsilon \to 0$, uniformly in $z \in [-1, 1]$;

ii) Let us denote $s_\varepsilon(z) = A'_\varepsilon(z)$. Then, $|s_\varepsilon(z)| \leq 1$ for any $z \in [-1, 1]$, $s_\varepsilon(z) \to \operatorname{sign}_0(z)$ as $\varepsilon \to 0$ for any $z \in \mathbb{R}$, and $Q_{2,\varepsilon}(z) := A_\varepsilon(z) - z s_\varepsilon(z) \to 0$ as $\varepsilon \to 0$, uniformly in $z \in [-1, 1]$.

A nice regularization of $A(z)$ actually exists:

– *Example* 1): $A_\varepsilon(z) = \sqrt{\varepsilon^2 + |z|^2} - \varepsilon$; in this case, $s_\varepsilon(z) = \frac{z}{\sqrt{\varepsilon^2+|z|^2}}$, $Q_{1,\varepsilon}(z) = O(\varepsilon)$ and $Q_{2,\varepsilon}(z) := A_\varepsilon(z) - z s_\varepsilon(z) = O(\varepsilon)$;

– *Example* 2): $A_\varepsilon(z) = z\frac{\arctan(z/\varepsilon)}{\arctan(1/\varepsilon)} - \frac{\varepsilon}{2\arctan(1/\varepsilon)}\log(1 + \frac{z^2}{\varepsilon^2})$, in this case $s_\varepsilon(z) = \frac{\arctan(z/\varepsilon)}{\arctan(1/\varepsilon)}$, $Q_{1,\varepsilon}(z) = O(\varepsilon \log(1/\varepsilon))$ and $Q_{2,\varepsilon}(z) = O(\varepsilon \log(1/\varepsilon))$, uniformly in $z \in [-1, 1]$.

$O(F(\varepsilon))$ is any expression that satisfies $|O(F(\varepsilon))| \leq CF(\varepsilon)$ for some constant $C > 0$ and $\varepsilon > 0$ small enough. In both cases, $s_\varepsilon(z) \to \operatorname{sign}_0(z)$ as $\varepsilon \to 0$ for any $z \in \mathbb{R}$ (see [PAL 09]).

Let us now assume that $A_\varepsilon(z)$ is a nice regularization of $A(z)$. We set:

$$\min_\varepsilon(a, b) = \frac{1}{2}(a + b - A_\varepsilon(a - b)), \qquad \max_\varepsilon(a, b) = \frac{1}{2}(a + b + A_\varepsilon(a - b)). \quad [5.13]$$

We define the regularized version of the perceptual functionals as follows:

$$C^{\mathrm{id}}_{w,\varepsilon}(I) := \frac{1}{4}\iint_{\Omega^2} w(x,y)\,\frac{\min_\varepsilon(I(x),I(y))}{\max_\varepsilon(I(x),I(y))}\,dxdy; \qquad [5.14]$$

$$C^{\log}_{w,\varepsilon}(I) := \frac{1}{4}\iint_{\Omega^2} w(x,y)\,\log\left(\frac{\min_\varepsilon(I(x),I(y))}{\max_\varepsilon(I(x),I(y))}\right)dxdy; \qquad [5.15]$$

$$C^{-\mathcal{M}}_{w,\varepsilon}(I) := -\frac{1}{4}\iint_{\Omega^2} w(x,y)\,\frac{A_\varepsilon(I(x)-I(y))}{I(x)+I(y)}\,dxdy. \qquad [5.16]$$

In [PAL 09], the following result has been proved.

THEOREM 5.2.– Assume that $A_\varepsilon(z)$ is a nice regularization of $A(z)$.

i) The first variation of $C^{\mathrm{id}}_{w,\varepsilon}(I)$ is:

$$\begin{aligned}\delta C^{\mathrm{id}}_{w,\varepsilon}(I) &= -\tfrac{1}{2}\int_\Omega w(x,y)\tfrac{I(y)}{\max_\varepsilon(I(x),I(y))^2}s_\varepsilon(I(x)-I(y))\,dy + S_\varepsilon\\ &= -\tfrac{1}{2}\int_\Omega w(x,y)\tfrac{I(y)}{\max(I(x),I(y))^2}s_\varepsilon(I(x)-I(y))\,dy + S'_\varepsilon,\end{aligned} \qquad [5.17]$$

where $S_\varepsilon, S'_\varepsilon = O(Q_{1,\varepsilon}(I(x)-I(y)) + Q_{2,\varepsilon}(I(x)-I(y)))$. Note that in the first formula, we have max and in the second one, we have $\max_\varepsilon$;

ii) The first variation of $C^{\log}_{w,\varepsilon}(I)$ is:

$$\delta C^{\log}_{w,\varepsilon}(I) = -\frac{1}{2}\int_\Omega w(x,y)\frac{1}{I(x)}s_\varepsilon(I(x)-I(y))\,dy + S_\varepsilon, \qquad [5.18]$$

where $S_\varepsilon = O(Q_{1,\varepsilon}(I(x)-I(y)) + Q_{2,\varepsilon}(I(x)-I(y)))$;

iii) The first variation of $C^{-\mathcal{M}}_{w,\varepsilon}(I)$ is:

$$\delta C^{-\mathcal{M}}_{w,\varepsilon}(I) = -\int_\Omega w(x,y)\frac{I(y)}{(I(x)+I(y))^2}s_\varepsilon(I(x)-I(y))\,dy + S_\varepsilon, \qquad [5.19]$$

where $S_\varepsilon = O(Q_{2,\varepsilon}(I(x)-I(y)))$.

In all cases, $Q_{1,\varepsilon}(z), Q_{2,\varepsilon}(z) \to 0$ as $\varepsilon \to 0$, uniformly in $z \in [-1,1]$.

Thus, we know that $S_\varepsilon = O(\varepsilon)$ if $A_\varepsilon(z)$ is given by Example 1), and $S_\varepsilon = O(\varepsilon \log 1/\varepsilon)$ if $A_\varepsilon(z)$ is given by Example 2). These were the cases of interest in [PAL 09] for the experiments.

Note that letting $\varepsilon \to 0$, we have that $\delta C^{\varphi}_{w,\varepsilon}(I) \to \delta C^{\varphi}_{w,0}(I)$, where:

$$\begin{aligned}
\delta C^{\mathrm{id}}_{w,0}(I) &= -\frac{1}{2}\int_{\Omega} w(x,y)\frac{I(y)}{\max(I(x),I(y))^2}\,\mathrm{sign}_0(I(x)-I(y))\,dy \\
&= -\frac{1}{2}\left(\int_{\{y\in\Omega\,:\,I(x)>I(y)\}} w(x,y)\frac{I(y)}{I(x)^2} - \int_{\{y\in\Omega\,:\,I(x)<I(y)\}} w(x,y)\frac{1}{I(y)}\right); \\
\delta C^{\log}_{w,0}(I) &= -\frac{1}{2}\int_{\Omega} w(x,y)\frac{1}{I(x)}\,\mathrm{sign}_0(I(x)-I(y))\,dy \\
&= -\frac{1}{2}\left(\int_{\{y\in\Omega\,:\,I(x)>I(y)\}} w(x,y)\frac{1}{I(x)} - \int_{\{y\in\Omega\,:\,I(x)<I(y)\}} w(x,y)\frac{1}{I(x)}\right); \\
\delta C^{-\mathcal{M}}_{w,0}(I) &= -\int_{y\in\Omega} w(x,y)\frac{I(y)}{(I(x)+I(y))^2}\,\mathrm{sign}_0(I(x)-I(y))\,dy \\
&= -\int_{\{y\in\Omega\,:\,I(x)>I(y)\}} w(x,y)\frac{I(y)}{(I(x)+I(y))^2} \\
&\quad + \int_{\{y\in\Omega\,:\,I(x)<I(y)\}} w(x,y)\frac{I(y)}{(I(x)+I(y))^2}.
\end{aligned}$$

Now, by direct computation, the derivative of the entropic dispersion term is given by:

$$\delta D_{\alpha,\beta}(I) = \alpha\left(1 - \frac{\mu}{I(x)}\right) + \beta\left(1 - \frac{I_0(x)}{I(x)}\right). \qquad [5.20]$$

This expression has a degree of homogeneity -1 with respect to $I(x)$, the same as the variation of the three contrast terms $C^{\varphi}_{w}(I)$.

Assume that $\alpha,\beta > 0$ are fixed. If $E^{\varphi}_{w,\varepsilon,\alpha,\beta,\mu}(I) = D_{\alpha,\beta,\mu}(I) + C^{\varphi}_{w,\varepsilon}(I)$, ε = id, log, $-\mathcal{M}$, then by linearity of the variational derivative, we have $\delta E^{\varphi}_{w,\varepsilon,\alpha,\beta,\mu}(I) = \delta D_{\alpha,\beta,\mu}(I) + \delta C^{\varepsilon}_{w,\varphi}(I)$.

The argmin of $E^{\varphi}_{w,\varepsilon,\alpha,\beta,\mu}(I)$ satisfies $\delta E^{\varphi}_{w,\varepsilon}(I) = 0$. To search for the argmin, we use a semi-implicit discrete gradient descent strategy with respect to $\log I$. The continuous gradient descent equation is:

$$\partial_t \log I = -\delta E^{\varphi}_{w,\varepsilon,\alpha,\beta,\mu}(I), \qquad [5.21]$$

being t the evolution parameter. Since $\partial_t \log I = \frac{1}{I}\partial_t I$, we have

$$\partial_t I = -I\delta E^{\varphi}_{w,\varepsilon,\alpha,\beta,\mu}(I). \qquad [5.22]$$

Using the gradient descent in $\log I$ leads to [5.22], which is related to a gradient descent approach that uses *the relative entropy as a metric*, instead of the usual quadratic distance (see [AMB 05]).

Let us now discretize our scheme: choosing a finite evolution step $\Delta t > 0$ and setting $I^k(x) = I_{k\Delta t}(x)$, $k = 0, 1, 2, \ldots$, with $I^0(x)$ being the original image, thanks to [5.20], we can write the semi-implicit discretization of [5.22] as:

$$\frac{I^{k+1}(x) - I^k(x)}{\Delta t} = \alpha\left(\frac{1}{2} - I^{k+1}(x)\right) + \beta\left(I_0(x) - I^{k+1}(x)\right) - I^k(x)\delta C^{\varphi}_{w,\varepsilon}(I^k). \qquad [5.23]$$

Now, considering the explicit expressions of $\delta C^{\varphi}_{w,\varepsilon}(I^k)$, neglecting their second terms containing S_ε (see Proposition 5.2 i), ii), iii)) and performing some easy algebraic manipulations, we obtain the equation:

$$I^{k+1}(x) = \frac{I^k(x) + \Delta t\left(\alpha\mu + \beta I_0(x) + \frac{1}{2}R^{\varphi}_{\varepsilon,I^k}(x)\right)}{1 + \Delta t(\alpha + \beta)}, \qquad [5.24]$$

where the function $R^{\varphi}_{\varepsilon,I^k}(x)$ assumes three different forms for $\varphi = \mathrm{id}, \log, -\mathcal{M}$, precisely:

$$\begin{aligned} R^{\mathrm{id}}_{\varepsilon,I^k}(x) &:= -2I^k\delta C^{\mathrm{id}}_{w,\varepsilon}(I^k) \\ &= \int_\Omega w(x,y)\frac{I^k(x)I^k(y)}{\max_\varepsilon(I^k(x), I^k(y))^2}\, s_\varepsilon(I^k(x) - I^k(y))\, dy. \end{aligned} \qquad [5.25]$$

$$R^{\log}_{\varepsilon,I^k}(x) := -2I^k\delta C^{\log}_{w,\varepsilon}(I^k) = \int_\Omega w(x,y)\, s_\varepsilon(I^k(x) - I^k(y))\, dy. \qquad [5.26]$$

$$\begin{aligned} R^{\mathcal{M}}_{\varepsilon,I^k}(x) &:= -2I^k\delta C^{-\mathcal{M}}_{w,\varepsilon}(I^k) \\ &= \int_\Omega w(x,y)\, \frac{2I^k(x)I^k(y)}{(I^k(x) + I^k(y))^2}\, s_\varepsilon(I^k(x) - I^k(y))\, dy. \end{aligned} \qquad [5.27]$$

The discrete equations corresponding to the limit $\varepsilon \to 0$ are:

$$R^{\mathrm{id}}_{0,I^k}(x) = \sum_{\{y\in\Omega\,:\,I^k(x)>I^k(y)\}} w(x,y)\frac{I^k(y)}{I^k(x)} - \sum_{\{y\in\Omega\,:\,I^k(x)<I^k(y)\}} w(x,y)\frac{I^k(x)}{I^k(y)}; \qquad [5.28]$$

$$R^{\log}_{0,I^k}(x) = \sum_{y\in\Omega} w(x,y)\,\mathrm{sign}_0(I^k(x) - I^k(y)); \qquad [5.29]$$

$$R^{-\mathcal{M}}_{0,I^k}(x) = \sum_{\Omega} w(x,y)\,\frac{2I^k(x)I^k(y)}{(I^k(x)+I^k(y))^2}\,\mathrm{sign}_0(I^k(x) - I^k(y)). \qquad [5.30]$$

5.2.1. *Stability of the iterative semi-implicit gradient descent scheme*

We assume here that $I_0 : \Omega \to [\rho, 1]$, where $\rho > 0$ is a minimum value for the initial image. We set $\rho = 1/255$, which means that we assume that I_0 does not take the value 0. In [PAL 09], the following statement about the stability of the argmin computation for the perceptual functionals has been proved.

THEOREM 5.3.– Assume that $\alpha \geq \frac{1}{1-2\rho} > 0$. Then, $\forall k \geq 1$:

- $-1 \leq R^{\varphi}_{\varepsilon,I^k}(x) \leq 1 \ \forall x \in \Omega$;
- $\rho \leq I^k(x) \leq 1 \ \forall x \in \Omega$;
- $\forall p \in [1, \infty]$:

$$\|I^{k+1} - I^k\|_p \leq \frac{1 + \Delta t\left(\frac{1}{\rho} + m_\varepsilon\right)}{1 + \Delta t(\alpha + \beta)}\|I^k - I^{k-1}\|_p,$$

where $m_\varepsilon := \max_{z\in[-1,1]} |s'_\varepsilon(z)|$.

As a result, if $\alpha + \beta > \frac{1}{\rho} + m_\varepsilon$, then the iterative scheme given in [5.24] is convergent to the unique function I^* that satisfies

$$\alpha(I^* - \mu) + \beta(I^* - I_0) - \frac{1}{2}R^{\varphi}_{\varepsilon,I^*} = 0. \qquad [5.31]$$

As usual, the $\|\cdot\|_p$ norm of a vector $v = (v_i)_{i=1}^n \in \mathbb{R}^n$, $n \geq 1$, is defined by $\|v\|_p := \left(\sum_{i=1}^n |v_i|^p\right)^{1/p}$ if $p \in [1, \infty)$ and $\|v\|_\infty := \max_{i=1,\dots,n}|v_i|$ if $p = \infty$.

Note that [5.31] is essentially (and not exactly, due to our regularization of the basic contrast variable) the Euler-Lagrange equation corresponding to the energy $E^{\varphi}_{w,\varepsilon,\alpha,\beta,\mu}$.

Note also that $\alpha + \beta > \frac{1}{\rho} + m_\varepsilon$ is not a reasonable condition in practice. The reason is that $1/\rho = 255$ and $m_\varepsilon \approx 1/\varepsilon$ for the particular nice regularization of $A(z)$ given in Examples 1) and 2) in section 5.2. Then, the values of α and/or β are too big and produce a strong attachment to the initial data and/or the value $\frac{1}{2}$; in this case, we do not have enough enhancement power. The values of α and β used in practice are much smaller, $\alpha = 255/253$ and $\beta = 1$, but they are enough to guarantee empirical stability and convergence.

5.2.2. *A general strategy for the reduction of computational complexity*

To better appreciate the simplicity of the idea behind the computational complexity reduction, it is worthwhile omitting the superscript k to avoid a cumbersome notation.

The computational complexity relative to the general form of semi-implicit gradient descent equation [5.24] is $O(N)$, with N being the total number of image pixels, for every $x \in \Omega$, which means that the computational complexity for the whole images is $O(N^2)$. Of course, this large cost is due to the term $R^{\varphi}_I(x)$.

In fact, $R^{\varphi}_I(x)$ have the same analytical structure for every choice of φ, i.e.

$$R^{\varphi}_{\varepsilon,I}(x) = \int_\Omega w(x,y)\, r^{\varphi}_{\varepsilon}(I(x), I(y))\, dy, \qquad [5.32]$$

where $r^{\varphi}_{\varepsilon}(I(x), I(y))$ is specified in equations [5.25], [5.26] and [5.27].

To reduce the complexity and obtain an algorithm that can be used in a reasonable time, at least three strategies can be followed.

The first strategy consists in localizing the computation in a circular window centered in the pixel x under analysis and discarding all the pixels that lie outside this window, using the argument that the kernel w takes values very close to 0 when the distance between pixel pairs becomes large enough (of course, this strategy implies a renormalization of w in the circular sub-image). The second strategy consists in replacing the kernel by a sparse sampling structure, for instance the local random spray technique proposed in [PRO 07].

The third strategy is the one that has been pursued in [PAL 09], which is based on polynomial approximations of the function $r_\varepsilon^\varphi(I(x), I(y))$, as we have first proposed in [BER 07] and then further refined in [PAL 09].

Let p be a generic polynomial of order n of the variables $I(x), I(y)$ and define

$$\tilde{r}_{n,\varepsilon}^{\varphi}(I(x), I(y)) = \operatorname{argmin}_p \, \|p - r_\varepsilon^\varphi\|_2, \qquad [5.33]$$

i.e. $\tilde{r}_n$ is the polynomial of order n with *minimal quadratic distance* with respect to the function φ.

It is convenient to write $\tilde{r}_{n,\varepsilon}^{\varphi}$ as follows: $\tilde{r}_{n,\varepsilon}^{\varphi}(I(x), I(y)) = \sum_{j=0}^{n} f_j^{\varepsilon,\varphi}(I(x)) I(y)^j$, where $f_j^{\varepsilon,\varphi}(I(x)) = \sum_{k=0}^{n-j} p_{k,j}^{\varepsilon,\varphi} I(x)^k$.

The numerical coefficients $p_{k,j}^{\varepsilon,\varphi}$ depend on the approximation order n, but we will not make explicit this dependence for the sake of a more readable mathematical notation.

Introducing this expression of $\tilde{r}_{n,\varepsilon}^{\varphi}$ in [5.32] instead of r_ε^φ and noting that $f_j^{\varepsilon,\varphi}$ does not depend on y, we obtain:

$$\tilde{R}_{n,\varepsilon,\varphi}^{\varphi}(x) = \sum_{j=0}^{n} f_j^{\varepsilon,\varphi}(I(x)) \int_\Omega w(\|x-y\|) I(y)^j dy, \qquad [5.34]$$

but $\int_\Omega w(\|x-y\|) I(y)^j dy = (w * I^j)(x)$, i.e. the convolution between the kernel w and the j-th power of the image I, hence

$$\tilde{R}_{n,\varepsilon,\varphi}^{\varphi}(x) = \sum_{j=0}^{n} \sum_{k=0}^{n-j} p_{k,j}^{\varepsilon,\varphi} I(x)^k (w * I^j)(x). \qquad [5.35]$$

The n convolutions $w * I^j$ can be *pre-computed* through the FFT (Fast Fourier Transform), which has computational complexity $O(N \log N)$, thus drastically decreasing the computational time.

The degree n of the polynomial is a parameter that controls the precision of the polynomial approximation. In our tests, we have found that $n = 9$ is a good trade-off between time cost and approximation precision.

Online demonstrations for these techniques can be found in [GET 12] and [FER 15]. A recent improvement of this approximation technique, which makes use of the so-called Bernstein polynomials, has been proposed in [PIE 16].

5.2.3. *Results*

In this section, we present some results of the algorithms derived by the model described above with the three different choices of φ =id, log, $-\mathcal{M}$. For a more complete analysis of the results with respect to variations of parameters, see [PAL 09].

The results presented here have been obtained by using the implementation [FER 15], publicly available on the website IPOL, with the following parameters: $\alpha = \beta = 1.2$, $\varepsilon = 1/20$, w: Gaussian kernel with standard deviation equal to 1/5 of the length of the image diagonal.

Let us start by showing in Figure 5.1 how a low-key image is handled by the variational algorithm versus the von Kries algorithm (normalization over the maximum intensity in the three chromatic channels separately) and the automatic color enhancement performed by Photoshop. It can be seen that the perceptual-inspired color enhancement avoids the color shifting of the von Kries method, which shows many more details than the automatic Photoshop algorithm. Also, recall from Figure 4.1 that histogram equalization has a dramatic effect on this image, which is absent in our perceptually inspired modification.

The intra-variations of the variational algorithm with respect to different choices of φ are perceptually small, the major difference being that, in general, $\varphi = \log$ corresponds to the brightest image, but with less saturated colors with respect to the other two choices.

Figure 5.1. *First row from left to right: original image and results of the global von Kries algorithms and the automatic color correction performed by Photoshop. Second row from left to right: result of the variational algorithms with φ =id,log,$-\mathcal{M}$. For a color version of the figure, see www.iste.co.uk/provenzi/color.zip*

In Figure 5.2, we can see the effect of the variational algorithm with φ =id on an image with haze and the difference with respect to histogram equalization.

Finally, in Figure 5.3, we can see the behavior of the perceptually inspired variational algorithms with respect to the images with color cast and the comparison with the von Kries and histogram equalization methods. Note that the von Kries algorithm is not able to completely remove the color cast and histogram equalization creates a dramatic color shift.

It is important to underline that the main aim of the research presented in this chapter is not to build the most efficient color correction algorithm, but to show that how by carefully modifying the histogram equalization functional guided by the HVS features, it is possible to strongly limit the typical problems related to a large color shift and excessive amplification of contrast even working in the three separated chromatic channels. The techniques developed here may be used in applications where a parallel elaboration is needed, and they can also be extended to more than three wavebands, as in hyperspectral imaging.

Recent and extremely well-performing techniques to control color shift and preserve the original hue have been proposed in [NIK 14] and [PIE 16].

5.3. Embedding existing perceptually inspired color correction models in the variational framework

One of the main theoretical achievements of [PAL 09] is the proof that the perceptual variational framework can embed and link together in a clear way two of the most used perceptually inspired color correction algorithms: the famous Retinex of Land and McCann [LAN 71] and ACE, automatic color equalization [RIZ 03].

Figure 5.2. *Row-wise from left to right: original image and results of the variational algorithms with φ =id, the global von Kries algorithms and histogram equalization. For a color version of the figure, see www.iste.co.uk/provenzi/color.zip*

Figure 5.3. *Row-wise from left to right: original image and results of the variational algorithms with φ =id, the global von Kries algorithms and histogram equalization. For a color version of the figure, see www.iste.co.uk/provenzi/color.zip*

The embedding of ACE is simple to discuss: if we choose $\varphi = \log$, $\mu = 1/2$, $\alpha = 1$ and $\beta = 0$ in equation [5.24], then, as proved in [BER 07], we obtain, as a particular instance, the ACE algorithm (see equations [3.37] and [3.38)].

The embedding of Retinex has proved to be more difficult, in fact, equations [3.3] and [3.15] seem very distant from the variational framework just discussed. However, in the paper [BER 09], it has been proved that a continuous (anti-) symmetrized version of Retinex can be considered as a particular instance of the variational framework described before. In order to understand how this is possible, let us come back to the lightness formula [3.15], i.e.

$$L_{0,\vec{\gamma}}(x) = \frac{1}{N} \sum_{k=1}^{N} \frac{I(x)}{I(y_{H_k})}. \qquad [5.36]$$

As already anticipated in Chapter 3, Land and McCann proposed a further Retinex mechanism, the scaling, implemented via a strictly increasing function

$f : (0,1] \to (0,1]$ such that $f(r) \geq r$ for all $r \in (0,1]$ applied to the ratio $r = \frac{I(x)}{I(y_{H_k})}$, so that the Retinex lightness formula becomes:

$$L_{0,\vec{\gamma},f}(x) = \frac{1}{N}\sum_{k=1}^{N} f\left(\frac{I(x)}{I(y_{H_k})}\right). \qquad [5.37]$$

The reset mechanism of Retinex and the scaling operation can be merged: in fact, we can extend f to $(0,+\infty)$ preserving its continuity by defining:

$$\hat{f}(r) = \begin{cases} f(r) & \text{if } r \in (0,1] \\ 1 & \text{if } r \in [1,+\infty). \end{cases}$$

It is clear that applying this new scaling function $\hat{f}$ to the ratios $I(x)/I(y)$, with x fixed and y that varies in Ω, jointly implements the scaling and the reset mechanism.

Now we have all the elements to introduce the continuous version of the Retinex algorithm presented in [BER 09] under the name "Kernel-Based Retinex" (KBR). Given $x \in \Omega$, let $Y_{w,x}$ be the random variable modeling the selection of a pixel in the neighborhood of x according to the density $w(x,y)$. The output $L_w^{\text{KBR}}(x)$ of the KBR algorithm at the pixel x is defined as the conditional expectation of $\hat{f}\left(\frac{I(x)}{I(Y_{w,x})}\right)$ with respect to the distribution w of pixels around x, i.e.

$$L_w^{\text{KBR}_w}(x) = \mathbb{E}_{Y_{w,x}}\left[\hat{f}\left(\frac{I(x)}{I(Y_{w,x})}\right)\right]. \qquad [5.38]$$

This formula is used independently for each color channel and can be written more explicitly as:

$$L_w^{\text{KBR}}(x) = \sum_{\{y\in\Omega:I(y)\geq I(x)\}} w(x,y)\, f\left(\frac{I(x)}{I(y)}\right) + \sum_{\{y\in\Omega:I(y)<I(x)\}} w(x,y). \qquad [5.39]$$

All the basic properties of Retinex recalled in Chapter 3 are faithfully implemented in [5.39]: KBR is founded on the propagation of a two-pixel ratio comparison between the fixed target x and the generic pixel y that runs across the image; these comparisons are then subjected to the reset and scaling performed by $\hat{f}$ and, finally, locally averaged with weight w, in order to produce the value of $L_w^{\mathrm{KBR}}(x)$.

To study the action of KBR of pixel intensities, it is useful to rewrite [5.39] introducing the functions:

$$\operatorname{sign}^+(\xi) := \begin{cases} 1 \text{ if } \xi > 0, \\ \frac{1}{2} \text{ if } \xi = 0, \\ 0 \text{ if } \xi < 0, \end{cases} \qquad \operatorname{sign}^-(\xi) = 1 - \operatorname{sign}^+(\xi),$$

so that equation [5.39] can be rewritten as:

$$\begin{aligned} L_w^{\mathrm{KBR}}(x) = &\sum_{y\in\Omega} w(x,y)\, f\left(\frac{I(x)}{I(y)}\right) \operatorname{sign}^+(I(y) - I(x)) \\ &+ \sum_{y\in\Omega} w(x,y) \operatorname{sign}^-(I(y) - I(x)). \end{aligned} \qquad [5.40]$$

Thanks to equation [5.40], we can verify that KBR always increases brightness as the original Retinex implementation. In fact, since $f(r) \geq r$ for all $r \in (0, 1]$, then $f\left(\frac{I(x)}{I(y)}\right) \geq \frac{I(x)}{I(y)} \geq I(x)$, so:

$$\begin{aligned} L_w^{\mathrm{KBR}}(x) \geq &\sum_{y\in\Omega} w(x,y)\, I(x) \operatorname{sign}^+(I(y) - I(x)) \\ &+ \sum_{y\in\Omega} w(x,y) \operatorname{sign}^-(I(y) - I(x)) \end{aligned} \qquad [5.41]$$

moreover, with $I(x) \leq 1$, we can write:

$$\begin{aligned} L_w^{\mathrm{KBR}}(x) \geq &\sum_{y\in\Omega} w(x,y)\, I(x) \operatorname{sign}^+(I(y) - I(x)) \\ &+ \sum_{y\in\Omega} w(x,y)\, I(x) \operatorname{sign}^-(I(y) - I(x)) \\ &= I(x) \sum_{y\in\Omega} w(x,y)\ [\operatorname{sign}^+(I(y) - I(x)) + \operatorname{sign}^-(I(y) - I(x))] \\ &= I(x) \sum_{y\in\Omega} w(x,y) = I(x), \end{aligned} \qquad [5.42]$$

having used the fact that the kernel is normalized. As in the original formulation, this property implies that overexposed pictures could not be enhanced with Retinex unless we use a post-processing stage and that further iterations of Retinex keep on increasing the intensity until a white image is reached.

In order to obtain a two-sided contrast modification able to enhance both overexposed and underexposed images, it is interesting to analyze what happens if we anti-symmetrize the analytic expression of equation [5.40].

As proved in [BER 09], if we anti-symmetrize the function $f\left(\frac{I(x)}{I(y)}\right) \operatorname{sign}^+(I(y) - I(x))$ on the region $\{x \in \Omega : I(y) \leq I(x)\}$, then we obtain the equations of the variational model described by the energy $E^{\mathrm{id}}_{w,0,1,0,\mu}$ presented in section 5.1. Thus, this last model can be considered as an anti-symmetric regularized version of the continuous version of Retinex represented by KBR.

5.3.1. *Alternative variational and EDP formalizations of Retinex-like algorithms*

Besides the variational framework described in the previous sections, in the literature there exist alternative variational models of Retinex-like algorithms and also formalizations based on partial differential equations (PDE). The aim of the discussion contained in this section is not to give an exhaustive list, rather to discuss the main features of the most famous alternative mathematical formalizations of Retinex-like algorithms present in the literature.

The first authors to embed a Retinex-like algorithm in a variational framework were Kimmel and colleagues in [KIM 03]. They did not consider the original Land's ratio-threshold-reset Retinex, but Horn's interpretation. In fact, they started from the logarithmic equation $\log I_c(x) = \log S_c(x) + \log L_c(x)$, $c \in \{R, G, B\}$ and tried to solve it with respect to $\log L_c(x)$ by imposing the hypothesis of smoothness on the illuminant part of the logarithmic image. Once we have obtained an estimation of the illumination, they could infer the reflectance information $S_c(x)$. This one then undergoes suitable transformations and gives an illuminant-invariant version of the original image.

It is important to underline a fundamental difference between this variational technique and the one presented in the previous sections: *here contrast enhancement of the original image* $\log I_c(x)$ *is obtained by decreasing the contrast of the illuminant image* $\log L_c(x)$. In fact, $\log I_c(x)$ is measured by the camera and so it is a fixed data, $\log L_c(x)$ is estimated by using a smoothness prior, thus the estimated reflectance $\log S_c(x) = \log I_c(x) - \log L_c(x)$, or $S_c(x) = I_c(x)/L_c(x)$ is forced to have a stronger contrast than the original image data. Instead, the variational principles previously discussed *act directly on the contrast of the original image*, without taking into account the separation between reflectance and illuminant and related approximations and priors.

Let us now turn to the details of the functional proposed in [KIM 03]. By avoiding the subscript c and by using the notations of this book, the energy of Kimmel and colleagues can be expressed as follows:

$$\begin{aligned} E_{\alpha,\beta}(\log L) = \int_\Omega & [|\nabla \log L(x)|^2 + \alpha(\log L(x) - \log I(x))^2 \\ & + \beta|\nabla(\log L(x) - \log I(x))|^2]dx \end{aligned} \qquad [5.43]$$

with the constraints $\log L(x) \geq \log I(x)$, because the reflectance $S(x)$ is always between 0 and 1, and the boundary condition $\langle \nabla \log L, \vec{n} \rangle = 0$ on $\partial\Omega$, i.e. $\log L$ orthogonal to the normal $\vec{n}$ to the boundary $\partial\Omega$ of Ω.

The first term of the functional forces spatial smoothness on the illumination L. The authors chose that particular analytical form because the Euler-Lagrange equation associated with $\int_\Omega |\nabla \log L(x)|^2\, dx$ is the Laplace PDE $\Delta \log L = 0$, whose steepest descent solution is equivalent to a Gaussian smoothing. The second penalty term forces a proximity between $\log L$ and $\log I$, so that their difference $\log S$, the logarithmic reflectance, tends to 0, i.e. the reflectance R tends to 1, or white. The authors declare that the principal objective of this term is to regularize the problem, so that it is better conditioned in view of a numerical solution and they set the constant α to a very small value not to force too much $\log L$ towards $\log I$. The third term represents a Bayesian penalty, which forces reflectance gradients to be smooth. The authors declared to have introduced it to force R to be visually pleasing, without abrupt variations. The choice of a quadratic expression is made to maintain the model simple: defined in this way, the minimization problem has a Quadratic Programming (QP) form that the authors solve via a

Projected Normalized Steepest Descent (PNSD) algorithm, accelerated by a multi-resolution technique.

Morel, Petro and Sbert [MOR 10] analyzed Land's original Retinex model [LAN 64] without the reset mechanism. They showed that if the Retinex paths are interpreted as symmetric random walks, then Retinex is equivalent to the following Neumann problem for a Poisson equation:

$$\begin{cases} -\Delta L(x) = F(x) & x \in \Omega \\ \frac{\partial L(x)}{\partial \vec{n}} = 0 & x \in \partial\Omega, \end{cases}$$

where F is a suitable scalar field, see [MOR 10] in page 2830. This turns out to be very similar to Horn's and Blake's equations on one side, and to the so-called "Poisson editing" equations proposed by Perez *et al.* in [PÉR 03]. [ZOS 15] further extended the link among different versions of Retinex by considering sparsity constraints.

Let us now consider the algorithm STRESS, introduced in section 3.7. We recall that the basic information needed by STRESS is given by the two envelope functions $E_{\min}$ and $E_{\max}$ which, in the original formulation, are computed through the same random spray technique of RSR [PRO 07]. To avoid the typical noise problems related to this technique, in [SIM 12], the authors proposed to compute the envelope functions via the minimization of a functional based on the total variation, instead of using the random spray technique. For this reason, the corresponding algorithm is called STRETV and corresponds to the minimization of the following functional for E (in this case E denotes the envelope and not the energy functional):

$$\int_\Omega [|\nabla E(x)| + \frac{\lambda}{2}|E(x) - I(x)|^2]dx \qquad [5.44]$$

subjected to $E(x) \geq I(x)$ to compute $E_{\max}$ and to $E(x) \leq I(x)$ for $E_{\min}$.

The minimization of the first (total variation) term assures the spatial smoothness of the envelope functions, the second term is a fidelity term used not to differ too much from the original image values. The authors declare that the coefficient λ must be $\ll 1$ for good results. The authors do not specify if they consider a spatial kernel to localize their computation or not.

The last variational formalization that we discuss here is that presented in [LEC 16] relative to the termite Retinex. Here, an energy functional is taken into account to determine the geometry of the paths used by Retinex. Considering a fixed pixel $x \in \Omega$, the authors search for the path $\gamma : [0, 1] \to \Omega$, $\gamma(0) = x$, that minimizes the energy functional defined by:

$$E(\gamma) = \int_0^1 [\frac{1}{1 + (D^2 - ||x - \gamma(s)||^2)||\nabla I(\gamma(s))||^2} + \theta(\gamma(s))]ds, \qquad [5.45]$$

where D is the diagonal of Ω and 1 is introduced to avoid singularities if the denominator is 0. The paths that minimize $E(\gamma)$ are those which balance the fact to remain as close to x as possible and, simultaneously, to explore image areas with high values of the gradient. Both features maximize the denominator of the first term. The interpretation is that if x lies in an area with a high density of edges, then the path γ will not go too far from x, instead, if x lies in a rather homogeneous area, γ will be forced to explore the image points far away from x to find the important edge information. $\theta(\gamma(s))$, the so-called "poison term", is set to zero at the beginning, and it increases each time a path has been traveled, to prevent from exploring the same image area all the time.

Once a set of N path has been selected, the intensity $I(x)$ of the pixel x in each separate chromatic channel is modified with the Retinex formula [3.15].

5.4. Variational interpretation of the Rudd-Zemach model of achromatic induction

In this section, we will discuss an alternative version of the Rudd-Zemach model presented in section 3.4 which leads to analogous predictions and that has the advantage of being understandable in terms of variational principles. The choice made by Rudd and Zemach to pass from equation [3.31] to equation [3.32] during the description of their WLLR model is questionable. The reason is that the weights of spatially local induction $w_1, w_2, \ldots$ should decrease with the distance between two point of the visual scene; however, in the decomposition of the chain of ratios in equation [3.30], the points corresponding to the indexes $k - 1$ and k and those corresponding to k and $k + 1$ have exactly the same distance. Instead, if we keep the target point i fixed and consider points at an increasing distance from it, then it is perfectly correct to consider weights of decreasing strength.

These considerations have been thoroughly analyzed in previous works on the interpretation of Retinex [BER 09, PRO 05, PRO 07, PRO 08]. Starting from this more coherent Retinex interpretation, we propose the following alternative definition of logarithmic brightness of i, denoted as $\log \Psi(i)$:

$$\log\,\Psi(i) \equiv \sum_{k=i}^{j-1} w_{k-i+1} \log \frac{L_i}{L_{k+1}} + \mu, \qquad [5.46]$$

where, as for $\log\,\Psi(i)$, $\mu \in \mathbb{R}$ is an arbitrary constant. If we compare the formulae of $\log\,\Phi(i)$ and $\log\,\Psi(i)$, we see that in the latter the numerator of each ratio is L_i, this means that the contribution to $\Psi(i)$ is given by the logarithmic ratios between $L(i)$ and the luminance of all the other patches in the visual field, weighted by the distance between i and the patches.

It is easy to see that this model also predicts a linear relationship between $\log L_{D_M}^{\text{Match}}$ and $\log L_{R_T}$ with slopes in $(-1, 0)$ for the visual match in Wallach's experiment. In fact, developing equation [5.46] for both sides of the visual field and matching the brightness, we obtain:

$$w_1 \log \frac{L_{D_M}^{\text{Match}}}{L_{R_M}} + w_2 \log \frac{L_{D_M}^{\text{Match}}}{L_B} + \mu = w_1 \log \frac{L_{D_T}}{L_{R_T}} + w_2 \log \frac{L_{D_T}}{L_B} + \mu, \qquad [5.47]$$

solving this equation w.r.t. $\log L_{D_M}^{\text{Match}}$ we have:

$$\log L_{D_M}^{\text{Match}} = \log L_{D_T} + \frac{w_1}{w_1 + w_2} \log L_{R_M} - \frac{w_1}{w_1 + w_2} \log L_{R_T}. \qquad [5.48]$$

We stress that the absolute value of the slope $w_1/(w_1 + w_2) = \beta_1$ is naturally bounded between -1 and 0, so it also accounts for Rudd-Zemach's observations, even without the hypothesis that $w_2 < w_1$. The weight w_2 can be expressed in terms of the measured value of β_1 as follows:

$$w_2 = \frac{1 - \beta_1}{\beta_1} w_1. \qquad [5.49]$$

If we now add two other rings in both the match and target bipartite field, and again use the outermost ring in the target field as an independent variable, then, by direct computation, it can be proved that expression of the induction weight w_3 corresponding to this new, and more distant, ring predicted by our model is the following:

$$w_3 = \frac{1-\beta_2}{\beta_2} w_2 - w_1, \qquad [5.50]$$

where $\beta_2 \in (0, 1)$ is the absolute value of the measured slope of the linear relationship in the logarithmic domain between the $L_{D_M}^{\mathrm{Match}}$ and the logarithmic luminance of the new outermost target ring. By iterating the process, we find the following formula for the n-th induction weight (corresponding to the configuration given by one disk and $n-1$ rings):

$$\begin{cases} w_2 = \frac{1-\beta_1}{\beta_1} w_1 \\ w_n = \frac{1-\beta_{n-1}}{\beta_{n-1}} w_{n-1} - \sum_{k=1}^{n-2} w_k \qquad n \geq 3, \end{cases} \qquad [5.51]$$

where $\beta_{n-1} \in (0, 1)$ is the absolute value of the measured slope of the linear relationship in the logarithmic domain between the $L_{D_M}^{\mathrm{Match}}$ and the logarithmic luminance of the outermost $(n-1)$-th target ring.

It is natural to search for a generalization of Rudd-Zemach's model that is valid for arbitrary spatial configurations and not just for the special one discussed in their experiments. To do that, we will distinguish between a discrete and a continuous context. In a discrete context, we will denote the discrete visual field with the lattice $\Omega \subset \mathbb{Z}^2$, the coordinates of two arbitrary points in Ω as $x = (x_1, x_2)$, $y = (y_1, y_2)$ and the corresponding luminance values as $L(x)$ and $L(y)$, respectively. The equivalent of the logarithmic brightness of x defined in equation [5.46] in this case is:

$$\log \Psi(x) = \sum_{y \in \Omega} w(\|x-y\|) \log \frac{L(x)}{L(y)} + \mu \qquad \text{Discrete context} \qquad [5.52]$$

where $w(\|x-y\|)$ is, as usual, a weight function which decreases with the distance $\|x-y\|$ and μ is an arbitrary constant. In a continuous context, Ω is a subset of $\mathbb{R}^2$, and of course the discrete sum must be replaced by an integral:

$$\log \Psi(x) = \int_{\Omega} w(\|x-y\|) \log \frac{L(x)}{L(y)}\, dy + \mu \qquad \text{Continuous context} \qquad [5.53]$$

The advantage of this formulation, over that of Rudd and Zemach, is that it is possible to provide a variational interpretation of formulae [5.52] and [5.53], as the following proposition states [GRO 16].

PROPOSITION 5.1–. The achromatic logarithmic brightness $\Psi(x)$ of an arbitrary point $x \in \Omega$ is the argmin of the functional:

$$E_w(\log L) = \frac{1}{2}\sum_{x\in\Omega}\left(\log\frac{L(x)}{\mu}\right)^2 - \frac{1}{4}\sum_{x\in\Omega}\sum_{y\in\Omega} w(\|x-y\|)\left(\log\frac{L(x)}{L(y)}\right)^2, \qquad [5.54]$$

in the discrete scenario, and of the functional:

$$E_w(\log L) = \frac{1}{2}\int_{\Omega}\left(\log\frac{L(x)}{\mu}\right)^2 dx - \frac{1}{4}\iint_{\Omega^2} w(\|x-y\|)\left(\log\frac{L(x)}{L(y)}\right)^2 dxdy. [5.55]$$

in the continuous scenario.

The consequence of this proposition is that the logarithmic brightness values $\Psi(x)$ can be interpreted as being *the optimal balance between two opposite mechanisms*: one that tends to adjust all stimuli to a constant, uniform value, and the other that tends to do the opposite, i.e. to amplify as much as possible the differences among all stimuli in a local, or context-driven, way. This shows how the variational generalization of Rudd-Zemach's model can be linked to the framework described before in this chapter.

5.5. Perceptual enhancement in the wavelet domain

Let us now present the wavelet version of the variational model presented in section 5.1.

Let us start by very briefly recalling the basic information about wavelet theory in one dimension, then we will extend the discussion to 2D wavelets, the main reference for all the results quoted hereafter is [MAL 99]. A 1D (mother) wavelet $\psi \in L^2(\mathbb{R})$ is a unit norm and null-mean function. Of course this is possible only if ψ oscillates, but, unlike infinite waves, wavelets can have compact support. The ψ-wavelet transform $W_\psi f$ of $f \in L^2(\mathbb{R})$ in the point ξ at the scale s is given by the inner product

$W_\psi f(\xi, s) = \int_{\mathbb{R}} f(x)\frac{1}{\sqrt{s}}\overline{\psi}\left(\frac{x-\xi}{s}\right)dx$. $W_\psi f$ gives a “measure of similarity” between f and ψ around the point ξ at the scale s. So, if a signal is constant or do not vary “too much” in the support of a wavelet, then its wavelet transform will be zero or very small, this is how wavelets provide a multi-scale information about the *local contrast* of a signal.

The set $\{\psi_{j,k}\}_{(j,k)\in\mathbb{Z}^2} \subset L^2(\mathbb{R})$ given by $\psi_{j,k}(x) \equiv \frac{1}{\sqrt{2^j}}\psi\left(\frac{x-2^j k}{2^j}\right)$ is a complete orthonormal system of $L^2(\mathbb{R})$. Moreover, $L^2(\mathbb{R})$ can be recovered by the closure of the union of a sequence of nested closed subspaces $V_j \subset V_{j-1}$ with suitable properties (see [MAL 99] for more details). The orthogonal projections of $f \in L^2(\mathbb{R})$ onto V_j and V_{j-1} give the approximation of f at the scales 2^j and 2^{j-1}, respectively. The 2^j-approximation is coarser and the missing details with respect to the finer 2^{j-1}-approximation are contained in the orthogonal complement W_j of V_j in V_{j-1}: $V_{j-1} = V_j \oplus W_j$. W_j is called the j-th *detail space* and it can be proved that the orthogonal projection of f on W_j is given by $P_{W_j} f = \sum_{k\in\mathbb{Z}}\langle f, \psi_{j,k}\rangle\psi_{j,k} \equiv \sum_{k\in\mathbb{Z}} d_{j,k}\psi_{j,k}$. The coefficients $d_{j,k}$ are called *detail coefficients of f at the scale* 2^j. Fine-scales detail coefficients at fine scale are sparse, in fact, they are non-null only when the support of $\psi_{j,k}$ intersects a high contrast zone, i.e. around sharp edges.

Finally, let us recall that every wavelet ψ is related to a mirror filter h and to a function ϕ, called *scale function*, through the following equation that involves their Fourier transforms: $\hat{\psi}(2\omega) = \frac{1}{\sqrt{2}}e^{-i\omega}\hat{h}^*(\omega+\pi)\,\hat{\phi}(\omega)$, see [STR 96] for a complete and detailed description of how to generate wavelets using the filter design methodology. ϕ appears in the orthogonal projection of a signal f onto the approximation space V_j, in fact it can be proved that $P_{V_j} f = \sum_{k\in\mathbb{Z}}\langle f, \phi_{j,k}\rangle\phi_{j,k} \equiv \sum_{k\in\mathbb{Z}} a_{j,k}\phi_{j,k}$, where $\phi_{j,k}(x) = \frac{1}{\sqrt{2^j}}\phi\left(\frac{x-2^j k}{2^j}\right)$ and $a_{j,k}$ are called *approximation coefficients* at the scale 2^j. It follows that $P_{V_{j-1}} f = P_{V_j} f + P_{W_j} f = \sum_{k\in\mathbb{Z}} a_{j,k}\phi_{j,k} + \sum_{k\in\mathbb{Z}} d_{j,k}\psi_{j,k}$.

In practical applications, we are interested in a multi-resolution analysis between two fixed scales 2^L and 2^J, $L, J \in \mathbb{Z}$, $L < J$. In this case $V_{J-1} = V_J \oplus W_J$, $V_{J-2} = V_{J-1} \oplus W_{J-1} = V_J \oplus W_J \oplus W_{J-1}$ and so on, thus $V_L = V_J \oplus \bigoplus_{2^J \geq 2^j \geq 2^{L+1}} W_j$. For this reason, following [MAL 99], we say that a discrete orthogonal wavelet multi-resolution representation of a one-dimensional signal f between two fixed scales 2^L and 2^J, $L, J \in \mathbb{Z}$, $L < J$, is given by the collection of detail coefficients $\{d_{j,k}\}$ at all scales, completed by the approximation coefficients at the coarser scale, i.e. $\{a_{J,k}\}$.

When we deal with 2D signals, as images, we have to consider a multi-resolution analysis of $L^2(\mathbb{R}^2)$. Multidimensional wavelet bases can be generated with tensor products of separable basis functions defined along each dimension. In this case, an orthogonal wavelet multi-resolution representation between two scales 2^L and 2^J, $L, J \in \mathbb{Z}$, $L < J$, is given by three sets of detail coefficients $\{d^H_{j,k}, d^V_{j,k}, d^D_{j,k}\}$ at all scales, which correspond to the *horizontal, vertical and diagonal detail coefficients*, respectively, completed by the approximation coefficients at the coarser scale, i.e. $\{a_{J,k}\}$.

As seen in this chapter, the perceptual color correction proposed in [PAL 09] is performed through a local contrast enhancement balanced by the action of an adjustment term around the average value plus a conservative term that avoids over-enhancement. Wavelet detail coefficients are related to local contrast, let us see how this fact has been used in [PRO 14] to provide a wavelet-based framework for perceptually inspired color correction.

The general scheme of the algorithm is the following:

1) Consider the coarsest approximation coefficients $\{a_{J,k}, k \in \Omega\}$, and modify them to implement adaptation to the average gray level in the wavelet domain (according to equation [5.56] found in section 5.5.1);

2) Fix these new approximation coefficients and use them along with $\{d^\ell_{J,k}, k \in \Omega\}$, $\ell = H, V, D$, to modify the horizontal, vertical and diagonal detail coefficients according to the equations of theorem 5.4 found in section 5.5.2. This will implement local contrast enhancement in the wavelet domain at the scale 2^J;

3) Pass to the scale 2^{J-1} and compute the approximation coefficients by summing the approximation and detail coefficients just computed at the scale 2^J;

4) Fix these approximation coefficients and we repeat step 2 at the scale 2^{J-1};

5) Iterate this scheme until reaching the finest scale. As an optional step, we can operate a linearly scaling of the minimum value towards 0 and of the maximum towards 1.

The equations quoted in the scheme above will be presented and analyzed in full detail in sections 5.5.1 and 5.5.2, but before doing that it is convenient to make some assumptions that will greatly simplify the exposition.

First of all, since changing the sign of a wavelet coefficient can result in drastic modifications of an image, we will modify only the *absolute value* of the wavelet coefficients, restoring the original sign at the end of the computation.

Moreover, in every scale 2^j, only coefficients with magnitude bigger than a fixed threshold $T_j > 0$ will be considered, the others will be left unchanged to avoid intensification of noise. Thus we will deal with *positive, bounded and finite* sequences of wavelet coefficient magnitudes.

To simplify the notation, we will avoid the superscript ℓ in the detail coefficients, by making the implicit assumption that the operations are repeated on the horizontal (H), vertical (V) and diagonal (D) detail coefficients.

The variability of the scale coefficient 2^j will be confined within the scales 2^L and 2^J, $L, J \in \mathbb{Z}$, $L < J$, with 2^L being the finest and 2^J the coarsest. Typically $J - L$ ranges between 2 and 10, depending on the image dimension. Finally, with the notation $k \in \Omega$, we will implicitly assume a column-wise ordering of Ω, the spatial support of the image, so that Ω can be seen as a finite subset of $\mathbb{Z}$.

5.5.1. *Adjustment to the average value in the wavelet domain*

Let us first consider the effect of adaptation to the average level. If we were dealing with Fourier transforms, the average image intensity value μ would be represented by the zero-order Fourier coefficient, in the wavelet domain there is no such direct correspondence. However, since the coefficients $\{a_{j,k},\ k \in \Omega\}$ represent the image approximation at the scale 2^j, a natural analogue of the average value μ in the wavelet framework at the scale 2^j is represented by $\overline{a}_j \equiv \frac{1}{|\Omega|} \sum_{k\in\Omega} a_{j,k}$, i.e. the average approximation coefficient.

We also stress that we only need to modify the approximation coefficients of the coarsest scale, since this modification will be propagated to finer scales. Thus, we implement the adaptation to the average value at the coarser scale balanced by the adjustment to the original values through this convex linear combination:

$$a_{J,k} \equiv \alpha\overline{a}_J + (1-\alpha)a^0_{J,k}, \qquad [5.56]$$

where $\{a^0_{J,k},\ k \in \Omega\}$ is the original sequence of approximation coefficients at the scale 2^J and $\alpha \in [0,1]$ is a suitable weight coefficient. The bigger the α, the stronger the adjustment to the average value $\overline{a}_J$ and vice versa.

5.5.2. *Local contrast enhancement in the wavelet domain*

Let us now consider local contrast enhancement. We have remarked that the two most important features of the contrast functional $E^{\varphi}_{w,\alpha,\beta,\mu}(I)$ described in section 5.1 are the fact that it enhances contrast *locally* and in an *illuminant-independent* way. In order to maintain these characteristics also in the wavelet domain, in [PRO 14] the following local contrast enhancement functional at the scale 2^j has been proposed:

$$C_{w_j,\varphi,\{a_{j,k}\}}(\{d_{j,k}\}) \equiv \sum_{k\in\Omega} w_j\, \varphi\left(\frac{a_{j,k}}{d_{j,k}}\right), \qquad 2^J \geq 2^j \geq 2^{L+1}, \qquad [5.57]$$

where w_j are positive coefficients that permit to differentiate the contrast enhancement action depending on the scale 2^j and $\varphi : [0,\infty) \to [0,\infty)$ is a differentiable monotonically increasing function such that $\varphi(r) \to +\infty$ as $r \to \infty$.

We stress that the approximation coefficients are passed to the functional C as fixed parameters in every scale, from the coarsest to the finest. In particular, the approximation coefficients used in the coarsest scale are those defined in equation [5.56].

$C_{w_j,\varphi,\{a_{j,k}\}}$ is minimized when the ratio between the approximation and detail coefficients decreases, but since the approximation coefficients are fixed at each scale, the minimization of $C_{w_j,\varphi,\{a_{j,k}\}}$ corresponds to an intensification of the coefficients $d_{j,k}$. This implies a local and multi-scale contrast enhancement of the image. The locality depends both on the mother wavelet chosen (because different mother wavelets have different shape) and on the scale 2^j at which one operates: the finer the scale, the more local is contrast enhancement and vice versa.

Furthermore, the invariance with respect to global illumination changes, in the sense of the von Kries model [VON 02], is guaranteed by the fact that also the functional $C_{w_j,\varphi,\{a_{j,k}\}}$ is *homogenous of degree 0*, i.e. so the transformation $I \mapsto \lambda I$, $\lambda > 0$ will have no effects on $C_{w_j,\varphi,\{a_{j,k}\}}$ and its Euler-Lagrange equations.

In order to prevent an excessive magnification of the original detail coefficients, whose absolute value is denoted as $d^0_{j,k}$, a conservative term should be introduced. To maintain dimensional coherence with $C_{w_j,\varphi,\{a_{j,k}\}}$, an entropic dispersion functional is a suitable choice:

$$\mathcal{D}_{d^0_{j,k}}(\{d_{j,k}\}) \equiv \sum_{k\in\Omega}\left[d^0_{j,k}\log\frac{d^0_{j,k}}{d_{j,k}} - \left(d^0_{j,k} - d_{j,k}\right)\right], \quad 2^J \geq 2^j \geq 2^{L+1}. \quad [5.58]$$

Combining these two effects, we can define the energy functional that realizes local contrast enhancement as $\mathcal{E}_{w_j,\varphi,\{a_{j,k}\},d^0_{j,k}} = C_{w_j,\varphi,\{a_{j,k}\}} + \mathcal{D}_{d^0_{j,k}}$, i.e.

$$\mathcal{E}_{w_j,\varphi,\{a_{j,k}\},d^0_{j,k}} \equiv \sum_{k\in\Omega}\left[w_j\varphi\left(\frac{a_{j,k}}{d_{j,k}}\right) + d^0_{j,k}\log\frac{d^0_{j,k}}{d_{j,k}} - \left(d^0_{j,k} - d_{j,k}\right)\right], \quad [5.59]$$

with $2^J \geq 2^j \geq 2^{L+1}$. The following theorem ensures the existence of a minimum of $\mathcal{E}_{w_j,\varphi,\{a_{j,k}\},d^0_{j,k}}$ and determines the corresponding Euler-Lagrange equations. Its proof can be found in [PRO 14].

THEOREM 5.4.– There exists a minimum of the functional $\mathcal{E}_{w_j,\varphi,\{a_{j,k}\},d^0_{j,k}}$. Moreover, the Euler-Lagrange equations for the detail coefficients are:

$$\frac{\partial\mathcal{E}_{w_j,\varphi,\{a_{j,k}\},d^0_{j,k}}}{\partial\{d_{j,k}\}}(d_{j,k}) = 0 \iff d_{j,k} = d^0_{j,k} + w_j\varphi'\left(\frac{a_{j,k}}{d_{j,k}}\right)\frac{a_{j,k}}{d_{j,k}}, \quad [5.60]$$

where φ' denotes the derivative of φ. In particular, when $\varphi \equiv \mathrm{id}$,

$$\frac{\partial\mathcal{E}_{w_j,\{a_{j,k}\},d^0_{j,k}}}{\partial\{d_{j,k}\}}(d_{j,k}) = 0 \iff d_{j,k} = d^0_{j,k} + w_j\frac{a_{j,k}}{d_{j,k}}. \quad [5.61]$$

In Theorem 5.4, the role of the identity has been highlighted because it is the easiest choice for φ. Equation [5.61] is an implicit equation that has to be solved using a numerical method. In [PRO 14], Newton-Raphson's method has been used to find the zero of the function $F(d_{j,k}) \equiv d_{j,k} - d^0_{j,k} - w_j \frac{a_{j,k}}{d_{j,k}}$ by iteratively solving the equation

$$d^n_{j,k} = d^{n-1}_{j,k} - \frac{F(d^{n-1}_{j,k})}{F'(d^{n-1}_{j,k})}, \qquad [5.62]$$

$n \geq 1$. Since the solution is not expected to differ too much from the original magnitude $d^0_{j,k}$, Newton-Raphson's algorithm is initialized with $d^0_{j,k}$.

A standard result guarantees the convergence of Newton-Raphson's algorithm as long as the initial condition $d^0_{j,k}$ is sufficiently near the solution, $F'(d^0_{j,k})$ is small enough, $F''(d_{j,k})$ varies smoothly and the inverse of $F''(d_{j,k})$ is bounded near the solution (see, e.g., [CIA 89]). In particular, these conditions imply that we cannot take the weights w_j to be too big, otherwise Newton's algorithm can oscillate. In [PRO 13], it has been proved that if the identity function is substituted by the gamma function, then the stability of Newton-Raphson's algorithm in this setting is improved.

Note that since Newton-Raphson's method is initialized with the coefficients $d^0_{j,k}$, which are bounded from below, the solution of equation [5.61] belongs to an open neighborhood of $d^0_{j,k}$ and the numerical method converges to a positive solution of equation [5.61].

To stress the perceptual nature of the model, Figure 5.4 shows a scan line of the classical Mach bands picture: the wavelet algorithm is able to reproduce the well-known undershoots and overshoots typical of the HVS behavior recalled in Chapter 1.

In Figure 5.5, the action of the wavelet algorithm can be seen on three images affected by distinct problems: underexposure, color cast and overexposure. As can be seen, the wavelet algorithm is able to perform a radiometric adjustment of the non-optimally exposed pictures and to strongly reduce the color cast, as shown in Figure 5.6.

5.6. High-dynamic-range (HDR) imaging

Radiance in natural scenes can span several orders of magnitude, yet commercial cameras can capture only two orders of magnitude and reproduce

Low-Dynamic-Range (LDR) photographs, often affected by saturated areas and loss of contrast and detail. During the last fifteen years, many techniques have been studied and proposed in order to expand the dynamic range of digital photographs to create the so-called High-Dynamic-Range (HDR) images, i.e. matrices whose entries are proportional to the actual radiance of the scene. For a thorough overview of the HDR imaging, we refer the interested reader to [REI 05b].

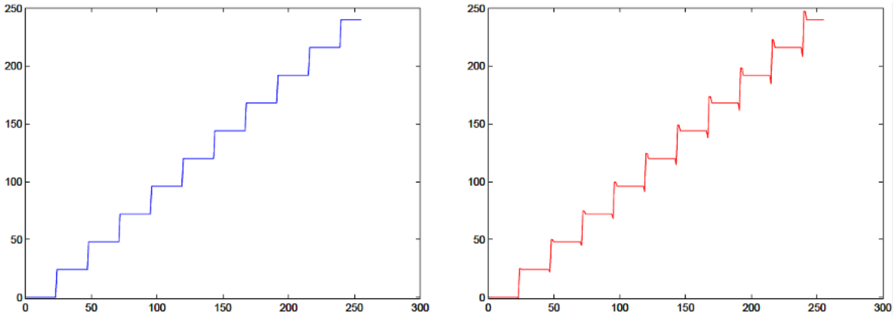

Figure 5.4. *From left to right: a scan line of the Mach bands image before and after the wavelet algorithm, respectively. The undershoot and overshoot effects are typical HVS features that the wavelet model is able to reproduce. The wavelet algorithm was applied with the following parameters: the mother wavelet is the biorthogonal wavelet with two vanishing moments; the computation is performed over the maximum number of scales allowed for each image,* $w_j = 0.5$, $T_j = \frac{\max_{k\in\Omega}\{d_{j,k}\}}{2.5}$ *for each scale, and* $\alpha = 0.1$

HDR images have been widely used to capture scene illumination, but also for a realistic scene representation. That is to say, the wider dynamic range of HDR images allows a better capture of details and color differences. This high precision is the reason why most photographers nowadays use cameras with a wider dynamic range than two orders of magnitude.

Two main problems remain to be solved in HDR imaging. First, while the technique proposed by Debevec and Malick [DEB 97] can be considered as the "*de facto* standard" for the creation of HDR images in *static conditions*, i.e. with perfectly still camera and without moving objects in the scene, no standard is available when these condition fail. Second, HDR images cannot be entirely displayed or printed on the majority of commercial screens or printers, hence a so-called *Tone Mapping* (TM) transformation is needed to properly reduce their range without losing details and respecting as much as possible the original color sensation. In what follows, we consider only the latter problem.

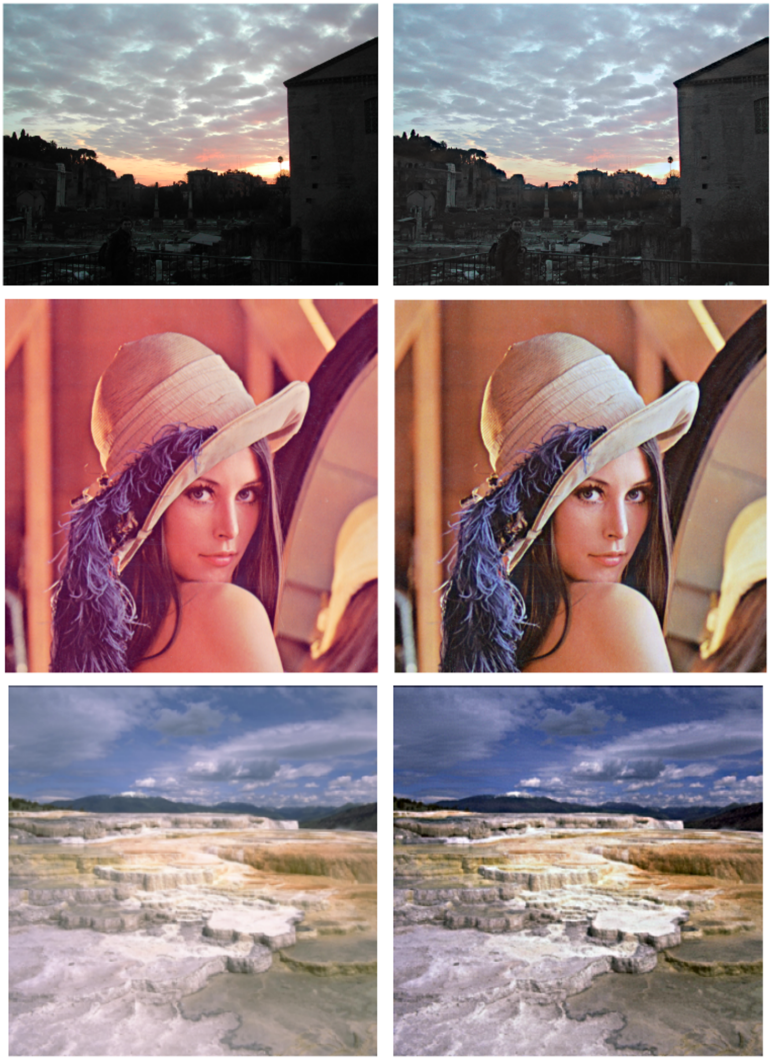

Figure 5.5. *Images on the left: original ones.* Images on the right*: enhanced versions after the wavelet algorithm: details appear in originally underexposed and overexposed areas, and the pink color cast in the “Lena” image is removed. The filtering parameters are the following: the mother wavelet is the Daubechies wavelet with two vanishing moments; the computation is performed over the maximum number of scales allowed for each image,* $w_j = 0.5$*, and* $T_j = \frac{\max_{k\in\Omega}\{d_{j,k}\}}{10}$ *for each scale* 2^j*. For a color version of the figure, see www.iste.co.uk/provenzi/color.zip*

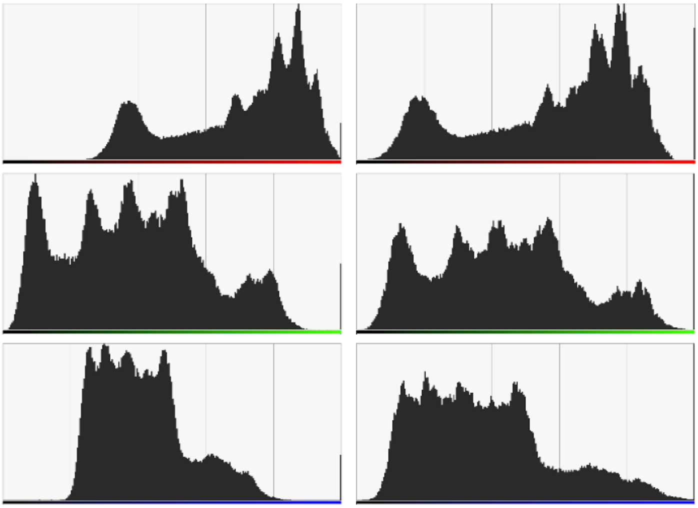

Figure 5.6. *Left column: original RGB histograms of the image in the second row of Figure 5.5. Right column: enhanced RGB histograms corresponding to the image in the second row of Figure 5.5. Again, note the histogram stretching without reaching a complete equalization, which would have been inappropriate. For a color version of the figure, see www.iste.co.uk/provenzi/color.zip*

Many tone mapping operators (TMOs) have been proposed in the literature; for a thorough review and analysis of the state of the art until 2005, we refer to [REI 05b]. Here, we just want to give a very brief overview of the different schools of thought that have been proposed so far. There is a category of perceptually based TMOs which can be either spatially global or local. The former are, in general, very fast and do not introduce halos or artifacts, but their contrast rendition tends to be poor. The first global TMOs used Stevens' law [3] to achieve range compression and were proposed by Tumblin and Rushmeier [TUM 93], Chiu *et al.* [CHI 93] and Ward *et al.* [WAR 97].

Schlick [SCH 94] proposed a rational function very close to the Michaelis-Menten formula [1.1], showing improvements with respect to Stevens' law [GON 02]. The global Michaelis-Menten formula has been exploited by Pattanaik et al. [PAT 00], Reinhard and Devlin [REI 05a], and more recently, by Kuang *et al.* [KUA 07]. More sophisticated vision models were also proposed, taking into account time adaptation such as Ferwerda's model [FER 96] or Weber-Fechner's law, e.g. the methods by Ward *et al.* [WAR 97] and Ashikhmin [ASH 02].

Reinhard *et al.* [REI 02] and Tamburrino *et al.* [TAM 08] introduced local TMOs that improved detail but created halos and artifacts next to edges. A TMO based on a modified version of the Retinex model of color vision was proposed by Jobson *et al.* [JOB 97a], and the anchoring theory 1 has been used by Krawczyk *et al.* [KRA 05] after a suitable subdivision of the original image into layers of similar luminance.

There is another category, that of gradient-based TMOs, which rely on the idea of shrinking large intensity gradients while preserving small fluctuations, corresponding to fine details. Tumblin and Turk [TUM 99] used a hierarchical method based on a Partial Differential Equation (PDE) inspired by anisotropic diffusion.

Durand and Dorsey [DUR 02] and Kuang *et al.* [KUA 07] obtained improved results by using techniques inspired by bilateral filtering. Fattal *et al.* [FAT 02] and Mantiuk *et al.* [MAN 06] proposed methods where spatially varying compression factors were used to implement suitable manipulations of the gradient field.

Here we describe the algorithm proposed in [FER 11], where the authors followed the TM philosophy proposed by Ward *et al.* [WAR 97], where the main purpose of TM is to emulate as much as possible the perception of contrast and color produced by the real-world scene. Lacking a perfect model of the Human Visual System (HVS), they concentrated on the HVS properties recalled in Chapter 1 to propose their TM operator.

While visual adaptation is considered as a retinal process, local contrast enhancement (and color constancy) is thought to involve also higher stages of the visual cortex (see, e.g., Hubel's book [HUB 95]). This suggests that the processes involved in these two phases are quite different; therefore, in [FER 11] the processes were implemented in two independent stages.

5.6.1. *A two-stage tone mapping*

Neuroscience experiments to measure visual adaptation have been performed using very simple, non-natural images: brief pulses of light with intensity $\mathcal{I}$ were superimposed on a uniform background.

As already recalled in Chapter 1, when a photoreceptor absorbs a photon, the electric potential of its membrane changes accordingly to the empirical law known as the Michaelis-Menten equation [1.1], which we replicate here for clarity:

$$r(\mathcal{I}) = \frac{\Delta V}{\Delta V_{\max}} = \frac{\mathcal{I}^{\gamma}}{\mathcal{I}^{\gamma} + \mathcal{I}_S^{\gamma}}, \qquad [5.63]$$

I_S is the light level at which the photoreceptor response is half maximal, called the semi-saturation level, and which is usually associated with the level of adaptation.

Each type of cone is most sensitive to a particular waveband; thus, the semi-saturation constant must depend on the amount of light in this same waveband that reaches it, not on the luminance of the light source, as pointed out by Boynton [BOY 02] and Wade and Wandell [WAD 02].

The change of electric potential ΔV is the photoreceptor's physiological response to $\mathcal{I}$, $V_{\max}$ is the highest difference of potential that can be generated and γ is constant, measured as 0.74 for the rhesus monkey [VAL 83]. This change in electric potential describes the light response of one single living photoreceptor isolated in a tiny glass pipette, which is different than the response of the cell embedded in the retina. In fact, adjacent photoreceptors strongly affect each other both chemically and electrically: none of the retina's approximately 125 million photoreceptor cells respond independently, and the brain receives no light meter-like signals from them. Instead, three layers of retinal neurons interconnect to construct 20 or more different kinds of signals that summarize local changes in retinal illumination.

Equation [1.1] has been used extensively in the TM literature, as mentioned in the previous section. Although not been explicitly stated, the underlying assumption here is that the output of equation [1.1], a ratio of voltage amplitudes of electrical responses (or the ratio of light intensities), which is a physical magnitude, is assumed to be correlated with the perceived brightness, which is a sensation, a perceptual magnitude. So, each TMO that uses [1.1], or its variations, takes an HDR input intensity and gives an LDR output, trying to mimic the perceived brightness.

On the side of perception of intensity changes, we have Weber-Fechner's law presented in Chapter 1, i.e. the logarithmic behavior of the sensation of light intensity: $s(\mathcal{I}) = s_0 + k\log(n + \mathcal{I})$. As pointed out in [REI 05b], this logarithmic transformation is probably the simplest procedure we might use as a TMO, and it works fairly well for medium-dynamic-range images. Nonetheless, this equation is questionable and still contested in the psychophysics community, where researchers disagree on the validity of accumulating and/or integrating JNDs to assess supra-threshold stimuli of any sort.

Now we have two equations, Michaelis-Menten's (MM) and Weber-Fechner's (WF), which are different but which are used (directly or with some modifications) under the assumption that they are both modeling the same thing, namely, the perceived brightness.

Let us examine this situation in more detail to understand how to solve this apparent contradiction. Michaelis-Menten (MM) and Weber-Fechner (WF) equations model mathematically the results of different experiments that measured different visual phenomena. WF describes detectable-difference thresholds for small, steady-state stimuli; users adapt to a steady, uniform background, and experiments measure the tiniest steady difference we can distinguish from that background. MM models electrical responses to flashed stimuli; it measures how well we can detect tiny differences in intensities far away from that of the adapting background (and measured before our adaptation level can change).

Since MM does not match with WF, we cannot claim that a TMO based on the NR equation accurately models perception in the HVS. However, the TM results obtained with these NR-like methods, based on modifications of the MM equation, are usually better than those obtained with the logarithmic mapping corresponding to WF: their overall appearance seems closer to our own perception.

To try to understand this fact, let us recall that TMOs map an arbitrarily large radiance range into image values in a limited range, without loss of generality we may assume that the output range is the interval $[0, 1]$. The values given by MM are already in this interval, but for WF, it is necessary to apply a normalization step to the output. The outputs of MM and WF are fairly similar for the first three or four orders of I, but then the output of MM tends to 1 while the output of WF increases indefinitely.

The fact that MM tends to 1 for high-radiance values is explained by the saturation property of photoreceptors: the activity of cones covers approximately four orders of magnitude around the semi-saturation value, as is explained by Valeton and van Norren [VAL 83], and for higher radiances the cones saturate.

The saturation of the cones is not considered in WF, and therefore the corresponding curve always increases. Taking all the above considerations into account, in [FER 11], the authors claimed that since cones are indeed saturating, in order to model the perceptual response, we must not use the curve obtained with steady stimuli fields because these fields do not cause saturation in the cones and we end up with the logarithmic curve, which increases indefinitely. Instead, we must use the curve obtained with pulsating fields. This complies with WF in an operative range of four orders of magnitude, but for higher radiances increase very steeply because the cones saturate at those radiance values.

Dunn *et al.* [DUN 07], while talking about visual adaptation and saccades, said the following: "retinal mechanisms [...] adjust sensitivity in the 200 ms intervals between saccades," and "As we make saccades to explore a visual scene, retinal neurons encounter a wide range of light intensities. Receptor and post-receptor adaptation permit the amplification required to see objects in shadows while avoiding saturation from the sky. The combination of these adaptive mechanisms allows the visual system to encode details in a scene with greater fidelity than a standard camera at a single exposure setting".

The implication would be that while viewing real-world scenes, as we frequently use saccadic movements to look for and track objects or simply to gather all of the details, the stimuli fields are not steady but pulsed. Hence, the curve that more accurately matches perception in real-world images would be the upper curve in Figure 5.7.

In short, Figure 5.7 shows an inflexion point at the radiance value located approximately two orders of magnitude above the semi-saturation radiance, which we will call I_M: for radiances below I_M, Weber-Fechner's law holds, so the perceptually valid tone mapping curve is the one given by WF; for radiances above I_M, the cones' responses start to saturate so the perceptually (and physiologically) valid tone mapping curve must have an horizontal asymptote, and for this, we can use the curve given by the MM.

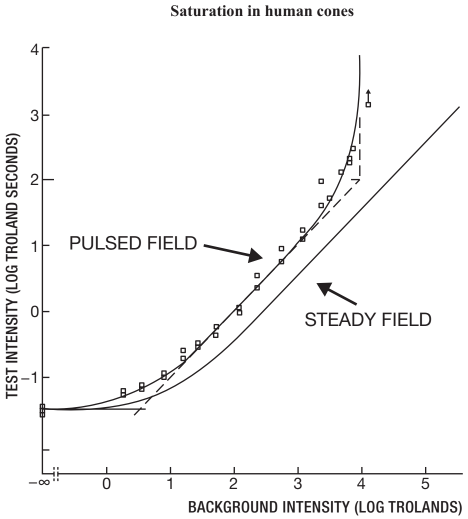

Figure 5.7. *Cones saturate when the stimuli field is not steady but pulsed: perceptual curves of cones for pulsed and steady stimuli (adapted from Shevell [SHE 77])*

With this information, we can now introduce the first stage of our algorithm. We propose to use a TM curve $C(\mathcal{I})$ which combines the curves MM and WF in the aforementioned way:

$$C(\mathcal{I}) = \begin{cases} s_0 + k\log(\mathcal{I} + n) & \text{if } \mathcal{I} \leq \mathcal{I}_M \\ \frac{\mathcal{I}^\gamma}{\mathcal{I}^\gamma + \mathcal{I}_S^\gamma} & \text{if } \mathcal{I} > \mathcal{I}_M \end{cases} \qquad [5.64]$$

where s_0 is chosen so as to ensure the continuity of c at the critical point $\mathcal{I}_M$. The output of c will be normalized, i.e. linearly scaled so that it spans the interval $[0, 1]$.

Figure 5.8 shows the TM results obtained using MM, WF and $C(\mathcal{I})$ on the same HDR image. The left-hand side image, obtained using MM, has an overall good contrast but the brightest regions appear overexposed (e.g. the areas near the windows or the trees); the middle image, obtained with the logarithmic mapping of WF, has overall poor contrast but the details of the brightest regions are not lost.

The right-hand side result is the one obtained with the *first stage* of the method just described, $C(\mathcal{I})$, and we see that it combines the best characteristics of the other two images, showing overall good contrast and little or no loss of detail in the brightest areas.

Figure 5.8. *Left: TM output using the Michaelis-Menten equation. Middle: TM output using a logarithmic mapping (Weber-Fechner's law). Right: TM output equation 5.64*

The *second stage* consists simply in the application of the perceptually inspired variational algorithm for color correction discussed in the previous sections, which is associated with higher stages of visual perception and will produce a local enhancement of the first stage, also allowing the reduction of a possible color cast due to a non-neutral illuminant in the photographed scene.

All the implementation details of the two-stage tone mapper and the comparison with the state-of-the-art TMOs are given in [FER 11]; here we just want to stress the fact that the proposed tone mapper has the best overall performance with respect to one of the most vastly used quality measures (see [AYD 08]).

Appendix

Rudimentals of Variational Principles

Calculus of variations is a generalization of ordinary calculus in $\mathbb{R}^n$. In the latter we deal with functions $f : D \subseteq \mathbb{R}^n \to \mathbb{R}^m$, n, m integers ≥ 1, while in variational calculus we work with functions acting on functional spaces.

More precisely, a functional space is a vector space whose elements are functions having some specified features. To give a concrete example let us consider two very well-known and useful functional spaces:

– $C^n(D)$, $D \subseteq \mathbb{R}^n$, D open, is the space of functions $f : D \to \mathbb{R}$ which are n-times differentiable, with continuous derivatives on the whole D, the case $n = 0$ corresponds simply to continuous functions on D;

– $L^2(\mathbb{R})$ is the space of square-integrable functions on $\mathbb{R}$, i.e. $f : \mathbb{R} \to \mathbb{R}$ such that $\int_{\mathbb{R}} f(x)^2 \, dx < +\infty$. These functions are also said to be finite-energy functions.

Given an abstract functional space $\mathcal{F}$ over the field $\mathbb{K}$ (in general $\mathbb{K} = \mathbb{R}$ or $\mathbb{C}$), the linear operations in $\mathcal{F}$ are defined point-wise, i.e. given $f, g \in \mathcal{F}$ and $\alpha, \beta \in \mathbb{K}$, the function $h \in \mathcal{F}$ defined by the linear combination $h = \alpha f + \beta g \in \mathcal{F}$ acts as follows on the arguments x of f and g: $h(x) = \alpha f(x) + \beta g(x)$.

A functional φ acting on the abstract functional space $\mathcal{F}$ is a linear form over $\mathcal{F}$, i.e. a linear function from $\mathcal{F}$ to the field $\mathbb{K}$:

$$\begin{aligned} \varphi : \mathcal{F} &\longrightarrow \mathbb{K} \\ f &\longmapsto \varphi(f). \end{aligned}$$

Computational Color Science: Variational Retinex-like Methods, First Edition. Edoardo Provenzi.

Let us also recall that, in ordinary calculus, a great deal of effort is dedicated to finding the extrema of functions. To fix ideas, let us consider a function $f \in C^n(D)$, $\vec{x} \in D$, then:

– we call $\underline{\vec{x}} = \underset{D}{\operatorname{argmin}} f$, if $f\left(\underline{\vec{x}}\right) = \min\limits_{\vec{x} \in D} f(\vec{x})$;

– we call $\overline{\vec{x}} = \underset{D}{\operatorname{argmax}} f$, if $f\left(\overline{\vec{x}}\right) = \max\limits_{\vec{x} \in D} f(\vec{x})$.

We recall that, given a function $f : D \subseteq \mathbb{R}^n \to \mathbb{R}$, $f \in C^n(D)$ and any unit vector $\vec{v} \in D$, the *directional derivative* of f along $\vec{v}$, calculated in $\vec{x}$, is defined by:

$$D_{\vec{v}} f(\vec{x}) = \lim_{\varepsilon \to 0} \frac{f(\vec{x} + \varepsilon \vec{v}) - f(\vec{x})}{\varepsilon}, \qquad \text{[A.1]}$$

the partial derivatives $\partial_i f(x)$, $i = 1, \dots, n$, of f are simply the n directional derivatives computed by choosing $\vec{v} = \vec{e}_i$, the i-th unit vectors of the canonical basis of $\mathbb{R}^n$. Finally, the gradient $\vec{\nabla} f(x)$ is the n-dimensional vector whose components are the partial derivatives of f in x.

By virtue of Fermat's interior extrema theorem, the gradient of f (and its directional derivatives in every direction) must be null when computed in the argmin or argmax of f. This necessary condition becomes also sufficient when D and the function f are convex.

The computation, analytical or approximated, of the extrema of a function $f \in C^n(D)$ belongs to a field called *optimization in* $\mathbb{R}^n$.

Contrary to ordinary calculus, in variational calculus *the argmin and argmax of a functional are functions*, more precisely, for an arbitrary functional $E : \mathcal{F} \to \mathbb{K}$:

– we call $\underline{f} = \underset{\mathcal{F}}{\operatorname{argmin}} E$, if $E\left(\underline{f}\right) = \min\limits_{f \in \mathcal{F}} E(f)$;

– we call $\overline{f} = \underset{\mathcal{F}}{\operatorname{argmax}} E$, if $E\left(\overline{f}\right) = \max\limits_{f \in \mathcal{F}} E(f)$.

The possibility to pass from *extrema of functions* represented by points of $\mathbb{R}^n$ to *extrema of functionals* represented by functions allows us to examine, in variational calculus, much more general problems than in ordinary calculus. Of course, this comes at the expense of a greater mathematical difficulty.

The computation, analytical and, most of the time, approximated, of the extrema of a functional E is called *variational* (or *functional*) *optimization* and it has been the subject of research by many mathematicians, physicists and engineers in the past two centuries [BOY 04, HIR 12]. In the following, we will give the reason for the name "optimization".

A basic tool in variational optimization is the concept of *first variation* of a functional, which is a direct generalization of the directional derivative of a function. More precisely, given a functional $E : \mathcal{F} \to \mathbb{R}$ and any function $g \in \mathcal{F}$, called *perturbation*, the first variation (or Gâteaux derivative) of E along g, calculated in f, is defined by

$$\delta E(f, g) = \lim_{\varepsilon \to 0} \frac{E(f + \varepsilon g) - E(f)}{\varepsilon}, \qquad [A.2]$$

here the perturbation g plays the role of the vector $\vec{v}$ in the definition of directional derivative.

The generalization of Fermat's interior extrema theorem to variational calculus states that the first variation of a functional computed in any extreme (argmin or argmax) must be null for every perturbation. Moreover, this necessary condition becomes also sufficient under suitable convexity hypotheses or when it is associated to some properties of the second variation, i.e. the first variation of the first variation interpreted as a functional.

The equations

$$\delta E(f, g) = 0 \qquad \forall g \in \mathcal{F}, \qquad [A.3]$$

are called *Euler-Lagrange equations*.

For a better comprehension of the variational framework of Chapters 4 and 5, it is worthwhile to complete this overview by showing explicit examples of functionals given by one or two terms and by explaining why the search of their extrema is called optimization.

Let us start with the problem of finding the extremal function $y = f(x)$ whose graph gives the shortest curve that connects two points (x_1, y_1) and

(x_2, y_2) in $\mathbb{R}^2$. To find the variational principle associated to this problem, let us recall that the arc length A of the curve represented by the graph of a differentiable function $y = f(x)$ between the points $(x_1, y_1 \equiv f(x_1))$ and $(x_2, y_2 \equiv f(x_2))$ is given by the integral $\int_{x_1}^{x_2} \sqrt{1 + [y'(x)]^2}\, dx$. The solution to our problem will therefore be the argmin of the functional

$$\begin{aligned} A : C([x_1, x_2]) &\longrightarrow \mathbb{R} \\ f \quad &\longmapsto A(f) = \int_{x_1}^{x_2} \sqrt{1 + [f'(x)]^2}\, dx. \end{aligned}$$

It can be easily proven that, as expected, the argmin of $A(f)$ is given by the straight line function $\underline{f}(x) = mx + b$, where $m = (y_2 - y_1)/(x_2 - x_1)$ and $b = (x_2y_1 - x_1y_2)/(x_2 - x_1)$.

In this case, it is very easy to understand why the argmin of $A(f)$ represents the optimal solution to the problem of finding the shortest curve, because of the *direct interpretation* of $A(f)$ as the arc length functional.

It is more difficult to understand what optimality means when the functional associated to a problem is given by two or more terms. To help understand this, let us consider the problem of determining, with a variational principle, the trajectory of a particle moving into space between time t_0 and time t_1 in a conservative physical system[1].

The Italian-French mathematician and physicist Lagrange solved this problem by considering the following functional, that nowadays we call *Lagrangian* in his honor:

$$L(\vec{q}) = \int_{t_0}^{t_1} \mathcal{L}(\vec{q}(t))\, dt \qquad \text{[A.4]}$$

where $\mathcal{L}(\vec{q}) = T(\vec{q}) - V(\vec{q})$, $\vec{q} : [t_0, t_1] \to \mathbb{R}^3$ being the time-dependent position function of a moving particle in $\mathbb{R}^3$ and T, V being the kinetic and the potential energy functions of the physical system, respectively.

The outstanding achievement of Lagrange is that the argmin of the functional in [A.4] is the function $\underline{\vec{q}}(t)$ which solves Newton's equation of

---

[1] A physical system is called conservative if the forces acting on it can be expressed as minus the gradient of a potential energy function V.

motion $\vec{F}(t) = m\ddot{\vec{q}}(t)$, $\forall t \in [t_0, t_1]$, where $\vec{F}$ is the resultant of forces acting on the particle and $\ddot{\vec{q}}(t)$ is the second temporal derivative of $\vec{q}$, i.e. its acceleration. Since it is well known that the trajectory of a particle in a (non-relativistic) physical system satisfies Newton's second law of dynamics, Lagrange proved that this is equivalent to searching for the argmin of the functional [A.4].

In other words, the minimization of functional [A.4] gives the optimal result because it coincides with the solution of Newton's second law of dynamics. Since $\mathcal{L}(\vec{q}(t))$, the integrand function of [A.4], is given by two terms with opposite sign, i.e. the kinetic energy $T(\vec{q}(t)) = \frac{1}{2}m\|\dot{\vec{q}}(t)\|^2$ and the potential energy $V(\vec{q}(t))$, we can interpret Lagrange's result by saying that, in every instant $t \in [t_0, t_1]$, the particle moves along a trajectory which minimizes the difference between the energy that the particle actually has due to its motion (i.e. T) and the energy that the particle could potentially attain (i.e. V). This interpretation is commonly summarized by saying that the trajectory of motion of a particle is given by the *optimal balance* between its kinetic and potential energy in every instant. The balance between them is always present, but it is optimal to describe the trajectory of motion only for the argmin of the functional [A.4].

Of course, when we deal with another problem, not necessarily related to motion of particles or length of curves, optimality will refer, more generally, to the match between the argmin of the functional with an empirical or theoretical law describing a phenomenon or a property. Consistent with the nomenclature just recalled, also in those cases we will say that the argmin is characterized by the optimal balance between the functional terms.

An illuminating example in this sense is the very deep variational interpretation of histogram equalization of digital images provided in [SAP 97], that is discussed in Chapter 4. There it is shown that a digital image with an equalized histogram[2] can be interpreted as the argmin of a functional characterized by the difference between a functional term which describes adjustment to the middle gray-level of the image and another one which gives a global measure of contrast carried by the image. Coherently with the considerations above, we will say that histogram equalization is given by the

---

[2] We recall that the intensity of a digital image is quantized and bounded in the set of values $\{0, 1, \ldots, 255\}$. A digital image is said to be equalized if each intensity level has the same occurrence probability in the image.

optimal balance between control of the dispersion around the middle gray and contrast intensification.

The possibility to arrive at these highly non-intuitive interpretations of known phenomena and also to predict new ones is what makes the use of variational calculus so prevalent among many different disciplines as a sort of unifying principle. This is one the main reasons why, in this book, we analyze the possibility of using variational principles as a bridge between the description of perceptual and non-physical judgments.

REMARK A.1.– Optimization of functionals is conventionally associated with the search of their minima. Of course, a minimization problem can be transformed into a maximization one simply by changing the sign of the functional under analysis.

REMARK A.2.– When parameters are involved in the definition of a functional, the interpretation of optimality can be a little more difficult. In fact, functional minimization in this case generates a whole family of optimal solutions that depend on the selection of the parameters appearing in the equations. In these cases, a suitable tuning procedure that may vary from case to case, must be used to set the parameters once and for all, thus providing the (only) optimal solution to the problem under consideration.

Bibliography

[AMB 05] Ambrosio L., Gigli N., Savaré G., *Gradient Flows in Metric Spaces and in the Space of Probability Measures*, Birkhauser, 2005.

[ASH 02] Ashikhmin M., "A tone mapping algorithm for high contrast images", in Debevec P., Gibson S. (eds), *Eurographics Workshop on Rendering*, 2002.

[AYD 08] Aydin T., Mantiuk R., Myszkowski K. *et al.*, "Dynamic range independent image quality assessment", *ACM SIGGRAPH 2008 Papers*, pp. 1–10, 2008.

[BAN 13] Banić N., Lončarić S., "Light random sprays retinex: exploiting the noisy illumination estimation", *IEEE Signal Processing Letters*, vol. 20, pp. 1240–1243, 2013.

[BAN 15] Banić N., Lončarić S., "Smart light random memory sprays retinex: a fast retinex implementation for high-quality brightness adjustment and color correction", *Journal of the Optical Society of America A*, vol. 32, no. 11, pp. 2136–2147, 2015.

[BAR 02] Barnard K., Cardei V., Funt B., "A comparison of computational color constancy algorithms, part II: Experiments with image data", *IEEE Transactions on Image Proc.*, vol. 11, no. 9, pp. 985–996, 2002.

[BER 07] Bertalmío M., Caselles V., Provenzi E. *et al.*, "Perceptual color correction through variational techniques", *IEEE Transactions on Image Processing*, vol. 16, pp. 1058–1072, 2007.

[BER 09] Bertalmío M., Caselles V., Provenzi E., "Issues about the retinex theory and contrast enhancement", *International Journal of Computer Vision*, vol. 83, pp. 101–119, 2009.

[BLA 85] Blake A., "Boundary conditions of lightness computation in Mondrian world", *Computer Vision, Graphics and Image Processing*, vol. 32, pp. 314–327, 1985.

[BOY 02] Boynton G., "Color vision: how the cortex represents color", *Current Biology*, vol. 12, pp. R838–R840, 2002.

[BOY 04] Boyd S., Vandendergh L., *Convex Optimization*, Cambridge University Press, 2004.

Computational Color Science: Variational Retinex-like Methods, First Edition. Edoardo Provenzi.

[BRA 86] BRAINARD D., WANDELL B., "Analysis of the retinex theory of color vision", *Journal of the Optical Society of America A*, vol. 3, no. 10, pp. 1651–1661, 1986.

[BUC 80] BUCHSBAUM G., "A spatial processor model for object colour perception", *Journal of the Franklin Institute*, vol. 310, pp. 337–350, 1980.

[CHI 93] CHIU K., HERF M., SHIRLEY P. *et al.*, "Spatially nonuniform scaling functions for high contrast images", *Proceedings of Graphics Interface 93*, pp. 245–253, 1993.

[CIA 89] CIARLET P., MIARA B., THOMAS J.-M., *Introduction to Numerical Linear Algebra and Optimisation*, Cambridge University Press, 1989.

[COO 04] COOPER T.J., BAQAI F.A., "Analysis and extensions of the Frankle-McCann Retinex algorithm", *Journal of Electronic Imaging*, vol. 13, pp. 85–92, 2004.

[CRE 87] CREUTZFELD O., LANGE-MALECKI B., WORTMANN K., "Darkness induction, retinex and cooperative mechanisms in vision", *Experimental Brain Research*, vol. 67, pp. 270–283, 1987.

[CRE 90] CREUTZFELD O., LANGE-MALECKI B., DREYER E., "Darkness induction, retinex and cooperative mechanisms in vision", *Journal of the Optical Society of America A*, vol. 7, pp. 1644–1653, 1990.

[DEB 97] DEBEVEC P., MALIK J., "Recovering high dynamic range radiance maps from photographs", *Proceedings of the 24th Annual Conference on Computer Graphics*, pp. 369–378, 1997.

[DUN 07] DUNN F., LANKHEET M., RIEKE F., "Light adaptation in cone vision involves switching between receptor and post-receptor sites", *Nature*, vol. 449, pp. 603–606, 2007.

[DUR 02] DURAND F., DORSEY J., "Fast bilateral filtering for the display of high-dynamic-range images", *SIGGRAPH 2002, Proceedings of the 29th Annual Conference on Computer Graphics and Interactive Techniques*, pp. 257–266, 2002.

[EBN 07] EBNER M., *Color Constancy*, Wiley, 2007.

[FAI 05] FAIRCHILD M., *Color Appearance Models*, Wiley, 2005.

[FAT 02] FATTAL R., LISCHINSKI D., WERMAN M., "Gradient domain high dynamic range compression", *ACM Transactions on Graphics*, vol. 21, no. 3, pp. 249–256, 2002.

[FER 96] FERWERDA J., PATTANAIK S., SHIRLEY P. *et al.*, "A model of visual adaptation for realistic image synthesis", *Proceedings of SIGGRAPH 96: Computer Graphics Proceedings*, pp. 249–258, 1996.

[FER 11] FERRADANS S., BERTALMÍO M., PROVENZI E. *et al.*, "An analysis of visual adaptation and contrast perception for tone mapping", *IEEE Transactions on Pattern Analysis and Machine Intelligence*, vol. 33, no. 10, pp. 2002–2012, 2011.

[FER 15] FERRADANS S., PALMA-AMESTOY R., PROVENZI E., "An algorithmic analysis of variational models for perceptual local contrast enhancement", *Image Processing On Line*, vol. 5, no. 10, pp. 219–233, 2015.

[FIN 04] FINLAYSON G., TREZZI E., "Shades of gray and color constancy", *Proc. of the Twelfth Color Imaging ConferenceIS&T/SID*, pp. 37–41, 2004.

[FRA 83] Frankle J., McCann J.J., Method and apparatus for lightness imaging, US Patent US 4,348,336, 1983.

[FUN 04] Funt B., Ciurea F., McCann J.J., "Retinex in MATLAB", *Journal of Electronic Imaging*, vol. 13, no. 1, pp. 48–57, 2004.

[FUN 10] Funt B., Lilong S., "The Rehabilitation of Max-RGB", *Proceedings 18th IS&T Color Imaging Conference, San Antonio, USA*, 2010.

[GET 12] Getreuer P., "Automatic color enhancement (ACE) and its fast implementation", *Image Processing On Line*, vol. 2, pp. 266–277, 2012.

[GEV 12] Gevers T., Gijsenij A., van de Weijer J. *et al.*, *Color in Computer Vision, Fundamentals and Applications*, Wiley, 2012.

[GIA 14] Gianini G., Manenti A., Rizzi A., "QBRIX: a quantile-based approach to retinex", *Journal of the Optical Society of America A*, vol. 31, no. 12, pp. 2663–2673, 2014.

[GIJ 07] Gijsenij A., Gevers T., "Color Constancy by Local Averaging", pp. 171–174, 2007.

[GIJ 11] Gijsenij A., Gevers T., van de Weijer J., "Computational color constancy: survey and experiments", *IEEE Transactions on Image Processing*, vol. 20, no. 9, pp. 2475–2489, 2011.

[GON 02] Gonzales R., Woods R., *Digital Image Processing*, Prentice Hall, 2002.

[GRO 16] Gronchi G., Provenzi E., "A variational model for context-driven effects in perception and cognition", *Journal of Mathematical Psychology*, 2016.

[HIR 12] Hiriart-Urruty J., Lemaréchal C., *Fundamentals of Convex Analysis*, Springer Science & Business Media, 2012.

[HOR 74] Horn B., "Determining lightness from an image", *Computer Graphics and Image Processing*, vol. 3, pp. 277–299, 1974.

[HUB 95] Hubel D., *Eye, Brain, and Vision*, Scientific American Library, 1995.

[HUN 14] Hunt R., Pointer M., *Measuring Colour*, Wiley, 2014.

[HUR 86] Hurlbert A., "Formal connections between lightness algorithms", *Journal of the Optical Society of America A*, vol. 3, pp. 1684–1693, 1986.

[HUR 90] Hurvich L., Jameson D., "Theory of brightness and color contrast in human vision", *Vision Research*, vol. 4, pp. 135–154, 1990.

[JIA 13] Jiang J., Liu D., Gu J. *et al.*, "What is the space of spectral sensitivity functions for digital color cameras?", *WACV, IEEE Workshop on the Applications of Computer Vision*, pp. 168–179, 2013.

[JOB 97a] Jobson D., Rahman Z., Woodell G., "A multiscale retinex for bridging the gap between color images and the human observation of scenes", *IEEE Transactions on Image Processing*, vol. 6, no. 7, pp. 965–976, 1997.

[JOB 97b] Jobson D., Rahman Z., Woodell G., "Properties and performance of a center/surround retinex", *IEEE Transactions on Image Processing*, vol. 6, no. 3, pp. 451–462, 1997.

[KIM 03] Kimmel R., Elad M., Shaked D. *et al.*, "A variational framework for retinex", *International Journal of Computer Vision*, vol. 52, pp. 7–23, 2003.

[KOL 95] Kolb H., Fernandez E., Nelson R., *Webvision: The Organization of the Retina and Visual System*, University of Utah Health Sciences Center, 1995.

[KOL 11] Kolås Ø., Farup I., Rizzi A., "Spatio-temporal retinex-inspired envelope with stochastic sampling: a framework for spatial color algorithms", *Journal of Imaging Science and Technology*, vol. 55, no. 4, pp. 40503–40501, Society for Imaging Science and Technology, 2011.

[KRA 05] Krawczyk G., Myszkowski K., Seidel H., "Lightness perception in tone reproduction for high dynamic range images", Eurographics, 2005.

[KRI 02] von Kries J., "Chromatic Adaptation", *Festschrift der Albrecht-Ludwigs-Universität*, pp. 145–158, 1902.

[KUA 07] Kuang J., Johnson G., Fairchild M., "iCAM06: a refined image appearance model for HDR image rendering", *Journal of Visual Communication and Image Representation*, vol. 18, pp. 406–414, 2007.

[LAN 64] Land E., "The retinex", *American Scientist*, vol. 52, no. 2, pp. 247–264, 1964.

[LAN 71] Land E., McCann J., "Lightness and retinex theory", *Journal of the Optical Society of America*, vol. 61, no. 1, pp. 1–11, 1971.

[LAN 77] Land E., "The retinex theory of color vision", *Scientific American*, vol. 237, pp. 108–128, 1977.

[LAN 83] Land E., "Recent advances in retinex theory and some implications for cortical computations: color vision and the natural image", *Proceedings of the National Academy of Sciences of the United States of America*, vol. 80, pp. 5163–5169, 1983.

[LAN 86] Land E., "An alternative technique for the computation of the designator in the retinex theory of color vision", *Proceedings of the National Academy of Sciences of the United States of America*, vol. 83, pp. 3078–3080, 1986.

[LEC 16] Lecca M., Rizzi A., Gianini G., "Energy-driven path search for termite retinex", *Journal of the Optical Society of America A*, vol. 33, no. 1, pp. 31–39, 2016.

[MAL 99] Mallat S., *A Wavelet Tour of Signal Processing*, 3rd ed., Academic Press, 1999.

[MAN 06] Mantiuk R., Myszkowski K., Seidel H., "A perceptual framework for contrast processing of high dynamic range images", *ACM Transactions on Applied Perception (TAP)*, vol. 3, no. 3, pp. 286–308, 2006.

[MAR 00] Marini D., Rizzi A., "A computational approach to color adaptation effects", *Image and Vision Computing*, vol. 18, pp. 1005–1014, 2000.

[MCC 70] McCann J., Land E., Tatnall S., "A technique for comparing human visual responses with a mathematical model for lightness", *Optometry & Vision Science*, vol. 47, no. 11, pp. 845–855, LWW, 1970.

[MCC 11] McCann J., Rizzi A., *The Art and Science of HDR Imaging*, vol. 26, John Wiley & Sons, 2011.

[MIC 27] Michelson A., *Studies in Optics*, Chicago University Press, 1927.

[MOR 10] Morel J., Petro A., Sbert C., "A PDE formalization of retinex theory", *IEEE Transactions on Image Processing*, vol. 19, no. 11, pp. 2825–2837, 2010.

[NIK 14] Nikolova M., Steidl G., "Fast hue and range preserving histogram specification: theory and new algorithms for color image enhancement", *IEEE Transactions on Image Processing*, vol. 23, no. 9, pp. 4087–4100, 2014.

[PAL 09] Palma-Amestoy R., Provenzi E., Bertalmío M. *et al.*, "A perceptually inspired variational framework for color enhancement", *IEEE Transactions on Pattern Analysis and Machine Intelligence*, vol. 31, no. 3, pp. 458–474, 2009.

[PAT 00] Pattanaik S., Tumblin J., Yee H. *et al.*, "Time-dependent visual adaptation for fast realistic image display", *Proceedings of SIGGRAPH*, pp. 47–54, 2000.

[PÉR 03] Pérez P., Gangnet M., Blake A., "Poisson image editing", *ACM SIGGRAPH 2003 Papers*, pp. 313–318, 2003.

[PIE 16] Pierre F., Aujol J., Bugeau A. *et al.*, "Variational contrast enhancement of gray-scale and RGB images", *Journal of Mathematical Imaging and Vision*, pp. 1–18, 2016.

[POL 00] Polesel A., Ramponi G., Mathews V., "Image enhancement via adaptive unsharp masking", *IEEE Transactions on Signal Processing*, vol. 9, no. 3, pp. 505–510, 2000.

[PRO 05] Provenzi E., De Carli L., Rizzi A. *et al.*, "Mathematical definition and analysis of the retinex algorithm", *Journal of the Optical Society of America A*, vol. 22, no. 12, pp. 2613–2621, 2005.

[PRO 07] Provenzi E., Fierro M., Rizzi A. *et al.*, "Random spray retinex: a new retinex implementation to investigate the local properties of the model", *IEEE Transactions on Image Processing*, vol. 16, pp. 162–171, January 2007.

[PRO 08] Provenzi E., Gatta C., Fierro M. *et al.*, "A spatially variant white patch and gray world method for color image enhancement driven by local contrast", *IEEE Transactions on Pattern Analysis and Machine Intelligence*, vol. 30, pp. 1757–1770, 2008.

[PRO 13] Provenzi E., "Boosting the stability of wavelet-based contrast enhancement of color images through gamma transformations", *Journal of Modern Optics*, vol. 60, pp. 1145–1150, 2013.

[PRO 14] Provenzi E., Caselles V., "A wavelet perspective on variational perceptually-inspired color enhancement", *International Journal of Computer Vision*, vol. 106, pp. 153–171, 2014.

[REI 02] Reinhard E., Stark M., Shirley P. *et al.*, "Photographic tone reproduction for digital images", *ACM Transactions on Graphics*, vol. 21, pp. 267–276, 2002.

[REI 05a] Reinhard E., Devlin K., "Dynamic range reduction inspired by photoreceptor physiology", *IEEE Transactions on Visualization and Computer Graphics*, vol. 11, no. 1, pp. 13–24, 2005.

[REI 05b] Reinhard E., Ward G., Pattanaik S. *et al.*, *High Dynamic Range Imaging: Acquisition, Display, and Image-Based Lighting*, Morgan Kaufmann, 2005.

[RIZ 03] Rizzi A., Gatta C., Marini D., "A new algorithm for unsupervised global and local color correction", *Pattern Recognition Letters*, vol. 24, pp. 1663–1677, 2003.

[RUD 04] RUDD M., ZEMACH I., “Quantitive properties of achromatic color induction: an edge integration analysis”, *Vision Research*, vol. 44, pp. 971–981, 2004.

[SAP 97] SAPIRO G., CASELLES V., “Histogram modification via differential equations”, *Journal of Differential Equations*, vol. 135, pp. 238–266, 1997.

[SCH 94] SCHLICK C., “Quantization techniques for visualization of high dynamic range pictures”, *Proceedings of the 5th Eurographics Workshop on Rendering Workshop*, Springer-Verlag, pp. 7–20, 1994.

[SHA 84] SHAPLEY R., ENROTH-CUGELL C., “Chapter 9 visual adaptation and retinal gain controls”, *Progress in Retinal Research*, vol. 3, pp. 263–346, 1984.

[SHA 85] SHAFER S., “Using Color to Separate Reflection Component”, *Color. Res. App.*, vol. 10, no. 4, pp. 210–218, 1985.

[SHE 77] SHEVELL S., “Saturation in human cones”, *Vision Research*, vol. 17, pp. 427–434, 1977.

[SIM 12] SIMONE G., FARUP I., “Spatio-temporal retinex-like envelope with total variation”, *Conference on Colour in Graphics, Imaging, and Vision*, vol. 2012, Society for Imaging Science and Technology, pp. 176–181, 2012.

[SIM 14] SIMONE G., AUDINO G., FARUP I. *et al.*, “Termite retinex: a new implementation based on a colony of intelligent agents”, *Journal of Electronic Imaging*, vol. 23, no. 1, pp. 013006–013006, International Society for Optics and Photonics, 2014.

[STR 96] STRANG G., NGUYEN T., *Wavelets and Filter Banks*, Wellesley-Cambridge Press, 1996.

[TAM 08] TAMBURRINO D., ALLEYSSON D., MEYLAN L. *et al.*, “Digital camera workflow for high dynamic range images using a model of retinal processing”, *Proceedings of SPIE*, vol. 6817, 2008.

[TUM 93] TUMBLIN J., RUSHMEIER H., “Tone reproduction for realistic images”, *IEEE Computer Graphics and Applications*, vol. 13, no. 6, pp. 42–48, 1993.

[TUM 99] TUMBLIN J., TURK G., “LCIS: a boundary hierarchy for detail-preserving contrast reduction”, *SIGGRAPH: Conference Proceedings*, pp. 83–90, 1999.

[VAL 83] VALETON J., VAN NORREN D., “Light adaptation of primate cones: an analysis based on extracellular data”, *Vision Research*, vol. 23, pp. 1539–1547, 1983.

[VON 02] VON KRIES J., “Chromatic adaptation”, *Festschrift der Albrecht-Ludwigs-Universität*, pp. 145–158, 1902.

[WAD 02] WADE A., WANDELL B., “Chromatic light adaptation measured using functional magnetic resonance imaging”, *Journal of Neuroscience*, vol. 22, pp. 8148–8157, 2002.

[WAL 48] WALLACH H., “Brightness constancy and the nature of achromatic colors”, *Journal of Experimental Psychology*, vol. 38, no. 3, pp. 310–324, 1948.

[WAL 63] WALLACH H., “The perception of neutral colors”, *Scientific American*, vol. 208, pp. 107–116, 1963.

[WAR 97] WARD G., RUSHMEIER H., PIATKO C., “A visibility matching tone reproduction operator for high dynamic range scenes”, *IEEE Transactions on Visualization and Computer Graphics*, vol. 3, pp. 291–306, 1997.

[WEI 06] van de Weijer J., Gevers T., Bagdanov A., “Boosting color saliency in image feature detection”, *IEEE Trans. on Pattern Analysis and Machine Intelligence*, vol. 28, no. 1, pp. 150–156, 2006.

[WEI 07] van de Weijer J., Gevers T., Gijsenij A., “Edge-Based Color Constancy”, *IEEE Trans. on Image Proc.*, vol. 16, no. 9, pp. 2207–2214, 2007.

[WYS 82] Wyszecky G., Stiles W.S., *Color Science: Concepts and Methods, Quantitative Data and Formulas*, John Wiley & Sons, 1982.

[ZAI 99] Zaidi Q., *Color and Brightness Induction: From Mach Bands to Three-dimensional Configurations*, Cambridge University Press, New York, 1999.

[ZEK 93] Zeki S., *Vision of the Brain*, Blackwell, 1993.

[ZOS 15] Zosso D., Tran G., Osher S., “Non-local retinex–a unifying framework and beyond”, *SIAM Journal on Imaging Sciences*, vol. 8, no. 2, pp. 787–826, 2015.

Index

Computational Color Science: Variational Retinex-like Methods, First Edition. Edoardo Provenzi.

Other titles from

ISTE

in

Digital Signal and Image Processing

2017

CESCHI Roger, GAUTIER Jean-Luc
Fourier Analysis

CHARBIT Maurice
Digital Signal Processing with Python Programming

FEMMAM Smain
Fundamentals of Signals and Control Systems
Signals and Control Systems: Application for Home Health Monitoring

MAÎTRE Henri
From Photon to Pixel – 2nd edition

2015

BLANCHET Gérard, CHARBIT Maurice
Digital Signal and Image Processing using MATLAB®
Volume 2 – Advances and Applications:The Deterministic Case – 2nd edition
Volume 3 – Advances and Applications: The Stochastic Case – 2nd edition

CLARYSSE Patrick, FRIBOULET Denis
Multi-modality Cardiac Imaging

GIOVANNELLI Jean-François, IDIER Jérôme
Regularization and Bayesian Methods for Inverse Problems in Signal and Image Processing

2014

AUGER François
Signal Processing with Free Software: Practical Experiments

BLANCHET Gérard, CHARBIT Maurice
Digital Signal and Image Processing using MATLAB®
Volume 1 – Fundamentals – 2nd edition

DUBUISSON Séverine
Tracking with Particle Filter for High-dimensional Observation and State Spaces

ELL Todd A., LE BIHAN Nicolas, SANGWINE Stephen J.
Quaternion Fourier Transforms for Signal and Image Processing

FANET Hervé
Medical Imaging Based on Magnetic Fields and Ultrasounds

MOUKADEM Ali, OULD Abdeslam Djaffar, DIETERLEN Alain
Time-Frequency Domain for Segmentation and Classification of Non-stationary Signals: The Stockwell Transform Applied on Bio-signals and Electric Signals

NDAGIJIMANA Fabien
Signal Integrity: From High Speed to Radiofrequency Applications

PINOLI Jean-Charles
Mathematical Foundations of Image Processing and Analysis
Volumes 1 and 2

TUPIN Florence, INGLADA Jordi, NICOLAS Jean-Marie
Remote Sensing Imagery

VLADEANU Calin, EL ASSAD Safwan
Nonlinear Digital Encoders for Data Communications

2013

GOVAERT Gérard, NADIF Mohamed
Co-Clustering

DAROLLES Serge, DUVAUT Patrick, JAY Emmanuelle
Multi-factor Models and Signal Processing Techniques: Application to Quantitative Finance

LUCAS Laurent, LOSCOS Céline, REMION Yannick
3D Video: From Capture to Diffusion

MOREAU Eric, ADALI Tulay
Blind Identification and Separation of Complex-valued Signals

PERRIN Vincent
MRI Techniques

WAGNER Kevin, DOROSLOVACKI Milos
Proportionate-type Normalized Least Mean Square Algorithms

FERNANDEZ Christine, MACAIRE Ludovic, ROBERT-INACIO Frédérique
Digital Color Imaging

FERNANDEZ Christine, MACAIRE Ludovic, ROBERT-INACIO Frédérique
Digital Color: Acquisition, Perception, Coding and Rendering

NAIT-ALI Amine, FOURNIER Régis
Signal and Image Processing for Biometrics

OUAHABI Abdeljalil
Signal and Image Multiresolution Analysis

2011

CASTANIÉ Francis
Digital Spectral Analysis: Parametric, Non-parametric and Advanced Methods

DESCOMBES Xavier
Stochastic Geometry for Image Analysis

FANET Hervé
Photon-based Medical Imagery

MOREAU Nicolas
Tools for Signal Compression

2010

NAJMAN Laurent, TALBOT Hugues
Mathematical Morphology

2009

BERTEIN Jean-Claude, CESCHI Roger
Discrete Stochastic Processes and Optimal Filtering – 2nd edition

CHANUSSOT Jocelyn *et al.*
Multivariate Image Processing

DHOME Michel
Visual Perception through Video Imagery

GOVAERT Gérard
Data Analysis

GRANGEAT Pierre
Tomography

MOHAMAD-DJAFARI Ali
Inverse Problems in Vision and 3D Tomography

SIARRY Patrick
Optimization in Signal and Image Processing

2008

ABRY Patrice *et al.*
Scaling, Fractals and Wavelets

GARELLO René
Two-dimensional Signal Analysis

HLAWATSCH Franz *et al.*
Time-Frequency Analysis

IDIER Jérôme
Bayesian Approach to Inverse Problems

MAITRE Henri
Processing of Synthetic Aperture Radar (SAR) Images

MAITRE Henri
Image Processing

NAIT-ALI Amine, CAVARO-MENARD Christine
Compression of Biomedical Images and Signals

NAJIM Mohamed
Modeling, Estimation and Optimal Filtration in Signal Processing

QUINQUIS André
Digital Signal Processing Using Matlab

2007

BLOCH Isabelle
Information Fusion in Signal and Image Processing

GLAVIEUX Alain
Channel Coding in Communication Networks

OPPENHEIM Georges *et al.*
Wavelets and their Applications

2006

CASTANIÉ Francis
Spectral Analysis

NAJIM Mohamed
Digital Filters Design for Signal and Image Processing